From Air to Water – Translating Active Flow Control Technology for Maritime Applications

kumulative
Dissertation
zur
Erlangung des akademischen Grades
Doktor-Ingenieur (Dr.-Ing.)
der Fakultät für Maschinenbau und Schiffstechnik der Universität Rostock

vorgelegt von:
Matthias Fromm

Rostock, April 2025

https://doi.org/10.18453/rosdok_id00005533

Gutachter:

1. Gutachter:	Prof. Dr.-Ing. habil. Sven Olaf Grundmann Lehrstuhl Strömungsmechanik, Universität Rostock
2. Gutachter:	Prof. Dr.-Ing. habil. Christian Oliver Paschereit Hermann-Föttinger-Institut, Technische Universität Berlin

Jahr der Einreichung: 2025

Jahr der Verteidigung: 2025

In memory

Avraham “Avi” Seifert

Abstract

This work explores the adaptation of Active Flow Control (AFC) technology from aerodynamic applications to maritime environments, focusing specifically on enhancing the performance of ship rudders. The primary objective is to reduce drag and improve maneuverability through the strategic manipulation of flow fields using fluidic oscillators. These devices, which generate periodic jets without any moving parts, have been extensively studied in aerodynamics but remain underexplored in maritime contexts.

The research is structured into three main phases. The first phase involves the analysis of computational fluid dynamics (CFD) data of a fluidic oscillator to understand the pressure-jet deflection relationship. The second phase comprises experimental investigations of a water-based oscillator, leading to a novel modeling approach based on the FitzHugh-Nagumo system of equations. The final phase focuses on applying the optimized oscillator design to a ship rudder model and conducting comprehensive experimentation to evaluate its performance.

Using the FitzHugh-Nagumo model for interpreting the oscillator mechanism led to numerous insights and a new modeling approach, highlighting the complex flow physics at work in this seemingly simple geometry. Key findings of the rudder experiments include the successful demonstration of fluidic oscillators in delaying flow separation on ship rudders, thus potentially enhancing maneuverability and reducing fuel consumption. This research highlights the potential of AFC technology in maritime applications, offering a pathway to significant environmental and operational benefits in the shipping industry.

Acknowledgments

I would like to express my deepest gratitude to my supervisor, Professor Sven Grundmann, whose unwavering support and guidance made this thesis possible. His expertise and encouragement were instrumental to the success of this research. My thanks also go to Professor Oliver Paschereit for reviewing my thesis.

Words will not be able to describe the contribution of Professor Avraham "Avi" Seifert, a mentor and friend, whose brilliance, dedication and kindness will never be forgotten.

Without order, I want to express my gratitude to colleagues, classmates and friends: Martin Brede, Jochen Kriegseis, Tobias Bestier, Leonie Kandler, Niv Mizrahi, Shay Monat, Ofek Katz, Mark Vassermann, Ulf Grebin, Jörg Wenzlaff, Andreas Wolter, Kirsten Russke, Vincent Klempau, David Frank, Fabian Schumacher, Inga Asmussen, Frithjof Bauer, Nimrod Shay, Lili Altrichter, and all co-authors, as well as remaining institute members.

Last but not least, I owe thanks to my parents for their support and for sometimes giving me a push when needed.

This work received funding by the State Government of Mecklenburg-Vorpommern under the program of Landesgraduiertenförderung; the German Federal Ministry of Economic Affairs and Climate Action under grant no. 03SX496E; and the German Academic Exchange Service (DAAD) under the program Forschungsstipendien für Doktorandinnen und Doktoranden, 2022 (57595508).

Contents

1 Introduction 1

1.1 Background and State of the Art 1

1.2 Motivation and Outline 3

2 Introduction to Flow Control 6

3 Publications 10

3.1 Publication I 10

3.2 Publication II 19

3.3 Publication III 28

3.4 Comparison of Methods 48

3.5 Conclusion of the Publications 49

3.6 Associated publications 50

4 Extended Discussion 51

4.1 Chaos, Spiking and Absence of Oscillations 51

4.2 Limit cycle behavior 53

4.3 POD modes and the FHN system 54

4.4 Common base POD analysis of flow rate variation 56

4.5 Application of the FHN equation to the LES data 57

5 Outlook 58

Bibliography 61

1 Introduction

1.1 Background and State of the Art

In recent years, the significance of ecological and economic considerations in applied fluid mechanics research has been amplified. This is primarily due to the global imperative to reduce fuel consumption across all vehicle types, a key strategy in mitigating greenhouse gas emissions and combating global warming. Within this context, the field of fluid mechanics is tasked with the challenge of devising more efficient lift and control surfaces, and flow-exposed geometries in general. This is because a reduction in drag directly corresponds to a decrease in fuel consumption.

Active Flow Control (AFC) presents a promising solution to the demand for enhanced efficiency, while simultaneously reducing the cost and complexity of the components involved. The theoretical groundwork for AFC was laid by Prandtl [1] through his seminal boundary layer suction experiments. Subsequent research in this domain has primarily focused on aerodynamic applications, with the most advanced experiment to date involving the application of separation control to the vertical tail of the Boeing 777 Ecodemonstrator [2, 3].

Particularly, AFC refers to the strategic manipulation of the flow field to achieve desired effects by applying external energy sources (in contrast to Passive flow control, which does not require additional energy). The desired effects are achieved by modifying the boundary layer — the thin region of fluid near a surface where viscosity effects are significant. AFC using pulsed fluid jets has become a well—established and highly researched technique in aerodynamics. By using devices such as fluidic oscillators, which generate periodic jets of fluid, AFC can dynamically influence the structure of the flow using small, controlled disturbances that interact with the boundary layer, enhancing mixing, and creating stable or unstable vortices. Consequently, AFC can delay flow separation, reduce drag, or enhance lift, leading to more efficient and effective control over the fluid dynamic properties of various surfaces, such as aircraft wings and control surfaces, thereby improving overall performance and energy efficiency.

A fluidic oscillator, as depicted in Figure 1.1, is a device designed to transform a steady input flow into an oscillatory output using fluid dynamic principles without any moving parts. Pioneering work by Spyropoulos [4], Viets [5], and

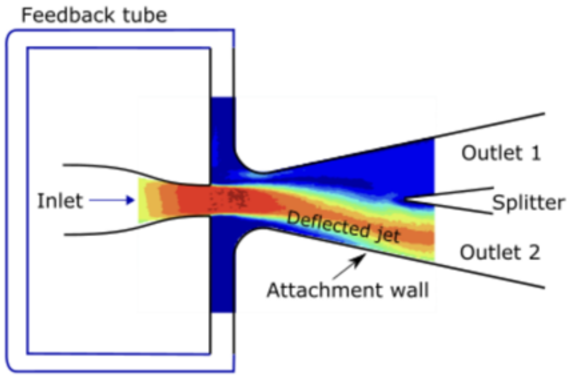

Figure 1.1: Fluidic oscillator schematic.

others in the 1960s and 1970s laid the groundwork for understanding these devices' dynamic behavior. These devices exploit the Coanda effect, where a jet flow attaches to a nearby surface, and feedback mechanisms to create self-sustained oscillations. The basic design consists of an inlet nozzle directing fluid into a chamber with diverging walls and control ports connected by feedback tubes. The jet alternates between the walls, creating a periodic switching of the flow direction. The fluidic oscillator's simplicity, reliability, and ability to operate without moving components make it an effective actuator for AFC systems.

Despite their widespread use, the exact mechanisms behind fluidic oscillations remain a topic of discussion, with various theories proposed over the years and considerable effort dedicated into understanding the oscillation mechanism, with particular focus on the sweeping jet oscillator (e.g.[6–10]).

Like airplane control surfaces, ship rudders and other hydrodynamic control surfaces experience flow separation, which restricts the maximum steering forces and, consequently, the maneuverability of the vessel. Furthermore, conventional rudders are designed to provide lift forces and withstand loads that occur only for brief durations, such as during harbor maneuvers. Most of the time, the ship's rudder is deflected at small Angles of Attack (AoA) [11]. Despite this, drag is generated continuously as long as the ship is in motion, a scenario akin to the vertical tail of commercial aircraft where AFC has been successfully implemented [2, 3]. Despite these parallels, research on AFC in a maritime context, utilizing traditional actuation techniques, has been relatively sparse [12–17]. Constant blowing techniques employing the Coanda effect were investigated on flapped rudders and horn-type rudders. These investigations were conducted at low Reynolds numbers, used small scale models and mostly investigated the properties of the infinite foil using endplates. Pulsed or oscillatory blowing, the state-of-the-art methods of aerodynamic AFC, have not been applied so far for realistic ship rudder geometries at relevant Reynolds numbers.

The state-of-the-art in flow performance improvement devices for commercial shipping primarily revolves around passive control methods and mechanical modifications aimed at reducing drag and enhancing efficiency. These include optimized hull designs, bulbous bows, and various appendages like fins and ducts to improve hydrodynamic flow. Additionally, the use of air lubrication systems, which create a layer of microbubbles along the hull, has been explored to reduce frictional resistance. The maritime sector has largely overlooked AFC, possibly due to the complexity of applying such techniques in the highly turbulent and variable marine environment. The potential for AFC to significantly enhance ship rudder performance by delaying flow separation and increasing maneuverability presents a compelling case for its adoption, offering the possibility of substantial improvements in fuel efficiency and emissions reduction.

However, applying AFC to marine environments poses unique challenges. Ship rudders operate under highly inhomogeneous flow conditions, influenced by the wake of the hull and the propeller slipstream. The hydrodynamic performance of rudders is often limited by flow separation at high angles of attack, which reduces steering efficiency and increases drag. Previous studies on rudder performance have primarily focused on constant blowing techniques and low Reynolds number experiments, with limited exploration of AFC in non-applicable settings.

1.2 Motivation and Outline

The motivation for this research was to bridge the gap between the established use of AFC in aerodynamics and its potential application in marine environments, specifically on ship rudders. By understanding the oscillation mechanism in fluidic oscillators and designing an effective water-based oscillator, it became possible to explore the benefits of AFC for ship rudders. The ultimate goal was to propose a method enhance the efficiency and maneuverability of ship rudders, thereby reducing fuel consumption and environmental impact in the shipping industry.

This thesis is structured around three main phases, each representing a significant milestone in this journey. The first phase involved the analysis of CFD data of fluidic oscillators to identify the relationship between pressure difference and jet deflection. The second phase consisted of experimental investigations of a water-based oscillator, leading to a new modeling approach of the flow physics involved in the self-sustained oscillations of this device, based on the FitzHugh Nagumo system of equations. The final phase focused on applying the optimized oscillator design to a ship rudder model and conducting extensive tests to evaluate its performance.

Through these phases, the research aimed to advance the understanding and application of AFC in marine environments, offering potential solutions for improving ship rudder performance. The findings from this research could pave the way for further innovations in maritime AFC technology, contributing to the broader goal of reducing fuel consumption and environmental impact in the shipping industry. The conducted research has been published in three journal publications as listed in Table 1.1.

Publication I	M. Fromm, J. Kim, A. Seifert, J. Kriegseis, and S. Grundmann, Flow patterns of self-sustained oscillations in fluidic diverters, AIAA Journal 60, 4207 (2022). DOI: 10.2514/1.J061280.
Publication II	M. Fromm, S. Grundmann and A. Seifert, Fluidic FitzHugh-Nagumo oscillator, Physics of Fluids, 37.2, 027115 (2025). DOI: 10.1063/5.0250615.
Publication III	M. Fromm, T. Bestier, S. Brüns, F. Kluwe, A. Hylla, F. Matin, A. Seifert, and S. Grundmann. Active flow control applied to a ship rudder model, Ship Technology Research, 71.1, (2024). DOI: 10.1080/09377255.2023.2275373.

Table 1.1: List of Publications

Various types of oscillators have been reported to be compatible with water [18–20] and have been used to investigate aerodynamic issues using water tanks. In this work, a fluidic oscillator design based on the fluid amplifier principle was chosen (as depicted in Fig. 1.1). However, it has been observed that the performance of the oscillator is sensitive to the density and viscosity of the operating fluid [21], and initial experiments of the author with fluidic oscillators in water faced significant challenges. The oscillators often failed to produce oscillations or resulted in one-sided outputs, demonstrating that the design principles established for air-based oscillators could not be directly applied to water, and crucial clues in the understanding of the oscillator are still missing. This prompted a deeper investigation into the oscillation mechanisms to design a successful water-based oscillator.

A significant challenge however in studying air-operated fluidic oscillators experimentally is their operation under high flow velocities and oscillation frequencies, which complicates data acquisition of any type. To overcome this, a comprehensive analysis of available computational fluid dynamics (CFD) data was conducted. This analysis, presented in the first paper, revealed that the pressure difference across the control ports is linked with jet deflection, while the flow in the feedback tube acts as a secondary mode that influences this pressure difference and jet deflection.

Building on these insights, a detailed experiment was designed using a water oscillator, which provided optical access for Particle Image Velocimetry (PIV) and Laser Doppler Anemometry (LDA), along with pressure taps on the control ports. This experiment, detailed in the second paper, showed that the waveform of pressure and feedback tube flow resembled variables of the FitzHugh-Nagumo system of equations, a model used in the study of excitable systems. This discovery allowed for a more informed approach to designing a water-based oscillator that operates as intended.

The FitzHugh-Nagumo (FHN) system is a mathematical model originally developed to describe the electrical activity of excitable cells, such as neurons and cardiac cells. It captures the essential features of excitability and refractory behavior using a set of nonlinear differential equations. In the context of this thesis, the FHN system's relevance emerged during the experimental investigation of the water-based fluidic oscillator. The experiment, detailed in the second paper, revealed that the pressure and feedback tube flow waveforms closely resembled the variables of the FHN system. This similarity provided a new perspective on understanding the oscillation mechanisms within fluidic oscillators. The FHN model, with its well-defined excitable dynamics, offered a framework for interpreting the observed oscillatory behavior in the fluidic system. By drawing parallels between the fluidic oscillator's dynamics and the FHN system, it was possible to gain deeper insights into the pressure-driven switching mechanism and the role of feedback flow. This understanding was crucial for designing an oscillator that operates effectively in water, as it highlighted the key parameters and their interactions that govern the oscillatory behavior. These findings not only advanced the fundamental understanding of this fluidic oscillator, but also provided practical guidelines for optimizing their design for marine applications, contributing significantly to the overall goals of the thesis.

Armed with a better understanding of the physical connection between pressure difference and feedback tube flow, the next step was to apply this newly designed oscillator to a ship rudder model and conduct extensive tests to characterize its performance. These experiments, described in the third paper, utilized underwater PIV, force measurements, and advanced analysis techniques to evaluate the AFC system's effectiveness in delaying flow separation and enhancing rudder performance.

2 Introduction to Flow Control

The current design strategies for vehicles are predominantly based on the assumption of time-independent, steady-attached flow around and within the vehicle's body. The geometries and systems derived from this principle function effectively, yet they are not without their drawbacks. These strategies often result in conservative designs that are inherently energy-inefficient, heavy, and consequently, costly to manufacture and operate.

In reality, flows are inherently unsteady and eventually become turbulent. The inability to accurately predict highly unsteady turbulent flows remains one of the most significant unresolved scientific questions to date. However, it is important to note that unsteady flows, and turbulence in particular, are not always disadvantageous. As demonstrated by Wygnanski [22] and Oster and Wygnanski [23] in the 1970s, artificially induced unsteady vortical motions can enhance mixing beyond the turbulent limit. This enables the design of vehicles that operate at a higher efficiency level than what is naturally possible for a given shaping.

These concepts have gained considerable traction among researchers, leading to the emergence of one of the most promising branches of unsteady fluid mechanics, known as Active Flow Control (AFC). This branch employs localized, unsteady vorticity disturbances to alter the state of the flow along its development path [24, 25]. These disturbances can be introduced into the flow through a variety of means, methods, and devices. It is postulated that with appropriate unsteady actuation imposed by devices, termed actuators, the advantages of flow unsteadiness can be harnessed to enhance the overall system efficiency, specifically to delay and suppress flow separation. Figure 2.1 provides a schematic representation of this method for a generic boundary layer.

Moreover, it is posited that incorporating unsteady AFC into the design cycle can yield additional benefits, well beyond those existing in systems that are properly designed to operate in turbulent flow conditions. These benefits could include reduced weight and cost, fewer parts, and decreased maintenance efforts. Figure 2.2 demonstrates the effect of Active Flow Control on the flow around an airfoil. By delaying separation or reattaching separated flow, the lift and drag characteristics of technical surfaces can be positively influenced. While these techniques have primarily been applied to aerodynamic problems, they also hold significant potential for application on marine vehicles or underwater structures.

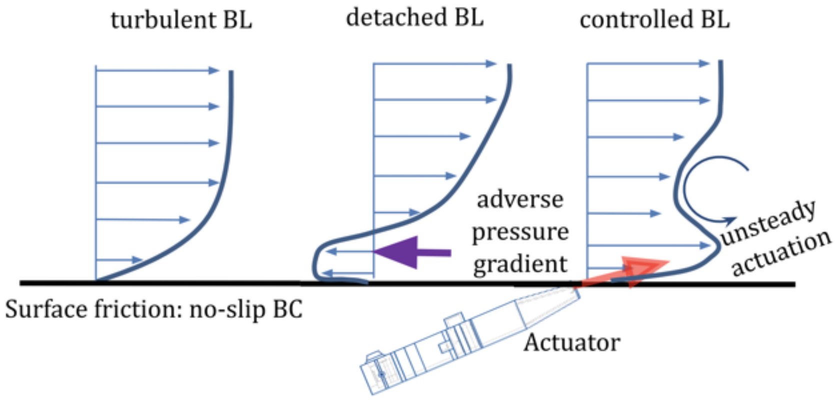

Figure 2.1: Schematic representation of a generic Boundary Layer (BL) with unsteady momentum addition by an actuator. The momentum addition and the enhanced mixing increase fluid flow momentum close to the wall and enable the flow to (re-)attach to the surface.

Control surfaces such as ship rudders and stabilizing fins are subject to flow separation, which can limit the maximum control forces and consequently, the turning radius.

Flow separation occurs when fluid particles near a wall are slowed down by friction and must advance against a positive pressure gradient. At some point, the particles come to rest, and further downstream of this point, the flow reverses and moves upstream. This point is called the separation point. On a lift-generating device, separation is linked with lift breakdown and increasing drag. The latter is true for blunt bodies as well, where separation leads to increased unsteady form drag.

To suppress separation, momentum must be added to the slow flow region close to the wall. This can be done either by directly adding momentum via tangential injection of high-speed fluid (steady blowing) or by enhancing the mixing inside the boundary layer, thereby transporting momentum-rich fluid closer to the wall (oscillatory blowing and vortex generating jets). Compared to direct addition of momentum, mixing enhancement requires less excitation energy input [26]. By exploiting naturally occurring vortex structures in the flow, mixing enhancement can promote the necessary mixing, reducing power consumption by up to 90% [27]. This method, known as pulsed or oscillatory blowing, amplifies spanwise vortex structures to enhance mixing.

Among the numerous methods proposed for AFC, a few have distinguished themselves. Steady blowing, for instance, involves the ejection of jets in a

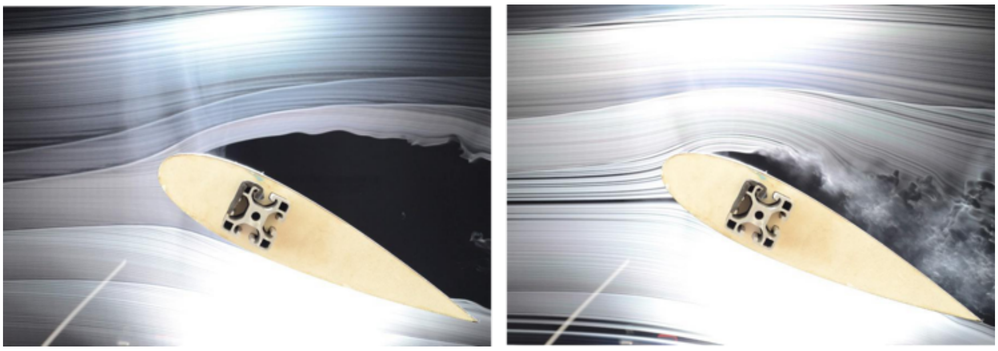

Figure 2.2: Smoke flow visualization of flow reattachment using steady blowing. Left: detached flow, Right: reattached flow using steady blowing through slots in the upper surface of the foil supplied with pressurized air. Wind tunnel experiment at $u_{inf} = 2\,\mathrm{m/s}$ at the University of Rostock.

predominantly downstream, wall-tangent manner to energize the decelerating boundary layer [27]. Pulsed blowing adds unsteady excitation to wall-jets, with jets being ejected from multiple slots in a cyclic manner. This creates beneficial vorticity patterns that redistribute momentum from the outer flow towards the wall, thereby reducing the energy required for a given task.

Another method, steady suction, involves drawing air through slots or holes on the surface to energize the boundary layer and increase vorticity. This method, suggested by Prandtl as early as 1904 [1], has proven to be extremely efficient. Steady suction can evolve into unsteady suction, a technique that has only recently been proposed [28]. The coupling of vorticity patterns created by actuation with unstable modes of the flow leads to a favorable interaction, further reducing the required actuation energy.

Another method for mixing is vortex generating jets (VGJ). These continuous jets are blown normal or at an angle into the boundary layer, introducing streamwise vortices. While the output of VGJs resembles that of steady jets, they require less air [29].

Periodic excitation, including both pulsed jets and oscillatory blowing, is another important tool in active flow control. Studies have shown that pulsed jets can be more effective than steady jets in delaying flow separation and enhancing mixing [30, 31]. The effectiveness of these methods is closely related to the excitation frequency and the Strouhal number. Streamwise vortices and spanwise vortices both play crucial roles in the process, with each type contributing differently to the overall mixing and momentum transport within the boundary layer.

For optimal excitation, it is necessary to excite the flow at a frequency close to that of the naturally occurring coherent structures in the flow [25]. This is related to the Strouhal number and is described by the reduced frequency:

$$F^* \equiv f_e x_{TE}/u_\infty, \tag{2.1}$$

where f_e is the oscillation frequency of the jet and x_{TE} is the distance between the actuator and the trailing edge of the body. Typically, the optimal reduced frequency ranges from $F^* \geq 0.03$ to $F^* \leq 4$ [27].

Pulsed blowing (a variant of periodic excitation) can be considered to be the method of choice for active flow separation control today. Several papers have demonstrated the effectiveness of this technology to delay or suppress flow separation when applied on aerodynamic surfaces. Other methods, like synthetic jet actuators (SJA) or plasma actuation, were shown to be less effective at high Reynolds numbers corresponding to aircraft flight conditions or not mature and robust enough with respect to environmental conditions encountered during aircraft operation like rain, icing, sand, and very low temperatures.

Fluidic Oscillators have been proposed as the actuator to create the necessary unsteady flow for pulsed blowing (instead of mechanical valves), and have been studied in a wide variety of Active Flow Control situations. The development of these devices began in the 1960s, with contributions from Spyropoulos [4] and Warren [32]. Since then, many different designs have been introduced. At present, a significant amount of research is being conducted to explore these different actuator designs and their specific implementations bench top [33, 34], prototype [7, 35] and full scale [36–38] investigations. These studies demonstrate the feasibility of different types of fluidic oscillators in similar fields of application.

3 Publications

3.1 Publication I

M. Fromm, J. Kim, A. Seifert, J. Kriegseis, and S. Grundmann, Flow patterns of self-sustained oscillations in fluidic diverters, AIAA Journal 60, 4207 (2022). DOI: 10.2514/1.J061280

Reprinted by permission of the American Institute of Aeronautics and Astronautics, Inc.

Author contributions

Task	Responsible author
Computations	Matthias Fromm
Data Analysis	Matthias Fromm
writing the Manuscript	Matthias Fromm

The first paper delves into the flow patterns occurring within fluidic oscillators, providing insight into the jet switching mechanism. By utilizing Proper Orthogonal Decomposition and Lagrangian Coherent Flow Structures to analyze CFD data, the study finds that the pressure difference between control ports and feedback tube flows are the primary driver of jet deflection, which challenges previously published models that emphasized the role of pressure waves. This nuanced understanding allowed to design the subsequent, targeted experimental study (publication 2), aiming to further the understanding and modeling of the oscillator. Simultaneously, it provided insights for more precise design and optimization of the device, which can be directly applied to AFC systems design choices.

AIAA JOURNAL

Flow Patterns of Self-Sustained Oscillations in Fluidic Diverters

Matthias Fromm*
University of Rostock, 18059 Rostock, Germany
Jeonglae Kim†
Arizona State University, Tempe, Arizona 85287
Avraham Seifert‡
Tel Aviv University, 69978 Tel Aviv, Israel
Jochen Kriegseis§
Karlsruhe Institute of Technology, 76131 Karlsruhe, Germany
and
Sven Grundmann¶
University of Rostock, 18059 Rostock, Germany

https://doi.org/10.2514/1.J061280

A fluidic oscillator is a device capable of transforming a steady input flow into an oscillatory output using solely fluid dynamic principles and without requiring any moving components. Although the basic operation principles of fluidic oscillator are known to some extent, the unsteady and turbulent nature of its internal flow remains difficult to understand. The current study aims to further clarify the complicated flow physics involved in fluidic oscillators by investigating a device based on the fluid diverter principle. Spatiotemporally resolved velocity and pressure data obtained from a large-eddy simulation of the internal flow are decomposed into the proper orthogonal modes. The finite-time Lyapunov exponents are computed on the flowfield reconstructed using the proper orthogonal modes to perform a Lagrangian analysis of the switching mechanism. It is found that four dominant modes are sufficient to describe the jet switching. Strong coherent structures are found to separate the flow going through the oscillator from secondary flows through the feedback tube. The deflection of the jet inside the device is found to depend only on the pressure difference across the control ports, whereas the change of this pressure difference is mediated by the flows in the feedback tube.

Nomenclature

A, V	=	left- and right-hand eigenvectors
a	=	mode coefficients
p	=	pressure, Pa
U	=	snapshot matrix
u, v, w	=	streamwise, lateral, and out-of-plane velocities, m/s
Σ	=	diagonal matrix of singular values
ρ	=	density, kg/m^3
Φ	=	orthonormal basis

Subscripts

in	=	inlet
5 *psi*	=	corresponding to inlet pressure condition p_{in} equal to 5 psi differential
20 *psi*	=	corresponding to inlet pressure condition p_{in} of 20 psi differential

I. Introduction

FLUIDIC oscillators are mechanically simple yet fluid dynamically complex devices. Developed in the 1960s and 1970s [1,2] for fluid logic circuits, the preceding term is used for devices capable of transforming a steady input flow into an oscillating output using solely fluid dynamic principles without requiring any moving parts. The unsteady output flow can be exploited to enhance fluid mixing in various applications: from bubble generation in microreactors [3] to jet spreading in windshield wipers. Recently, renewed interest in these devices occurred in the context of active flow control (AFC) applications, where fluidic oscillators are used as actuators to create unsteady vortical structures inside the boundary layer, which minimize the amount of energy required to alter the boundary layer in a desired way [4].

Among different types of fluidic oscillators described in the literature, the fluid diverter principle (also referred to as the fluid amplifier concept) is among the most used in fundamental and applied experiments in an AFC context (e.g., see Refs. [5,6]). Figure 1 shows a specific implementation of this principle: the suction and oscillatory blowing (SAOB) actuator as proposed by Arwatz et al. [7], and an instantaneous snapshot of the velocity magnitude inside the device as computed by Kim et al. [8].

The general layout, functionality, and nomenclature of such a device is as follows: It consists of three stages. The first stage in the flow direction is called the suction stage or ejector, creating a low-pressure region to entrain additional flow from elsewhere, and thus increase the total mass flow rate that is useful for the AFC application. In the diverter stage, marked with a blue rectangle in Fig. 1, two control ports are connected by a feedback tube made of a flexible tube or a channel machined using (for example) additive manufacturing. There, a continuous inlet jet attaches due to the Coanda effect to one of two diverging walls downstream of the inlet. In the course of the operation of the device, the jet switches between the attachment walls and subsequent outlets, emitting alternating pulses through the outlets. The relevant geometry in the diverter stage is 2.5-dimensional, i.e., it is symmetrical to the two-dimensional plane with the same distance to the floor and ceiling of the device. The last stage is the outlet nozzle, with the nozzle comprising two outlets. The outlet openings would be connected to the aerodynamic surface to be controlled, with the actuator mounted below that surface. Movie 1

Received 14 September 2021; revision received 20 January 2022; accepted for publication 4 March 2022; published online 29 April 2022.

*Research Assistant, Institute of Fluid Dynamics, Albert-Einstein-Str. 2.

†Assistant Professor, School for Engineering of Matter, Transport and Energy.

‡Head of Chair, Meadow Aerodynamics Laboratory, School of Mechanical Engineering, Faculty of Engineering.

§Senior Researcher, Institute of Fluid Dynamics, Kaiserstraße 10.

¶Head of Chair, Institute of Fluid Dynamics, Albert-Einstein-Str. 2.

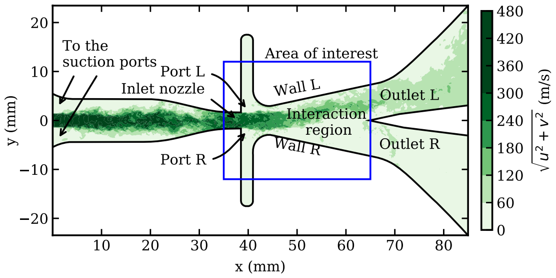

Fig. 1 Nomenclature and instantaneous snapshot of velocity magnitude on the centerplane of the simulation domain. The flow direction is from left to right, and the jet leaves through outlet L [8].

provides visual representations of the switching mechanisms and unsteady flow structures.

Despite the wide usage of the device, the literature provides only a limited understanding of the underlying fluid mechanics causing the jet to switch between the attachment walls. Based on pointwise measurements of velocity and/or pressure inside fluidic oscillators, empirical models and explanations were derived by Spyropoulos [1], Viets [2], and later by Arwatz et al. [7] to explain the dynamic behavior of these devices. Only a few investigations of the entire internal flowfield exist, namely, by Koso et al. [9] using hot-wire anemometry and Wassermann et al. [10] using magnetic resonance velocimetry. The state-of-the-art hypothesis of the working principle describes a pressure difference between the control ports of the oscillator as the primary cause for the deflection of the jet and the acoustic transmission of this pressure through the feedback tube as the cause for switching [7,11].

Rather independently, comprehensive efforts to model the wall attachment characteristics of fluid diverters based on the Coanda effect in general were conducted by (for example) Epstein [12], Lush [13], and Goto and Drzewiecki [14]. These works provide analytical models that use a streamline curvature equation

$$\frac{dp}{dy} = \frac{\rho u^2}{R} \tag{1}$$

for the explanation of the jet deflection. In Eq. (1), dp/dy is the cross-stream pressure gradient between the control ports and R is the curvature radius of the streamline at the center of the jet. Additional equations are then employed to describe the control port pressure and the size of the separation bubble between the main jet and the attachment wall.

However, a satisfactory conclusion incorporating both views (pressure-wave-driven switching and separation-bubble-driven separation) has never been achieved. Certainly, a lack of spatiotemporal resolved flowfield and pressure data adds to this situation. A more thorough understanding of the spatiotemporal relations of theses quantities can add insight to the underlying physical mechanisms, and it may provide guidelines for the design of such devices and improve their performance. The latter is critical for the successful implementation in AFC systems, which is currently delayed due to inefficiency.

This paper aims to extend the understanding of the fluid dynamics that cause the jet to switch by providing the perspective of a data-driven reduced order model (ROM). To achieve this, time-resolved velocity and pressure fields from a large-eddy simulation (LES) of the SAOB actuator by Kim et al. [8] are further analyzed. Velocity and pressure fields inside the actuator's diverter stage are decomposed into proper orthogonal decomposition (POD) modes to test the correlation between jet deflection and pressure distributions. Two approaches are used: a "classical" velocity-only POD [15] and a coupled pressure–velocity POD [16]. The latter allows us to analyze how pressure and velocity correlate with the switching mechanism of the device. To identify possible Reynolds or Mach number effects, datasets from the simulation of different inlet pressures are analyzed jointly with a common-base POD (CPOD) [17]. Lagrangian coherent structures (LCSs) are evaluated by analyzing finite-time Lyapunov exponent (FTLE) fields on the flowfields of the ROM to provide insight into the flow topology [18]. In the following section, details on the dataset as well as the employed POD and FTLE techniques are provided, and Sec. III presents the respective results.

II. Methods

A. Description of the Dataset

The datasets used for the current analysis are the LES computations carried out by Kim et al. [8]. An entire SAOB actuator device was modeled, including the suction stage and the nozzle outflow into quiescent air downstream of the outlets. The fully compressible Navier–Stokes equations were solved on unstructured grids consisting of 47 million control volumes in three dimensions using the high-fidelity CharLES code using a cell-based finite volume discretization [19]. The Vreman subgrid-scale model [20] was used with a constant turbulent Prandtl number of 0.9. The simulations were carried out for three different inlet pressures, where the inlet pressure is defined as the differential pressure between the ambient, atmospheric pressure downstream of the outlets and the pressure at the inflow boundary to the suction stage. The LES prediction shows time-periodic jet switching, which is quantified using mass flow rates on the two outlets as well as the two feedback ports. The oscillation frequency, wall pressure distribution, outlet velocity, and suction velocity show good agreement with the measurement. Additional details of the simulation setup can be found in the work of Kim et al. [8].

Snapshots of the velocity and pressure fields were obtained for five oscillation periods for each inlet pressure after the decay of initial transient effects. The sampling rate of these snapshots is 47 kHz, resulting in 673 samples for an inlet pressure of $p_{\mathrm{in}} = 20$ psi differential (psid) and 1507 samples for $p_{\mathrm{in}} = 5$ psid. At $p_{\mathrm{in}} = 5$ psid, flows are subsonic everywhere in the oscillator with a peak Mach number of $\mathrm{Ma} = 0.4$ at the inlet of the interaction region. In contrast, at $p_{\mathrm{in}} = 20$ psid, the flow regime is supersonic at the suction stage, and the Mach number is 0.8 at the inlet of the interaction region, with no shocks or supersonic flow present in the area considered in the current analysis. The flows oscillate at 150 and 330 Hz, respectively.

The analysis presented in this study is performed in the actuator's diverter stage. The geometry of the device is essentially two-dimensional in this region, and thus the oscillator's centerplane is chosen for the analysis.

B. POD Setup

In this work, three different POD formulations are used to investigate the relations between velocity, pressure, and distinct operating parameters. The POD [15] decomposes a dataset $\boldsymbol{D}(\boldsymbol{x}, t)$ of snapshots into a combination of time-dependent coefficients $a_i(t)$ and an orthonormal basis of spatial modes Φ such that the dataset may be reconstructed by the linear combination

$$\boldsymbol{D} = \sum_i a_i(t)\Phi_i$$

In all formulations, singular value decomposition is used for computing the modes and coefficients, where matrix $\boldsymbol{U}$ is decomposed into left- and right-hand eigenvectors and singular values: $\boldsymbol{U} = A\Sigma V^T$. Then, the individual modes are the columns of the left-hand eigenvectors, $\phi_i = A_i^T$, and the associated energy e_i of the i th mode is the square of its singular value

$$e_i = \Sigma_i^2$$

The coefficients are obtained by multiplication of the singular values with the right-hand eigenvectors

$$a_i = \Sigma_i V_i$$

First, the standard velocity-only POD is computed, where each column of $\boldsymbol{U}$ is built from the rearranged spatial velocity data at one point in time: $u_i = [uv]^T$. The velocity in the out-of-plane direction w is not included in the decomposition. The cross correlations of the in-plane components u and v with w were found to be negligible, and thus the resulting modes are independent of a potential inclusion of w. Also, the mean velocity $\bar{w}$ is insignificant in the area of interest, and thus only two components will be discussed.

A coupled pressure–velocity POD is computed as an extension of the standard formulation. For this, the pressure distribution is appended to each snapshot vector such that $u_i = [uvp]^T$. The coupling of a scalar and velocity in a POD was used (for example) in Ref. [16]. Commonly, the reconstruction by means of POD is claimed to be "energy optimal" because the correlation of velocities is related to flow kinetic energy. However, if the pressure is included, this no longer holds true; and the only claim that can be made is that POD provides a basis optimal with respect to the variance of the quantities.

Another aspect of the inclusion of the pressure in the decomposition includes the different magnitudes of the velocity and pressure fields. Different scaling and normalization approaches were tested, where the resulting modes were found to be dominated by either the pressure or the velocity. Thus, for the results presented here, it was decided to leave the data unmodified, which implies the corresponding eigenvalue problem to be predominated by the pressure data. Because the influence of the pressure on the jet switching is an open discussion, as outlined in Sec. I, this is therefore an approach to obtain a model "from the perspective" of the pressure.

The third formulation is the CPOD [17], which seeks to enable a quantitative comparison between datasets with different parameter settings. In this case, the POD modes are computed using the same number of snapshots from two different inlet pressure conditions. The snapshots are stacked sequentially along the time axis and are decomposed into a shared orthogonal basis: $U = [U_{20\,psi} U_{5\,psi}]$. A sectional analysis of the mode coefficients enables us to investigate the influence of a certain parameter realization by comparing the relative variance contribution of the respective subset to the cumulative variance of the entire dataset. This enables us to investigate how the different inlet pressures (and subsequently different Reynolds and Mach numbers) act on the principle of the jet switching.

Because it is not clear whether the switching process may be harmonic or not, the POD is favored above a spectral POD or a dynamic mode decomposition formulation to allow arbitrary wave forms of the modal coefficients rather than imposing the restriction of a sinusoidal wave form.

The data inside the area of interest are used on the original, unstructured grid to compute the POD modes. Before the decomposition, the data are multiplied with the corresponding cell volumes of the simulation to account for the spatial distribution of the velocity and pressure measurements. For the reconstruction, the modes are divided by the cell volumes to regain the dimensional data.

C. Computation of FTLE

Fields of the FTLE display spatial convergence or divergence, depending on the particle-path integration direction in time (backward or forward, respectively). High "ridges" of the FTLE represent material lines across which no mixing occurs. The FTLE implementation in this study follows the approach introduced by Shadden et al. [18]. To eliminate high-frequency fluctuations, the flowfield is reconstructed before FTLE computation using the four most energetic modes of the velocity-only POD and the phase-averaged mode coefficients, thus including 98.7% of the total phase-averaged energy. The reconstructed data are interpolated to a regular, evenly spaced grid for computational efficiency. Virtual particles are seeded initially on a regular grid with a resolution of 450×450 in the area of interest. Particles are advanced on the time-dependent flowfield by numerical integration using the ODEPACK implementation of the Adams/BDF scheme [21]. The integration time is chosen to be 0.5 switching periods in both forward and backward directions. After this time span, most of the particles have left the domain so that the FTLEs are invariant to an additional increase in integration time.

III. Results and Discussion

With the results of the CPOD, the contribution of the modes to the overall energy relative to each other can be computed and compared by computing the ratio between the two datasets: ratio $= \sigma^2(a_{i,5\,psi})/\sigma^2(a_{i,20\,psi})$. This ratio is approximately one for modes $i \leq 7$. At higher modes, the ratio decreases below one, which can be attributed to stronger turbulence present at $p_{\text{in}} =$ 20 psid. Thus, the flowfield can be described with the same set of modes and relative weighting, independent of the inlet pressure and the change in Reynolds and Mach numbers. Based on this, in the remainder of this section, we discuss the analysis results for the 20 psi case.

The time-resolved coefficients of the first four POD modes contribute to 76.1 and 64.5% of the total variance for the coupled and for the velocity-only cases, respectively (cf. Fig. 2). A large number of modes is therefore required to capture the high-frequency fluctuations in the fields.

Despite this, the unique behavior of the flow and pressure fields are well approximated by only considering the modes 1 and 3, as will be shown in the following. In Fig. 3, the reconstructions of the flowfield with individual modes are compared with the original sample from the LES simulation at four different locations. For each location, the respective mode or modes are used and summed with the mean field to show the contribution of the individual modes. To obtain a clear picture, the original and reconstructed data are each averaged over small areas around the locations displayed in Fig. 4. Furthermore, the pressure data from areas I and II are subtracted to compute the pressure difference between the control ports, corresponding to an approximation of the left-hand side of Eq. (1). Location III is the location where the jet is expected to initially attach to the wall and is chosen as representative for this condition. Similarly, location IV is chosen to illustrate the flow at the left outlet. For the feedback tube flow, the mean of locations I and II is computed and displayed in Fig. 5.

Figure 3a shows that mode 1 reconstructs the port pressure difference remarkably well, despite the respective singular value only accounting for 51.6% of the total energy (compare Fig. 2). Mode 1 also reconstructs a large part of the flowfield between the control ports at location III, capturing the dynamical behavior well (Fig. 3b). The characteristics of the outlet flow may be well described by mode 3 alone, as Fig. 3c shows. In contrast, as Fig. 5 shows, the feedback tube flow follows a different dynamic and is only well approximated when considering at least modes 1 and 3 for the reconstruction.

The main observation here is that mode 1 describes the port pressure difference and the attachment of the jet to the wall remarkably well, whereas the output flows are approximated by mode 3, which is not associated with the port pressure difference. At the same time, the feedback tube flow is not directly correlated, in a statistical sense, with the pressure difference or the jet attachment. This claim is further supported by the relative energy contribution of the modes after the time histories of the coefficients are phase averaged. The phase average is computed with respect to the coefficient of the

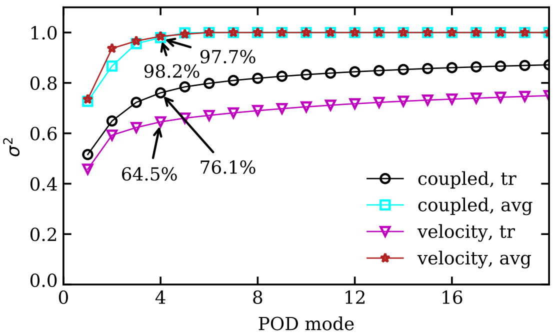

Fig. 2 Energy contribution of the POD modes of the 20 psid dataset: time resolved (tr), and phase averaged (avg).

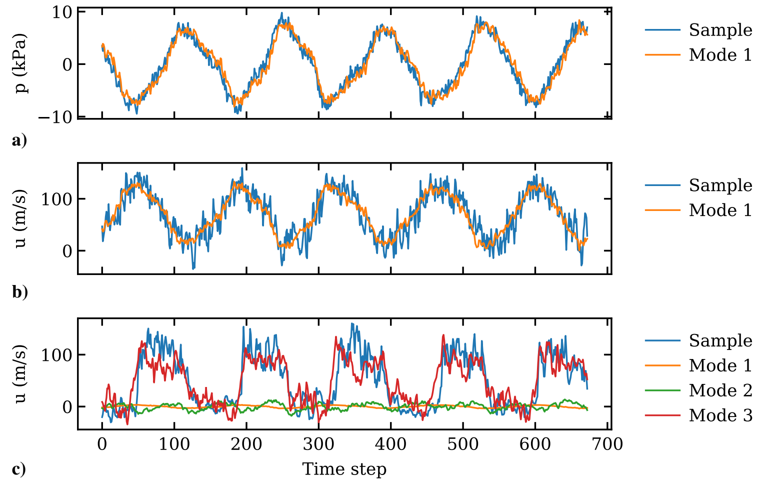

Fig. 3 Reconstruction of flowfield with individual modes. Entire time history of 20 psid dataset is displayed, and individual plots are obtained by averaging over corresponding areas marked in Fig. 4: a) port pressure difference (difference of locations I and II), b) streamwise velocity between walls (location III), and c) streamwise velocity at location IV (left outlet).

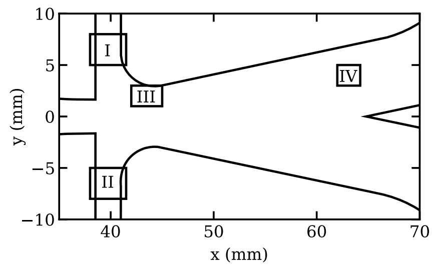

Fig. 4 Areas over which quantities are averaged for reconstruction.

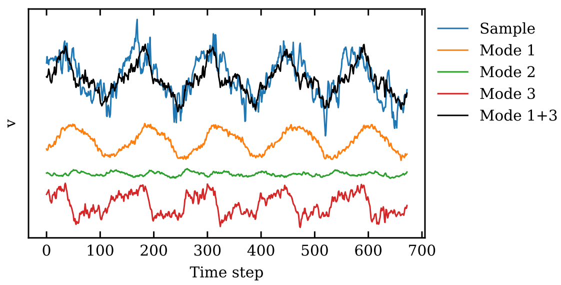

Fig. 5 Reconstruction of flows through the feedback tube, averaged over locations I and II. Individual modes are shifted along the ordinate for clarity.

first mode by detecting zero crossings and defining one period by every other zero crossing. After that, the weight w_i of the i th mode can be computed as the variance of the phase-averaged coefficient: $w_i = \sigma^2(\tilde{a}_i)$.

In this case, the first four modes contribute substantially more (97.7 and 98.2% for the coupled and velocity-only cases, respectively) to the overall energy content, as Fig. 2 shows. The coefficients of the higher modes cancel out in the phase-averaging process because they fluctuate in a manner that is not synchronized to the jet switching. The phase-averaged coefficients shown in Fig. 6 point out that modes 1 and 3 oscillate at the jet switching frequency, whereas mode 2 oscillates at twice the switching frequency, and thus represents higher harmonic components of the switching. The phase-averaged coefficients will be discussed in more detail in the following paragraphs:

Considering the results so far, it seems justified to discuss the mechanism of the jet switching based on the three most energetic modes. First, we will discuss the topology of the individual modes, and subsequently their dynamical interplay. The three most energetic modes and the flowfields that emerge when these modes and the mean fields are superimposed are displayed in the left and right columns in Fig. 7, respectively. The superposition for each mode is computed with the maximum value of the phase average of the respective coefficient such that the superposition is $\hat{U}_i = \bar{U} + \max(\tilde{a}_i)\phi_i$.

In the first mode, the pressure difference between the ports is correlated with the deflection of the jet toward a wall. The jet is bent toward the side with lower pressure (denoted by L), whereas on the opposite side, where the jet is not attached (denoted by R), the pressure is higher than average. Furthermore, a low-velocity flow is observed in the feedback tube from port L to R, i.e., away from the side where the jet is attached. Superimposed with the mean (right column), it presents the attachment of the jet to the wall. The attachment begins right downstream of the control port and is not yet fully developed; the jet is split between the outlets.

Note that the direction of the pressure difference and the direction of the flow change with the sign of the coefficient. For the interpretation of the mode topology, we assume a positive coefficient; and in the discussion of the dynamical interaction, we will address the change in sign.

The topology of mode 3 is similar to that of mode 1, but the attachment of the flow to the wall spans the entire analysis domain down to the outlets. In contrast to mode 1, the pressure difference between the ports is negligible. On the detached side (wall L), fluid travels upstream toward the control port. Again, in contrast to mode 1, there is a strong and directed flow through the feedback tube toward the attached side (wall L to R), i.e., opposite to the direction observed in mode 1.

The second mode describes the lateral movement of the jet while it changes sides, where the jet aligns with the centerline when it transitions from one wall to the other. The pressure increases in the streamwise direction because the jet is decelerated by interacting with the resting fluid in both port areas and the downstream splitter. Mode 4 repeats the dynamic of mode 2 but describes the lateral movement of the jet downstream of the region covered by mode 2 and is not further discussed here.

With the impact of the individual modes in mind, several specific phase angles of a switching cycle are discussed in the following, as marked by capital letters in Fig. 6. Refer also to Fig. 8, where selected velocity and pressure fields are shown.

At phase angle A, mode 1 is at its maximum value and modes 2 and 3 are much smaller in amplitude. The jet has just completed

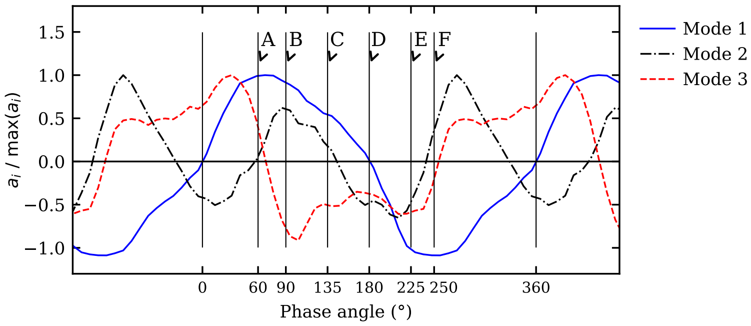

Fig. 6 Phase-averaged coefficients of first three modes. Capital letters mark phase angles discussed in the text.

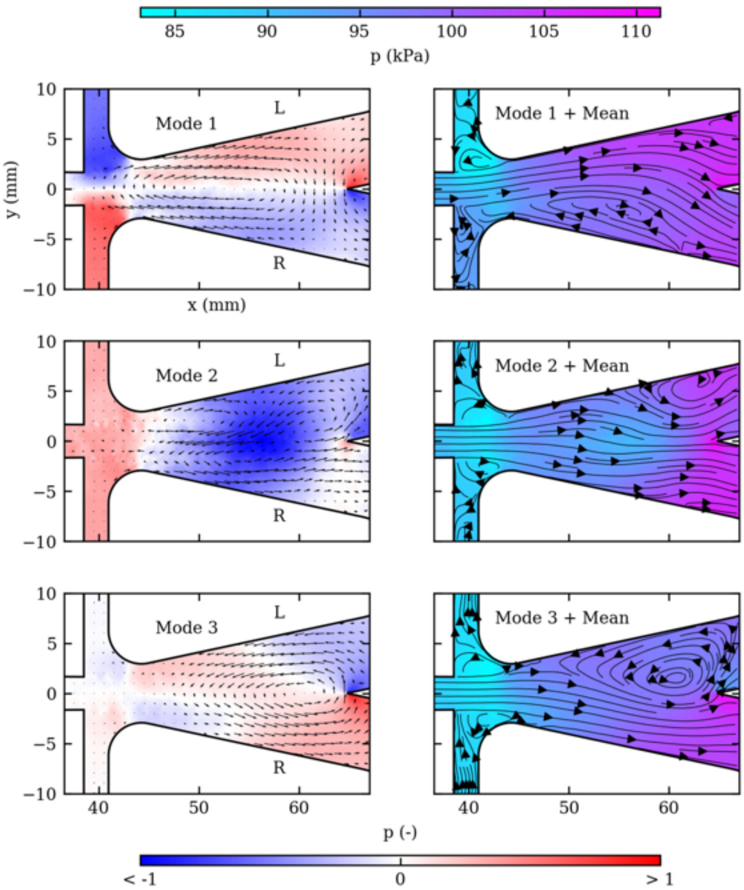

Fig. 7 Most energetic POD modes (left column's color map denotes dimensionless pressure quantity, and arrows correspond to velocity vectors) and flowfield obtained by adding mean flow to the respective mode (right column's color map displays pressure and streamlines of the resulting flowfield).

its attachment to wall L. Immediately after, at point B, mode 3 approaches its minimum value and the jet remains attached over the full length of wall L; and a flow through the feedback tube has developed. Note that mode 1 and 3 attach to the same wall when their coefficients have opposite signs. Since mode 1 reaches its maximum before mode 3, the jet attaches first in the upstream part of the interaction region; and the new flow direction propagates to the outlets. As mode 3 became stronger in its amplitude, mode 1 is weakened (point B to point C), which could be attributed to the flow through the feedback tube supplying fluid to the attachment side port (point L), thus increasing the pressure there. At point D, mode 1 approaches zero amplitude. There is no pressure difference across the ports, and the jet is centered in between the walls. However, it is still attached to the wall further downstream; and the flow through the feedback tube associated with mode 3 is strong. The feedback flow is draining port R while supplying fluid to port L. Entrainment by the jet and feedback flow co-act, rapidly lower the pressure at port R, and promote attachment of the jet to wall R (point D to point E). With the sign change in pressure difference, the feedback tube flow decelerates and finally reverses, together with the attachment of the jet over the full length of the wall (point F). Phase angle F now presents the same situation as

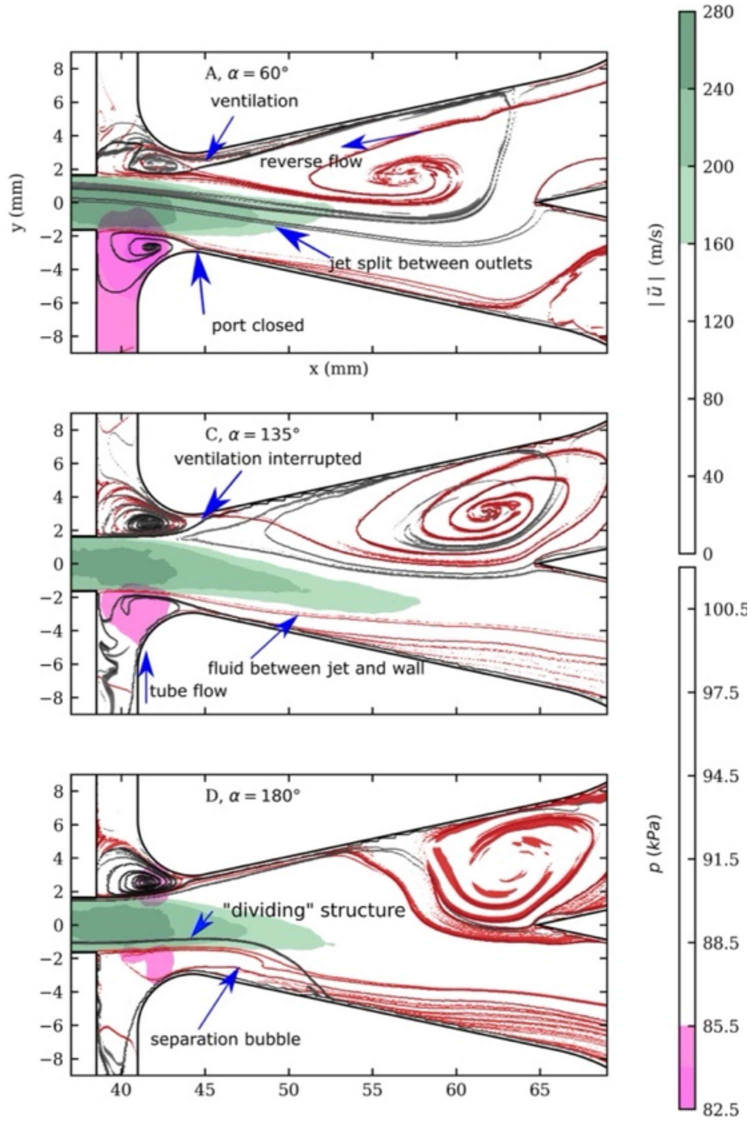

Fig. 8 Snapshots of the phase-resolved FTLE fields combined with pressure and velocity: high values of repelling FTLE (black) and attracting FTLE (red). Indicated phase angles relate to Fig. 6.

described for point A but on the opposite wall. From this condition, the pressure difference decreases again and the cycle repeats in the other direction.

In the whole cycle, the maxima of mode 2 indicate when the jet is centered between the walls, and the minima indicate full attachment to a wall. The reconstructed flow and pressure fields are rendered in movie 2.

The observed distribution and temporal evolution of the pressure difference between the ports does not point toward evidence of traveling pressure waves, as suspected in Ref. [1] and by others. The evolution of mode 1, and thus the pressure difference, spans the entire cycle of the switching in a continuous manner; and the jet is always attached to the side with the lower pressure. Thus, another effect must be responsible for the switching of the jet between the walls.

The FTLE field is computed for the flowfield reconstructed from phase-averaged mode coefficients. In Fig. 8, snapshots of the FTLE field are presented alongside with velocity and pressure data corresponding to phase angles A, C, and D, marked in Fig. 6. The color maps of the velocity magnitude and pressure distribution are adjusted to show only the highest and lowest values, respectively, to provide a clearer but physically correct visualization. Black and red lines indicate repelling and attracting coherent structures, respectively.

When the jet completes its attachment to wall R (Fig. 8a), a repelling ridge cuts off the feedback tube from the interaction region. At opposite side L, fluid from the interaction region reverses and travels upstream toward port L, which explains the pressure rise at this side associated with the first POD mode. When the jet separates from wall R and returns to the center of the interaction region (Fig. 8b), this upstream flow is terminated because the jet blocks the entire width of the interaction region. This can explain the rapid decrease in pressure at port L because the supply of fluid that enabled the higher pressure is instantaneously interrupted.

On the opposite side, fluid flows from the feedback tube toward the main jet and feeds a small region bounded by high FTLE values between the jet and wall. Ridges of the FTLE fields show that the fluid in the feedback tube is separated from the main jet for most of the time and only a small amount of fluid is interchanged with the interaction region before the jet separates from the wall. In movie 3, the forward and backward FTLE fields are rendered for five oscillation periods.

Note that the separation of the jet from the wall occurs as soon as the pressure difference vanishes and seems not to be dependent on the slow growth of the separation bubble between the jet and wall. Rather, the separation is forced by the jet; and the necessary fluid to fill the region between the jet and the wall is separated from the jet and entrained from downstream. This is in contrast to the models of Epstein [12] and Goto and Drzewiecki [14] that, in general, model the growth of the separation bubble by supply from the feedback tube as the cause for detachment.

In Fig. 8c, the repelling ridge enclosing the separation bubble mimics the "dividing streamline" introduced by Chapman et al. [22]. This is defined as the edge between the fluid of the jet and secondary fluids originating from the control ports. In the literature, this streamline originates from the edge of the inlet nozzle. However, as can be seen in Fig. 8c, the separating structure originates from inside of the jet and stagnates against the attachment wall, and thus limits the separation bubble. At this point, no fluid is entrained from the control port and convected downstream with the jet, but all fluid is captured inside the separation bubble, which again is in contrast to the cited literature.

In the studies of other fluidic oscillator configurations, secondary effects influencing the flowfield have been reported. Tesař and Bandalusena [23] investigated a fluid diverter and reported a vortex blocking off one of the outlets, and thus slowing the switching process. The oscillation mechanism of the sweeping jet oscillator, as reported by Ostermann et al. [24], relies heavily on a separation bubble, which is fed by fluid from the feedback tubes, pushing the jet away from its attachment wall. In the device investigated here, essentially no fluid is exchanged between the feedback tubes and the interaction region. In contrast, the detachment of the jet is enabled by reversing fluid from downstream of the interaction region and by fluid from the jet itself.

IV. Conclusions

In this paper, a novel, interpretable reduced-order model of the oscillator flow was built based on spatiotemporally resolved high-fidelity data. In the investigated device, a direct correlation between the pressure difference between the control ports and jet deflection was found, without a phase lag or deadband. This pressure difference is found to be the mechanism for the deflection of the jet, supporting previous models available in the literature. A flow through the feedback tube is induced by the pressure. The onset of this flow is correlated to the decrease of the pressure difference and enables the detachment of the jet from the wall, where the gap between the wall and the jet is filled with fluid from downstream and not from the feedback tube. The reattachment is a combined effect of entrainment of the fluid by the main jet and of the flow through the feedback tube, leading to a low pressure at the corresponding port. This aspect was, so far, not included in any model.

Current models of the switching mechanism do not include the pressure on the nonattached side. In this study, LCSs show a strong reverse flow from the interaction region toward the port from where the jet is separated, enabling the rise of pressure at this port above the temporal mean pressure, and subsequent starting of feedback tube flow. The results presented here suggest inclusion of the feedback tube flow and the reverse flow into future analytical modeling approaches.

The observed coupling of port pressure and jet deflection may be exploited for control purposes, where the exact state of the oscillator needs to be known in order to control either the oscillatory behavior or the effect of the actuator on the flowfield. In such an application, the full state of the actuator may be approximated with just a single pressure sensor measuring the port pressure difference.

These findings may also be used to investigate modifications in the design of the device to increase and adjust its performance. The dependence of the oscillation on the reverse flow between the interaction region and the control port indicates that a larger distance between the control ports could enable an increase in magnitude and a decrease of rise time for this reverse flow. This may lead to a faster oscillation with a higher quality, i.e., higher standard deviation of the velocity at the outlets.

Acknowledgment

This project did not receive special funding.

References

[1] Spyropoulos, C. E., "Sonic Oscillator," *Proceedings of the Fluid Amplification Symposium*, Harry Diamond Labs, Washington, D.C., 1964, pp. 27–52.

[2] Viets, H., "Flip-Flop Jet Nozzle," *AIAA Journal*, Vol. 13, No. 10, 1975, pp. 1375–1379.
https://doi.org/10.2514/3.60550

[3] Zimmerman, W. B., Hewakandamby, B. N., Tesař, V., Bandulasena, H., and Omotowa, O., "On the Design and Simulation of an Airlift Loop Bioreactor with Microbubble Generation by Fluidic Oscillation," *Food and Bioproducts Processing*, Vol. 87, No. 3, 2009, pp. 215–227.
https://doi.org/10.1016/j.fbp.2009.03.006

[4] Cattafesta, L. N., III, and Sheplak, M., "Actuators for Active Flow Control," *Annual Review of Fluid Mechanics*, Vol. 43, 2011, pp. 247–272.
https://doi.org/10.1146/annurev-fluid-122109-160634

[5] Seifert, A., Stalnov, O., Sperber, D., Arwatz, G., Palei, V., David, S., Dayan, I., and Fono, I., "Large Trucks Drag Reduction Using Active Flow Control," *The Aerodynamics of Heavy Vehicles II: Trucks, Buses, and Trains*, Springer, New York, 2009, pp. 115–133.
https://doi.org/10.1007/978-3-540-85070-0_10

[6] Schloesser, P., Soudakov, V., Bauer, M., and Wild, J., "Active Separation Control at the Pylon-Wing Junction of a Real-Scale Model," *AIAA Journal*, Vol. 57, No. 1, 2019, pp. 132–141.
https://doi.org/10.2514/1.J057345

[7] Arwatz, G., Fono, I., and Seifert, A., "Suction and Oscillatory Blowing Actuator," *IUTAM Symposium on Flow Control and MEMS*, Springer, New York, 2008, pp. 33–44.
https://doi.org/10.1007/978-1-4020-6858-4_4

[8] Kim, J., Moin, P., and Seifert, A., "Large-Eddy Simulation-Based Characterization of Suction and Oscillatory Blowing Fluidic Actuator," *AIAA Journal*, Vol. 55, No. 8, 2017, pp. 2566–2579.
https://doi.org/10.2514/1.J055445

[9] Koso, T., Kawaguchi, S., Hojo, M., and Hayami, H., "Flow Mechanism of a Self-Induced Oscillating Jet Issued from a Flip-Flop Jet Nozzle," *JSME-KSME Fluids Engineering Conference*, Vol. 5, JSME, Nagoya, Japan, 2002, pp. 1–6.

[10] Wassermann, F., Hecker, D., Jung, B., Markl, M., Seifert, A., and Grundmann, S., "Phase-Locked 3D3C-MRV Measurements in a Bi-Stable Fluidic Oscillator," *Experiments in Fluids*, Vol. 54, No. 3, 2013, Paper 1487.
https://doi.org/10.1007/s00348-013-1487-5

[11] Gregory, J., and Tomac, M. N., "A Review of Fluidic Oscillator Development," *43rd AIAA Fluid Dynamics Conference*, AIAA Paper 2013-2474, 2013.
https://doi.org/10.2514/6.2013-2474

[12] Epstein, M., "Theoretical Investigation of the Switching Mechanism in a Bistable Wall Attachment Fluid Amplifier," *Journal of Basic Engineering*, Vol. 93, No. 1, 1971, pp. 55–62.
https://doi.org/10.1115/1.3425182

[13] Lush, P., "A Theoretical and Experimental Investigation of the Switching Mechanism in a Wall Attachment Fluid Amplifier," *Proceedings of IFAC Symposium on Fluidics*, Hartford Shire, London, 1968.

[14] Goto, J. M., and Drzewiecki, T. M., "Fluerics 32. An Analytical Model for the Response of Flueric Wall-Attachment Amplifiers," U.S. Army Materiel Command, Harry Diamond Labs. TR 1598, Washington, D.C., June 1972, https://apps.dtic.mil/sti/citations/AD0747761 [retrieved 6 Jan. 2022].

[15] Berkooz, G., Holmes, P., and Lumley, J. L., "The Proper Orthogonal Decomposition in the Analysis of Turbulent Flows," *Annual Review of Fluid Mechanics*, Vol. 25, No. 1, 1993, pp. 539–575.
https://doi.org/10.1146/annurev.fl.25.010193.002543

[16] Gnirß, M., and Tropea, C., "Simultaneous PIV and Concentration Measurements in a Gas-Turbine Combustor Model," *Experiments in Fluids*, Vol. 45, No. 4, 2008, pp. 643–656.
https://doi.org/10.1007/s00348-008-0518-0

[17] Kriegseis, J., Dehler, T., Gnirß, M., and Tropea, C., "Common-Base Proper Orthogonal Decomposition as a Means of Quantitative Data

Comparison," *Measurement Science and Technology*, Vol. 21, No. 8, 2010, Paper 085403.
https://doi.org/10.1088/0957-0233/21/8/085403

[18] Shadden, S. C., Lekien, F., and Marsden, J. E., "Definition and Properties of Lagrangian Coherent Structures from Finite-Time Lyapunov Exponents in Two-Dimensional Aperiodic Flows," *Physica D: Nonlinear Phenomena*, Vol. 212, Nos. 3–4, 2005, pp. 271–304.
https://doi.org/10.1016/j.physd.2005.10.007

[19] Khalighi, Y., Ham, F., Nichols, J., Lele, S., and Moin, P., "Unstructured Large Eddy Simulation for Prediction of Noise Issued from Turbulent Jets in Various Configurations," *17th AIAA/CEAS Aeroacoustics Conference (32nd AIAA Aeroacoustics Conference)*, AIAA Paper 2011-2886, 2011.
https://doi.org/10.2514/6.2011-2886

[20] Vreman, A., "An Eddy-Viscosity Subgrid-Scale Model for Turbulent Shear Flow: Algebraic Theory and Applications," *Physics of Fluids*, Vol. 16, No. 10, 2004, pp. 3670–3681.
https://doi.org/10.1063/1.1785131

[21] Hindmarsh, A. C., "ODEPACK, A Systematized Collection of ODE Solvers," *Scientific Computing*, North-Holland, Amsterdam, 1983, pp. 55–64.

[22] Chapman, D., Kuehn, D., and Larson, H., "Investigation of Separated Flows in Supersonic and Subsonic Streams with Emphasis on the Effect of Transition," NACA TN 3869, 1957.

[23] Tesař, V., and Bandalusena, H., "Bistable Diverter Valve in Microfluidics," *Experiments in Fluids*, Vol. 50, No. 5, 2011, pp. 1225–1233.
https://doi.org/10.1007/s00348-010-0983-0

[24] Ostermann, F., Woszidlo, R., Nayeri, C., and Paschereit, C., "Experimental Comparison Between the Flow Field of Two Common Fluidic Oscillator Designs," *53rd Aerospace Sciences Meeting*, AIAA Paper 2015-0781, 2015.
https://doi.org/10.2514/6.2015-0781

J. Larsson
Associate Editor

3.2 Publication II

M. Fromm, S. Grundmann and A. Seifert, Fluidic FitzHugh-Nagumo oscillator, Physics of Fluids, 37.2, 027115 (2025). DOI: 10.1063/5.0250615.

Reprinted by permission of AIP Publishing LLC.

Author contributions

Task	Responsible author
Experiment design and preparation	Matthias Fromm
Experimental data acquisition	Matthias Fromm
Data Analysis	Matthias Fromm
writing the Manuscript	Matthias Fromm

The second paper expands the previous study by exploring the mechanisms behind fluidic oscillators through the lens of the FitzHugh-Nagumo (FHN) equations, traditionally used for modeling neuronal excitations. The research presents experimental evidence suggesting that fluidic oscillators can be effectively modeled using the FHN system, linking fluid dynamics with electrical analogs. Detailed phase-averaged velocity fields and local pressures were obtained using Particle Image Velocimetry (PIV) and pressure transducers, providing a comprehensive view of the oscillator's behavior. The study revealed a complex interplay of secondary flows within the oscillator that facilitate self-sustained oscillations. This novel approach of using the FHN equations offers a new perspective on the control and prediction of fluidic oscillator performance. The experimental validation strengthens the theoretical model, making it a valuable tool for future research and practical applications in AFC systems.

Physics of Fluids ARTICLE pubs.aip.org/aip/pof

Fluidic FitzHugh-Nagumo oscillator

Cite as: Phys. Fluids **37**, 027115 (2025); doi: 10.1063/5.0250615
Submitted: 26 November 2024 · Accepted: 7 January 2025 ·
Published Online: 5 February 2025

View Online Export Citation CrossMark

Matthias Fromm,[1,a)] Sven Grundmann,[1] and Avraham "Avi" Seifert[2]

AFFILIATIONS

[1]Institute of Fluid Dynamics, University of Rostock, Albert-Einstein-Str.. 2, 18059 Rostock, Germany
[2]Meadow Aerodynamics Laboratory, School of Mechanical Engineering, Faculty of Engineering, Tel Aviv University, 69978 Tel Aviv, Israel

[a)]Author to whom correspondence should be addressed: matthias.fromm@uni-rostock.de

ABSTRACT

Fluidic oscillators display a unique feature: from a constant input flow, they generate an output that alternates both temporally and spatially, all without the necessity for any moving components. However, there have been varying theories proposed to explain the underlying mechanisms. In this study, we provide experimental arguments that the functioning of a single-feedback loop fluidic oscillator can be effectively modeled and interpreted using the Fitzhugh-Nagumo equations. We explore the connection between the Fitzhugh-Nagumo system and the momentum equations, as well as a fluid capacitance. Our findings reveal a complex interplay of secondary flows within the oscillator, which appears to facilitate the self-sustained oscillation.

NOMENCLATURE

A_{fbt}	Cross-sectional area of the feedback tube
C	Fluid capacitance (analogous to electrical capacitance)
d_{fbt}	Diameter of the feedback tube
d_{in}	Inlet nozzle diameter
f	Switching frequency
$f(p_d)$	Cubic polynomial representing the interaction mass flow
$f(V)$	Cubic function representing tunnel diode current in FHN model
FBT	Feedback tube
i	Current in the FitzHugh-Nagumo model
L	Inductance in the FitzHugh-Nagumo model
L_{fbt}	Length of the feedback tube
p_1, p_2	Control port pressures
$p_d = p_1 - p_2$	Pressure difference between control ports
R	Resistance in the FitzHugh-Nagumo model
$Re_{in} = \frac{d_{in}u_{in}}{\nu}$	Inlet Reynolds number
ρ	Density
t	Time
u_{fbt}	Velocity in the feedback tube
u_{in}	Bulk oscillator inlet velocity
$\dot{m}_{fbt}$	Mass flow in the feedback tube
$\dot{m}_{inter}$	Interaction mass flow
$\dot{V}_{in}$	Volume flow rate of the supply flow
μ	Dynamic viscosity
ν	Kinematic viscosity
$\alpha_W = d_{fbt}\sqrt{\frac{\omega\rho}{\mu}}$	Womersley number

I. INTRODUCTION

A particularly interesting member of the family of fluid logic devices is the fluidic oscillator, which creates alternating jets from a steady-state input, without any moving components.[1,2] The geometric configuration enabling this feature is a simple and two-dimensional geometry, which varies between different types of oscillators that have been developed in subsequent research. Derived from the idea of a fluid logic gate and amplification device, the unsteady output flow of fluidic oscillators has been investigated for the enhancement of fluid mixing in various applications from active flow control, micro-bubble generation, and enhancement of heat transfer to applications as a wind shield wiper.[3–9] As an example, a fluidic oscillator may be integrated into the suction side surface of an airplane wing or the airplanes vertical tail. The unsteady output of the oscillator enhances mixing of the boundary layer and thus can delay or even fully suppress flow separation, leading to improved wing performance or eventually replace mechanical flap systems.[4,10–12]

Recent research has dedicated considerable effort into understanding the oscillation mechanism of fluidic oscillators, with particular focus on the sweeping jet oscillator (e.g., Refs. 13–17)

In this paper, we aim to shed a new light on the mechanism of the jet oscillation of the fluid amplifier inspired oscillator (as depicted in Fig. 1). This device comprises the following components (Fig. 1): An inlet nozzle supplies fluid into a chamber formed by two diverging walls which lead to two outlets, which are separated by a splitter. Where the nozzle and the chamber join, the control ports are located, connected to each other by the feedback tube (FBT).

In the research of fluid amplifiers,[18–22] the jet was modeled by means of a jet curvature equation for the case of external control flows or pressures. In the oscillator configuration, the self-sustained oscillations were initially attributed to acoustic pressure waves traveling through the FBT and pulling the jet from side to side.[1] The currently accepted explanation can be summarized as follows (see, e.g.,5). The jet position at the centerline of the device is unstable. Therefore, the jet will initially attach, due to entrainment, natural turbulence, and any small asymmetry, to one of the side walls, where it creates a low pressure region at the control port. The low pressure travels as a wave through the feedback tube toward the opposite control port and draws the jet across, by applying a transverse pressure gradient acting on the jet and accelerating it to move from one side to the other.

However, the oscillation timescale was found to be much slower than expected for a purely acoustic feedback.[2] To overcome this, the explanation of the oscillation mechanism was refined by incorporation of viscous time delays,[23] and a flow through the feedback tube induced by the control port pressure difference was first reported by Koso *et al.*[24]

Here, we propose a new model for the jet switching mechanism based on the FitzHugh-Nagumo (FHN) system of equations, which was developed to describe neuron excitation dynamics.[25,26] In terms of electrical quantities, it reads

$$C\frac{dV}{dt} = f(V) - i, \tag{1a}$$

$$L\frac{di}{dt} = V - Ri. \tag{1b}$$

In Eq. (1), C is a capacity, V denotes voltage, $f(V)$ is a cubic function representing the current through the tunnel diode, and i is the current through inductance L and resistance R. In this paper, we consider the state of fully developed, stable oscillations.

II. METHODS

We obtained phase-averaged velocity fields and local pressures of a generic fluidic oscillator using particle image velocimetry (PIV),

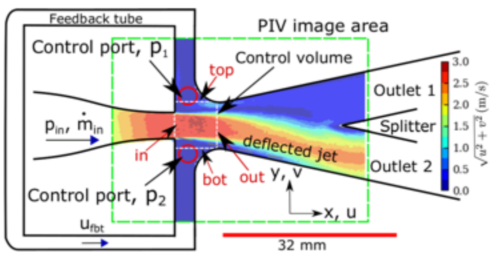

FIG. 1. Oscillator geometry and phase-averaged velocity magnitude field. The red circles correspond to the size of the pressure taps p_1 and p_2. The FBT length is not to scale.

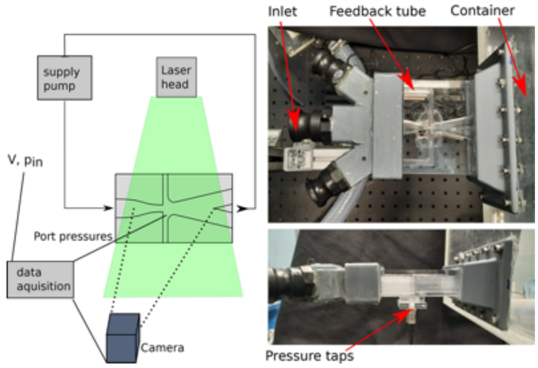

FIG. 2. Experimental setup overview.

synchronized with two Kulite XTM-190 piezo-resistive pressure transducers. The setup is illustrated in Fig. 2. The oscillator model, milled from acrylic glass via Computer Numeric Control (CNC) milling, was mounted externally on a container measuring 1 m × 0.5 m × 0.3 m. The outlet nozzles of the model were flush with the container's front surface to ensure minimal flow interference with the water surface inside.

Table I summarizes the geometry and measurements of the device. The aspect ratio, at 3.6, falls within a range that likely minimizes effects of the top and bottom walls. The narrowest channel width, measuring 5 mm at the junction where the feedback tube connects to the control ports, is small but does not qualify as microfluidic. The reference points determining the length of the FBT vary in the literature. Here, we choose the boundary of the control volume as the reference point where the FBT length is measured from (see Fig. 1).

Water was circulated through the system using a pump, with its suction side positioned inside the container opposite to the model. This setup maintained a consistent supply flow, monitored for total inlet pressure, volume flow rate, and temperature using industry-grade sensors.

Pressure measurements within the oscillator were taken at the control ports, labeled 1 and 2 as depicted in Fig. 1, using the aforementioned pressure transducers mounted flush with the interaction region floor. Each sensor recorded data at a 10 kHz sampling rate, processed through a 5 kHz analog low-pass filter before 16-bit analog-to-digital conversion.

TABLE I. Device geometry.

Parameter	Value
Width of the FBT channels at narrowest point	5.0 mm
Inlet nozzle width	4.98 mm
Height of the channels	18.0 mm
Aspect ratio	3.6
Device length (inlet nozzle to outlet)	100.0 mm
Feedback tube length (main configuration)	0.6 m

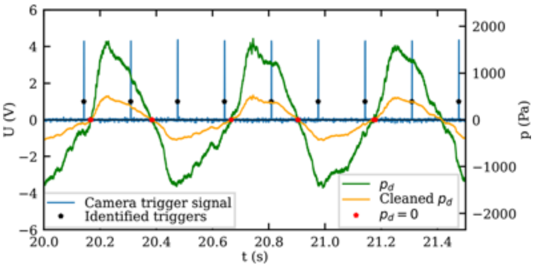

FIG. 3. Phase averaging procedure.

For visualizing the velocity field, PIV was employed at a steady rate of 6 Hz using a commercial double-pulse laser setup. The PIV camera was positioned perpendicularly above the oscillator, and the laser light-sheet was aligned centrally, equidistant from the model's floor and ceiling, to minimize three-dimensional effects. The images captured had a resolution of 1100 x 800 pixels, with interrogation areas of 16 x 8 pixels each and a 50% overlap, yielding a spatial resolution of 0.387 mm by 0.194 mm per vector.

Data synchronization between the PIV camera and pressure sensors was achieved by recording the camera trigger voltage signal alongside the pressure sensor outputs. This enabled the computation of phase-averaged velocity fields during post-processing. Phase-averaging was referenced against the port pressure difference, with $\phi = 0$ defined as the instant of zero pressure difference between the ports occurring in a positive direction ($dp_d/dt > 0$). Prior to searching for the zero crossings, p_d is filtered by applying a cross correlation with a single extracted period (similarly as described in Ref. 27). Figure 3 shows a sample time span from the measurement detailing the signals used to compute the phase-averaged properties.

III. RESULTS AND DISCUSSION

In the following, we will primarily discuss the results of an individual experiment run conducted under the conditions summarized in Table II. Note that the oscillation frequency was measured as $f = 2$ Hz, but the characteristic time of acoustic wave transmission through the feedback tube is $t = 0.4$ ms, which would result in an oscillation frequency at the order of kHz, if pressure waves played a primary role in the switching mechanism.

Consider the two-dimensional control volume between the control ports (Fig. 1). The pressures p_1 and p_2 are assumed to be uniform over the extent of their respective control port and thus along the upper and lower boundaries of the control volume. The control port pressure difference is defined as $p_d = p_1 - p_2$. The phase angle $\phi = 0$ is defined as $p_d = 0$ when $dp_d/dt > 0$. A full cycle corresponds to the jet attaching to one side, switching over to the other and returning to the first.

TABLE II. Experimental results of the main configuration.

Parameter	Value
Bulk inlet velocity v	2.8 m/s
Inlet flow rate $\dot{V}_{in}$	15.0 l/min
Switching frequency f	2 Hz
Wormersley number α	27.74

For the current control volume, the conservation of lateral momentum states

$$\int_A \frac{\partial v}{\partial t}\, dA + \int_{out} uv\, dS - \int_{in} uv\, dS + \int_{top} v^2\, dS - \int_{bot} v^2\, dS = \frac{1}{\rho} p_d S_{top}, \quad (2)$$

where *in*, *out*, *top,* and *bot* denote the inlet, outlet, upper, and lower boundaries of the control volume, as labeled in Fig. 1; A is the area and S denotes the individual boundaries. We evaluate Eq. (2) numerically from the measured data, finding that the force exerted by the pressure difference $p_d A_{top}$ accelerates the jet fluid in the y-direction while it passes through the control volume and balances the outflow of lateral momentum [Fig. 4(a)]. Notably, the jet enters the control volume with nonzero vertical momentum, $\dot{P}_{in}$, indicating that there is an upstream effect of the jet deflection. The temporal derivative of the vertical momentum, $\frac{dP}{dt}$, is small compared to the magnitudes of the pressure force and the momentum fluxes [Fig. 4(a)], supporting the assumption of quasi-steady flow previously used for fluid amplifiers.[18,19] At the same time, the momentum transported by the FBT ($\dot{P}_{fbt}$) is of the same order of magnitude as the unsteady term [see Fig. 4(b), though with distinctive differences around $\Phi = 0°$ and $180°$], which indicates that the FBT flow may affect the switching, as will be subsequently discussed.

To further assess the dynamic behavior of oscillatory flows within the feedback tube channel, the Womersley number is evaluated. It is defined as

$$\alpha_W = d_{fbt} \left(\frac{\omega \rho}{\mu}\right)^{\frac{1}{2}}. \quad (3)$$

Here, d_{fbt} is the characteristic length, in this case the diameter of the feedback tube, ω is the angular frequency of the oscillation, ρ is the fluid density, and μ is the dynamic viscosity of the fluid. The Womersley number characterizes the relative importance of inertial forces to viscous forces in oscillatory flow and is particularly useful in predicting the flow behavior in channels and blood vessels where the flow may be pulsatile. Evaluated to $\alpha_W = 27.74$, the Wormersley number indicates fully developed oscillatory flow in the FBT.

The relation between the FBT flow and p_d is modeled as in the study of Woszidlo *et al.*[24] using an unsteady, viscous-loss corrected Bernoulli equation for a streamline through the FBT from control port 1 to 2 (conf. Figure 1). Given incompressibility, the result is

$$\frac{\partial u}{\partial t} = \frac{1}{\rho L_{fbt}} (p_d - \lambda u), \quad (4)$$

with L_{fbt} being the FBT length; the (constant) fluid density, ρ; and λ approximating the viscous losses of laminar flow through a tube (Hagen–Poiseuille),

$$\lambda = 32 \frac{L_{fbt} \nu \rho}{d_{fbt}^2}, \quad (5)$$

where d_{fbt} is the FBT diameter and ν is the kinematic viscosity. Furthermore, we calculate the mass flow in the FBT as $\dot{m}_{fbt} \approx \rho A u_{fbt}$, since the FBT velocity is observed as spatially nearly uniform at the

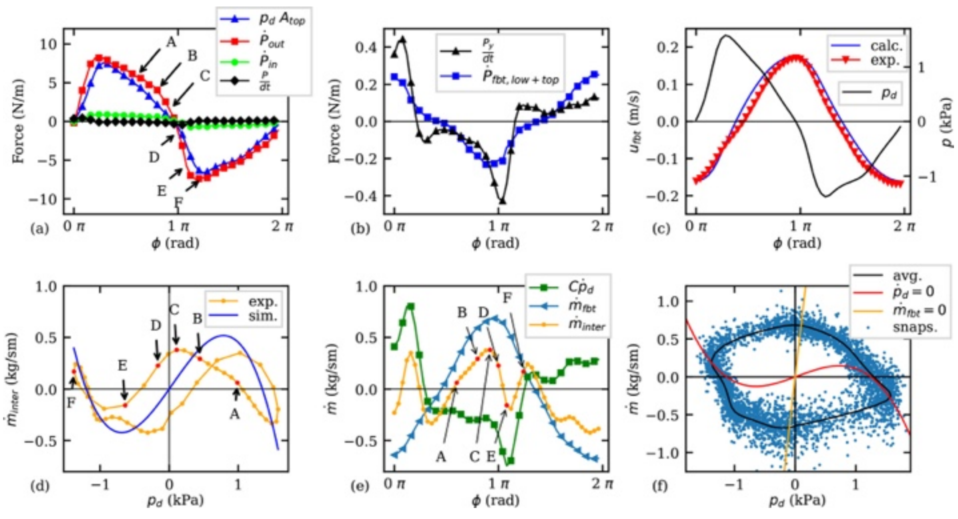

FIG. 4. Phase-averaged momentum terms obtained from PIV for one oscillation cycle at a flow rate of 15 l/min. Every second data point marked in a, b, and e. (a and b) Momentum terms of Eq. (2). (c) Measured vs calculated FBT velocity u_{fbt} using experimental pressure difference p_d. (d) Interaction flow $\dot{m}_{inter}$ vs p_d. (e) Terms of Eq. (1a) evaluated from measurement data. (f) Phase-space and nullclines of p_d and FBT massflow $\dot{m}_{fbt}$. Dots indicate instantaneous data.

measurement location. Figure 4(c) shows that Eq. (4), evaluated using the measured p_d, well approximates the measured data.

To analyze the flows in the control volume, finite-time Lyapunov exponents (FTLE)[28] are computed from the velocity fields. Ridges in the FTLE field represent mixing boundaries, referred to as Lagrangian coherent structures (LCS), across which no fluid exchange occurs. Based on this, the fluid of the main jet can be distinguished from fluid originating from the feedback tubes or from downstream. In Fig. 5, several secondary flows can be identified next to the main jet, which is bounded by distinct LCS at all times. In Fig. 5B, the jet is attached to the upper wall and fluid enters the control volume from the FBT at the side where the jet is attached (FBT flow). Part of it joins the main jet due to entrainment and leaves the control volume toward the outlet (entrainment flow). On the detached side (lower wall in Fig. 5B), a reverse, upstream directed flow develops, originating from the outlet. Part of this reverse flow is entrained back toward the outlets. The remaining fluid flows into the control port and enters the FBT (reverse flow). This flow is enabled by the downstream increase in pressure, as the jet decelerates toward the outlets.[22,29] When the jet just attaches to the lower side (Fig. 5F), a small part of the jet stagnates against the lower wall and fluid is diverted from the jet and redirected into the associated control port (stagnation flow). Note that these flows are dependent on the deflection of the jet, since the jet restricts or opens up space for the flows: the reverse flow is inhibited when the jet takes the center; the stagnation flow is only present at near-maximum deflection.

Let us now use p_d as a "lumped" state variable of the jet vertical deflection, $p_d \propto \alpha$, corresponding to the voltage variable in Eq. (1a). The jet is modeled here as a flexible membrane, which divides the control volume into three sub-spaces: the jet itself, taking the role of the membrane, and the top and lower halves of the remainder of the control volume. These regions cannot interchange fluid directly, as indicated by the LCS bounding the jet, forming a jet barrier capacitance.[22] Therefore, a change in the in- or outflow of mass to the two parts of the control volume governs the temporal evolution of p_d. We introduce the *interaction flow* $\dot{m}_{inter}$ as the resulting net flow from reverse, entrainment and stagnation flows and associate it to the function $f(V)$ in Eq. (1a). The time-dependent balance of flows for one control port then reads

$$C\dot{p}_d = \dot{m}_{inter} - \dot{m}_{fbt}, \tag{6}$$

representing the temporal derivative of p_d with capacitance C. $\dot{m}_{fbt}$ takes the role of the current i in Eq. (1a). Thus, Eq. (1b) represents the temporal derivative of $\dot{m}_{fbt}$, directly resembling Eq. (4). The resulting equation system adapted to the oscillator thus becomes

$$C\frac{dp_d}{dt} = f(p_d) - \rho A_{fbt} u_{fbt}, \tag{7a}$$

$$\frac{du_{fbt}}{dt} = \frac{1}{\rho L_{fbt}}\left(p_d - 32\frac{L_{fbt}\nu\rho}{d_{fbt}^2}u_{fbt}\right), \tag{7b}$$

with $f(p_d) = \dot{m}_{inter}$. To visualize this idea, the electric circuit proposed by Nagumo *et al.*[26] is schematically adapted to the oscillator geometry in Fig. 6.

While $\dot{m}_{fbt}$ can be computed according to Eq. (4) from the velocity data as presented above, $\dot{m}_{inter}$ cannot easily be determined. Particularly, the magnitude of the stagnation flow is nearly impossible to obtain from experimental data, and no analytical assessment is available here. Therefore, we performed a simulation of Eq. (7) using the already derived parameters for Eq. (7b) and approximate $f(p_d)$ with a symmetric cubic polynomial (as commonly done in applications

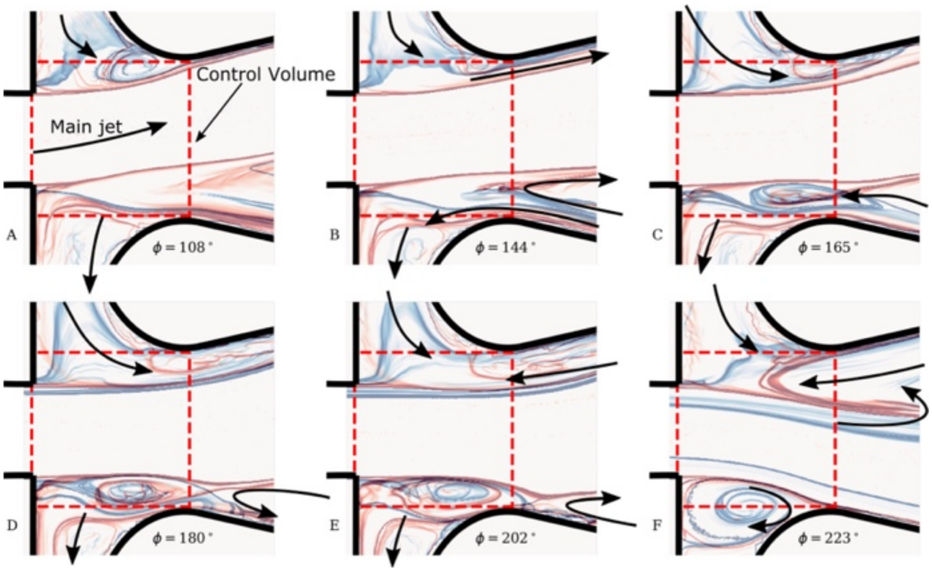

FIG. 5. Visualization of coherent flow structures inside the oscillator. Repelling (blue) and attracting (red) FTLE computed from the phase-averaged velocity fields. Colormap and transparency adjusted to highlight regions of high FTLE.

of the FHN), $f(p_d) = p_d(p_d^2 - r)$ with root r, fitting the values for C and the roots of the polynomial to the experimental data[30] (Fig. 7).

With the thereby derived value for C, we calculate $\dot{m}_{inter} = C\dot{p}_d - \dot{m}_{fbt}$ and compare it to the optimal polynomial in Fig. 4(d).

The measured data exhibit a clear cubic relationship alongside a hysteresis and minor asymmetry. This is remarkable because the average flow fields show near perfect symmetry and equal flow distribution between the outlets. Consequently, we assume the reason for the deviation from the perfect model to be twofold: first, the secondary flows in the control ports, summarized by m_{inter}, are not necessarily strictly two-dimensional, but could have three-dimensional components that we were not able to measure with the 2D PIV setup. Second, those 3D components could be amplified by small asymmetries in the geometry of the oscillator model, due to manufacturing and assembly inaccuracies, and potentially asymmetric inflow conditions, e.g., due to swirl in the inflow tubing. Note also that the accurate measurement and analysis of flows of such small scale poses known challenges to (non-micro) PIV. Nevertheless, the cubic approximation will be valuable for the use in the FHN equations. Figure 4(e) presents the obtained terms of Eq. (7a).

Concluding, a switching half-cycle, i.e., the transition of the jet from the upper to lower wall, is composed of the following steps (the letters correspond to the markings in Fig. 4 and the subfigures of Fig. 5):

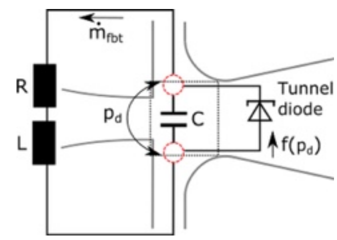

FIG. 6. Schematic electric-fluid equivalent circuit for the fluidic oscillator.

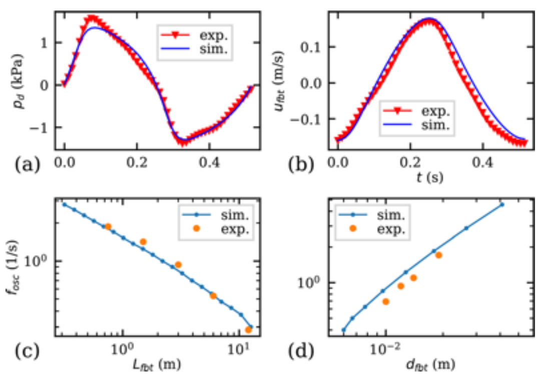

FIG. 7. Experimental vs simulated (a) p_d and (b) u_{fbt}. Experimental and simulated switching frequency with different FBT (c) length and (d) diameter.

(A) The jet is fully attached; $\dot{m}_{fbt}$ is lightly developed, feeding fluid to the attached port, and p_d is decreasing consequently.
(B) A thin layer of fluid forms between upper wall and jet, removing volume from upper port.
(C) $\dot{m}_{fbt}$ increases until p_d approaches zero [Fig. 4(c)].
(D) The jet centers between walls and interrupts the upstream flow at the lower port; the upper port is opened to supply from downstream; thus, the interaction flow decreases sharply; $\dot{m}_{fbt}$ is still transporting fluid from the lower port to the upper port. The pressure gradient changes direction.
(E) The pressure rapidly decreases at the lower port and the jet simultaneously bends into the new direction.
(F) A stagnation streamline forms against the wall and $\dot{m}_{inter}$ changes sign again, limiting the maximum value and even relaxing p_d.

Figure 8 (Multimedia view) displays a full switching cycle of the most relevant terms and the corresponding FTLE fields in an animated fashion. The phase-space and the resulting nullclines $\dot{u}_{fbt} = \dot{p}_d = 0$ of the identified system are shown in Fig. 4(f).

Comparing these observations to results reported for other oscillator types shows significant differences. For the sweeping jet oscillator, the separation of the jet from the wall was found to be due to a separation bubble filled up by FBT fluid.[31] In that case, the dynamic relies on the integral of the FBT flow rather than on its amplitude, as is the case reported here.

The geometrical parameters of the oscillator are known to influence the oscillation frequency, particularly the FBT length and diameter.[1,2,23,32] Due to the non-linearity in $f(p_d)$, the oscillation frequency cannot be obtained analytically from Eq. (7). Thus, we perform simulations with varying L_{fbt} in Eq. (7b) and extract the oscillation frequency using Fast Fourier Transform. The predicted frequencies align closely with the experimental values and are consistent with previously published data[1,2,23,32] [Fig. 7(c)].

Experimentally, a change in the FBT diameter is realized in such a way that the control port size is kept constant and the tube diameter enlarges after a short distance. To address this, Eq. (7b) needs to be expanded to

$$2\int_{l_1} \frac{\partial u_1}{\partial t} ds + \int_{L-2l_1} \frac{\partial u_2}{\partial t} ds = \frac{1}{\rho} \int_L \frac{\partial p}{\partial s} ds, \tag{8}$$

where l_1 is the part of the FBT with original diameter and $L - 2l_1$ is the part with the varied diameter. We neglect l_1 by assuming $l_1 \ll L$; thus, Eq. (8) becomes

$$\frac{du}{dt} = \frac{1}{\rho L} \left(\frac{d_2^2}{d_1^2} p_d - \lambda u \right). \tag{9}$$

Again, good agreement is achieved, though the range of experimentally accessible diameters was limited due to technical reasons [Fig. 7(d)]. The simulated frequencies are slightly but consistently higher than the measured data. This can be attributed to additional losses due to the changes in cross section and additional bends of the FBT due to manufacturing restrictions, which are unaddressed in the simulation model. This is consistent with the observation that the deviation

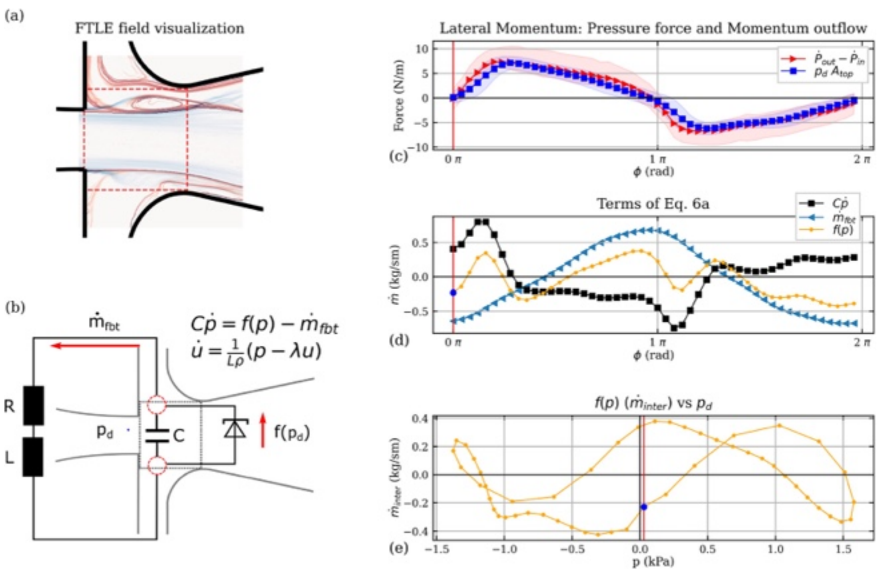

FIG. 8. Animated display of a full switching cycle including: (a) the FTLE fields; (b) equivalent circuit, where arrow directions and length correspond to the value of the parameter; (c) pressure force and outflowing momentum (shaded areas correspond to two times the respective standard deviation); (d) terms of Eq. (7a); and (e) the relationship between p_d and the interaction mass flow, $\dot{m}_{inter}$. Multimedia available online.

between simulated and measured data slightly widens with smaller FBT diameters.

Another influence on the switching frequency is the inlet Reynolds number, $\mathrm{Re}_{in} = \frac{d_{in} u_{in}}{\nu}$, with the bulk inlet velocity u_{in} and the scale of the oscillator, represented by the inlet nozzle diameter, d_{in}. However, these effects are competing. An increase in inlet velocity increases the oscillation frequency and an increase in size lowers the frequency, despite both increasing Re_{in}.[2,23] This aligns with the principles of scaling, which state that the characteristic frequency of any device is inversely proportional to its size. Figure 9 shows that the waveform of the phase-averaged port pressure difference is preserved over the investigated range of Re_{in}, indicating that $f(p_d)$ may scale in a linear and self-similar manner with respect to Re_{in}.

IV. CONCLUSION

We demonstrated the applicability of the FHN equations for the modeling of fluidic oscillators based on the fluid amplifier principle. Experimental data showed that complex flows inside the oscillator are responsible for the development of the oscillations instead of an acoustic feedback. The non-harmonic output of the oscillator is due to the non-linearity arising from the self-accelerating attachment of the jet to the side walls. The characteristics of the FBT flow, which takes the role of the relaxation variable, were successfully connected to fluid properties and the geometry details. The length and diameter of the FBT are confirmed to control the switching frequency, but based on different effects as previously reported. The model-predicted oscillation frequencies are in quantitative agreement with the measurements despite the approximated assumption of a pure polynomial for $f(p_d)$.

Certainly, several questions remain open, including the modeling of Reynolds number dependence; a direct evaluation of $f(p_d)$ and the dependence of the latter on geometrical parameters; and the ability of the model to capture transient effects. On a practical level, the model may be used to guide design decisions, e.g., choosing appropriate FBT parameters for a desired frequency. For applications involving the control of the oscillator flow or using the oscillator to control external flows, the FHN model may provide valuable insight into the dynamics and may enhance the applicability in new areas, such as the emerging field of soft robotics.[33]

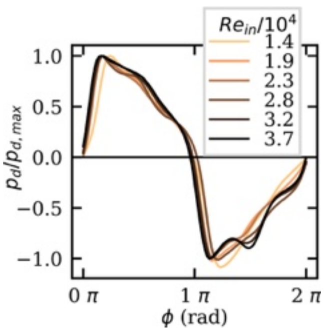

FIG. 9. Experimentally obtained, phase-averaged, normalized port pressure difference p_d for various Re_{in}.

ACKNOWLEDGMENTS

M. F. acknowledges support by the German Federal Ministry of Economic Affairs and Climate Action under Grant No. 03SX496E. A.S. was actively involved in the initial draft but, due to his passing, was unable to contribute to the current version. Nonetheless, his contributions to this work were indispensable.

AUTHOR DECLARATIONS

Conflict of Interest

The authors have no conflicts to disclose.

Author Contributions

Matthias Fromm: Conceptualization (lead); Funding acquisition (equal); Investigation (lead); Software (lead); Validation (lead); Visualization (lead); Writing – original draft (lead); Writing – review & editing (lead). **Sven Grundmann:** Conceptualization (equal); Funding acquisition (equal); Project administration (lead); Supervision (equal); Writing – review & editing (equal). **Avraham "Avi" Seifert:** Conceptualization (equal); Formal analysis (equal); Supervision (equal); Writing – review & editing (equal).

DATA AVAILABILITY

The data that support the findings of this study are available from the corresponding author upon reasonable request.

REFERENCES

[1] C. E. Spyropoulos, "Sonic oscillator," in *Proceedings of the Fluid Amplification Symposium* (Defense Technical Information Center, 1964), pp. 27–52.
[2] H. Viets, "Flip-flop jet nozzle," AIAA J. **13**, 1375–1379 (1975).
[3] A. Seifert, O. Stalnov, D. Sperber, G. Arwatz, V. Palei, S. David, I. Dayan, and I. Fono, "Large trucks drag reduction using active flow control," in *The Aerodynamics of Heavy Vehicles II: Trucks, Buses, and Trains* (Springer, 2009), pp. 115–133.
[4] M. Bauer, J. Lohse, F. Haucke, and W. Nitsche, "High-lift performance investigation of a two-element configuration with a two-stage actuator system," AIAA J. **52**, 1307–1313 (2014).
[5] R. Woszidlo and O. Krüger, "Editorial for the special issue on fluidic oscillators: Devices and applications," Fluids **7**, 91 (2022).
[6] V. Tesař and H. Bandalusena, "Bistable diverter valve in microfluidics," Exp. Fluids **50**, 1225–1233 (2011).
[7] V. Tesař, "Fluidic oscillators mediating generation of microbubbles (survey)," Fluids **6**, 77 (2021).
[8] R. W. Warren, (1962)."Fluid oscillator," US Patent 3,016,066.
[9] L. N. Cattafesta and M. Sheplak, "Actuators for active flow control," Annu. Rev. Fluid Mech. **43**, 247–272 (2011).
[10] M. Y. Andino, J. C. Lin, A. E. Washburn, E. A. Whalen, E. C. Graff, and I. J. Wygnanski, "Flow separation control on a full-scale vertical tail model using sweeping jet actuators," in *53rd AIAA Aerospace Sciences Meeting* (ARC, 2015), p. 0785.
[11] J. C. Lin, M. Y. Andino, M. G. Alexander, E. A. Whalen, M. A. Spoor, J. T. Tran, and I. J. Wygnanski, "An overview of active flow control enhanced vertical tail technology development," in *54th AIAA Aerospace Sciences Meeting* (ARC, 2016), p. 0056.
[12] J. McLean, J. Crouch, R. Stoner, S. Sakurai, G. Seidel, W. Feifel, and H. Rush, "Study of the application of separation control by unsteady excitation to civil transport aircraft," Techical Report (NASA, 1999).
[13] X. Wen, Z. Li, L. Zhou, C. Yu, Z. Muhammad, Y. Liu, S. Wang, and Y. Liu, "Flow dynamics of a fluidic oscillator with internal geometry variations," Phys. Fluids **32**, 075111 (2020).

[14]R. Woszidlo, T. Stumper, C. Nayeri, and C. O. Paschereit, "Experimental study on bluff body drag reduction with fluidic oscillators," in *52nd Aerospace Sciences Meeting* (AIAA, 2014), p. 0403.
[15]M. Sieber, F. Ostermann, R. Woszidlo, K. Oberleithner, and C. O. Paschereit, "Lagrangian coherent structures in the flow field of a fluidic oscillator," Phys. Rev. Fluids **1**, 050509 (2016).
[16]F. Ostermann, R. Woszidlo, C. N. Nayeri, and C. O. Paschereit, "Properties of a sweeping jet emitted from a fluidic oscillator," J. Fluid Mech. **857**, 216–238 (2018).
[17]A. Spens, P. J. Brandt, and J. P. Bons, "Characterization of out-of-plane curved fluidic oscillators," AIAA J. **62**, 1563–1573 (2024).
[18]P. Lush, "A theoretical and experimental investigation of the switching mechanism in a wall attachment fluid amplifier," in Proceedings of IFAC Symposium on Fluidics (1968).
[19]M. Epstein, "Theoretical Investigation of the Switching Mechanism in a Bistable Wall Attachment Fluid Amplifier," J. Basic Eng. **93**, 55–62 (1971).
[20]J. M. Goto and T. M. Drzewiecki, "Fluerics 32. an analytical model for the response of flueric wall-attachment amplifiers" (US Army Materiel Command, Harry Diamond Laboratories, 1972).
[21]F. Brown and R. Humphrey, "Dynamics of a proportional fluidic amplifier: Part 2," J. Basic Eng. **92**, 312 (1970).
[22]J. M. Kirshner, *Design Theory of Fluidic Components* (Academic Press, 2012).
[23]G. Arwatz, I. Fono, and A. Seifert, "Suction and oscillatory blowing actuator," in *IUTAM Symposium on Flow Control and MEMS* (Springer, 2008), pp. 33–44.
[24]T. Koso, S. Kawaguchi, M. Hojo, and H. Hayami, "Flow mechanism of a self-induced oscillating jet issued from a flip-flop jet nozzle," in *JSME-KSME Fluids Engineering Conference* (Citeseer, 2002), Vol. 5.
[25]R. FitzHugh, "Impulses and physiological states in theoretical models of nerve membrane," Biophys. J. **1**, 445–466 (1961).
[26]J. Nagumo, S. Arimoto, and S. Yoshizawa, "An active pulse transmission line simulating nerve axon," Proc. IRE **50**, 2061–2070 (1962).
[27]F. Ostermann, R. Woszidlo, C. N. Nayeri, and C. O. Paschereit, "Phase-averaging methods for the natural flowfield of a fluidic oscillator," AIAA J. **53**, 2359–2368 (2015).
[28]S. C. Shadden, F. Lekien, and J. E. Marsden, "Definition and properties of Lagrangian coherent structures from finite-time Lyapunov exponents in two-dimensional aperiodic flows," Phys. D **212**, 271–304 (2005).
[29]M. Fromm, J. Kim, A. Seifert, J. Kriegseis, and S. Grundmann, "Flow patterns of self-sustained oscillations in fluidic diverters," AIAA J. **60**, 4207–4214 (2022).
[30]A. C. Jensen, S. Ditlevsen, M. Kessler, and O. Papaspiliopoulos, "Markov chain Monte Carlo approach to parameter estimation in the Fitzhugh-Nagumo model," Phys. Rev. E **86**, 041114 (2012).
[31]F. Ostermann, R. Woszidlo, C. Nayeri, and C. Paschereit, "Experimental comparison between the flow field of two common fluidic oscillator designs," in *53rd AIAA Aerospace Sciences Meeting* (ARC, 2015), p. 0781.
[32]J. McDonough, R. Law, J. Kraemer, and A. Harvey, "Effect of geometrical parameters on flow-switching frequencies in 3d printed fluidic oscillators containing different liquids," Chem. Eng. Res. Des. **117**, 228–239 (2017).
[33]M. Wehner, R. L. Truby, D. J. Fitzgerald, B. Mosadegh, G. M. Whitesides, J. A. Lewis, and R. J. Wood, "An integrated design and fabrication strategy for entirely soft, autonomous robots," Nature **536**, 451–455 (2016).

3.3 Publication III

M. Fromm, T. Bestier, S. Brüns, F. Kluwe, A. Hylla, F. Matin, A. Seifert, and S. Grundmann. Active flow control applied to a ship rudder model. Ship Technology Research, 71.1 (2024). DOI: 10.1080/09377255.2023.2275373.

Reprinted by permission of Taylor and Francis Group.

Author contributions

Task	Responsible author
Experiment design and preparation	Matthias Fromm
Experimental data acquisition	Matthias Fromm
Data Analysis	Matthias Fromm
writing the Manuscript	Matthias Fromm

Building on the foundational knowledge laid out by the previous two papers, the third paper applies the derived insights to the practical hydrodynamic problem: flow separation on a ship rudder. By equipping different rudder models with AFC systems that use fluidic oscillators, the study demonstrates significant improvements in delaying flow separation and enhancing lift forces. This application is particularly relevant given the maritime industry's focus on reducing fuel consumption and emissions. The comparative analysis between aerodynamic and hydrodynamic applications of AFC highlights the unique challenges and opportunities in each field, providing a comprehensive perspective on the versatility and potential of AFC technologies in a maritime context.

SHIP TECHNOLOGY RESEARCH (SCHIFFSTECHNIK)
https://doi.org/10.1080/09377255.2023.2275373

Active flow control applied to a ship rudder model

Matthias Fromm [a], Tobias Bestier[a], Sören Brüns[b], Jörn Kröger[b], Florian Kluwe[b], Alexander Hylla[c], Farhan Matin[c], Avraham "Avi" Seifert[d] and Sven Grundmann[a]

[a]Institute of Fluid Dynamics, University of Rostock, Rostock, Germany; [b]Hamburgische Schiffbau-Versuchsanstalt GmbH, Hamburg Ship Model Basin, Hamburg, Germany; [c]Damen Marine Components, Van der Velden Barkemeyer GmbH, Hamburg, Germany; [d]Meadow Aerodynamics Laboratory, School of Mechanical Engineering, Faculty of Engineering, Tel Aviv University, Tel Aviv, Israel

ABSTRACT

The improvement of the performance and efficiency of hydrodynamic control surfaces such as ship rudders is a long sought goal, given economic considerations and the ecological impact of the shipping sector. One major problem limiting the performance of rudders is flow separation at high deflection angles. In this paper, we address this problem using active flow control, a technique first proposed in aerodynamics. A small scale and a large-scale rudder model with realistic geometry were manufactured and equipped with an active flow control system employing the method of pulsed blowing. The actuation system was extensively characterized. Towing tank experiments were conducted up to a Reynolds number of 1.33×10^6. Data included force measurements for the large-scale model and flow field and force measurements for the small-scale model. The impact of the active control on the flow fields around the small-scale model was characterized. The delay of the flow separation towards a higher angle of attack, accompanied with an increase of the maximum lift forces, was demonstrated for both models.

ARTICLE HISTORY
Received 29 August 2022
Accepted 20 July 2023

KEYWORDS
Active flow control; ship rudder; separation control; fluidic oscillator; towing tank; particle image velocimetry

1. Introduction

Reducing the fuel consumption of all kinds of vehicles has been one of the central answers to the challenge of reducing greenhouse gas emissions and global warming. In this context, fluid mechanics research faces the difficult task of developing more efficient lift and control surfaces (or flow exposed geometries in general), since the reduction of drag directly translates to reduced fuel consumption.

The application of Active Flow Control (AFC) has been proposed as a promising approach towards this goal. AFC is the modification of the natural flow state of some body using a form of local energy input to the boundary layer. AFC can be used for a number of targets, including noise reduction, thrust vectoring or mixing enhancement. The most important application in the context of wings and control surfaces is the suppression and delay of flow separation. With the delay of separation or reattachment of separated flow, lift and drag characteristics of aerodynamic surfaces can be improved. This has been impressively demonstrated several times in the context of aerodynamic problems, from simplified lab flow settings to full-scale investigations on airplanes and trucks (Seifert et al. 1993, 2009; Lin et al. 2016; Whalen et al. 2016; Andino et al. 2015; Schloesser et al. 2019; Seele et al. 2012).

Ship rudders and other hydrodynamic control surfaces are subject to flow separation as well, limiting, e.g. the maximum steering forces and consequently the ability to maneuver. Additionally, typical rudders are designed for loads occurring only for very short durations, e.g. during harbour maneuvers, and most of the time the ship's rudder is deflected at small Angles of Attack (AoA) only (Zelazny 2014). Despite this, drag is obviously created the entire time the ship is moving, which is a situation similar to the vertical tail of commercial aircraft, where AFC has been successfully demonstrated (Andino et al. 2019; Whalen et al. 2016). If the hydrodynamic performance of a ship rudder would be enhanced by employing AFC, several scenarios are possible: Without modifying the original rudder geometry and size, higher forces can be obtained when the AFC system is operated, leading to a narrower turning radius and enhanced maneuverability in critical situations. Another option is to reduce the size of the rudder in the same amount the AFC system is able to increase the steering force, thus leading to reduced drag force at all conditions due to the smaller size. In both cases, the AFC system is only operated when needed and energy is only invested during operation. See Liu and Hekkenberg (2017) for a comprehensive review of ship rudder design and operating conditions.

There are some differences between an AFC application on an aircraft and the hydrodynamic application proposed in the current work. The foil geometries used for ship rudders are usually of high

CONTACT Matthias Fromm matthias.fromm@uni-rostock.de, matthias.mfr@gmail.com Institute of Fluid Dynamics, University of Rostock, Albert-Einstein-Str. 2, Rostock 18059, Germany

thickness but comparatively low aspect ratio. The rudder operates in the wake of the ships hull and the slipstream of the propeller, which leads to a high degree of flow inhomogeneity and strong cross-flow components. Typical full-scale chord-length rudder Reynolds numbers can vary between 5×10^5 for small yachts and 1×10^8 for large, fast vessels (Liu and Hekkenberg 2017; Molland and Turnock 2011). Surface effects may influence the performance of the rudder, up to the point where the rudder is only partly submerged when the ship operates in ballast conditions.

The available literature in this field covers only a limited scope. Constant blowing techniques employing the Coanda effect were investigated on flapped rudders (Oh et al. 2003; Choi and Kim 2004; Ahn et al. 1999, 2004; Gim 2017) and horn-type rudders (Seo et al. 2017). However, these investigations were conducted at low Reynolds numbers, used small scale models and mostly investigated the properties of the infinite foil using endplates. Pulsed blowing, the state-of-the-art method of aerodynamic AFC, has not been applied so far for realistic ship rudder geometries at relevant Reynolds numbers.

In this paper, we aim to demonstrate the potential for the use of AFC in the maritime sector, specifically on a ship rudder. We develop and examine a novel AFC system for the control of flow separation on a small-scale and a near full-scale flap-less ship rudder model. The central aspect is to demonstrate the feasibility and benefits of applying AFC to a ship rudder model. In this work, the rudder model geometry and experimental setup were chosen to be as close as possible to the geometry and aspect ratio of full-scale ship rudders and will be investigated without a hull or propeller up front. Measurements of lift and drag forces and the corresponding flow field around the models were used to investigate the influence of varying actuation intensities quantitatively and qualitatively. The small-scale model was used for extensive experiments including Particle Image Velocimetry (PIV) and force measurements in a small towing tank. The large-scale model was investigated in a large towing tank and serves as a validation of the small-scale experiments at higher Reynolds numbers and near-full size system operation.

The outline of the paper is as follows. The current state of the art of AFC for aerodynamic applications will be reviewd in Section 2. This summary is not meant to be exhaustive, but to provide an introduction and context to the system developed in this study. For an in-depth review of the topic, the reader is referred to, e.g. (Greenblatt and Wygnanski 2000; Scott Collis et al. 2004). The small-scale rudder model and the actuation system proposed for this model are presented in Sections 3 and 4 presents the small-scale experimental setup. The actuation system is described in Section 5. The small-scale towing experiments are presented and discussed in Section 6. In Section 7, the large-scale model, a limited characterization of its actuation system and the corresponding towing tank results are presented. The conclusions can be found in Section 8.

2. Introduction to active flow control

In the following, the current state of the art of Active Flow Control (AFC) technology as well as relevant fluid mechanics background will be briefly summarized. Following the roadmap proposed by Scott Collis et al. (2004) for the development of new AFC applications, the target, mechanism, method and enabling technology will be assessed for the actuation system of the rudder model. The target of the system in development is Boundary Layer (BL) separation control. Flow separation is the detachment of the flow along a surface from that surface, accompanied by near wall reversed flow downstream of the separation point. This separation point is defined as the point with zero wall normal velocity gradient, i.e. where the wall shear stress approaches zero, namely:

$$\tau_{wall} = \eta \frac{\mathrm{d}u}{\mathrm{d}y} = 0. \tag{1}$$

Hence, the mechanism to delay BL separation is to enhance near-wall streamwise momentum upstream of the natural separation point. This enables the boundary layer to surmount an adverse pressure gradient and to reach the inviscid performance limit of the aerodynamic surface (Scott Collis et al. 2004). Over the last decades, a number of methods emerged to achieve skin friction enhancement. Today, the method considered as the most mature and capable is the addition of momentum flux into the boundary layer on the suction side of the foil using a net mass flow, combined with redistribution of momentum inside the boundary layer. The latter is achieved by introducing unsteady momentum and thereby creating favourable vortex structures which transport high momentum fluid from the outer region of the flow closer to the wall. This method is commonly referred to as Pulsed-Jet-Actuation (PJA). With sufficient addition or redistribution of momentum, a naturally occurring flow separation can be partly or fully suppressed. If, following complete flow attachment, the level of momentum addition is further increased, the forces acting on the foil increase further as well. This operation regime is termed circulation control, and the only limit for the resulting forces is the availability of the power source. It should be noted though, that the efficiency, that is, the relative increase of the lifting force times the freestream velocity per invested input power, is reported to diminish sharply in this regime (Scott Collis et al. 2004).

The enabling technology for the use of PJA is a suitable actuation system. In general, high momentum fluid jets are introduced into the boundary layer through tangential slots or openings in the surface of the foil. For the creation of the unsteady jets, fluidic oscillators have been proposed as a simple and reliable alternative to fast-switching valves, with extensive research exploring different actuator designs and particular implementations in bench top (Arwatz et al. 2008), prototype (Seifert et al. 2004) and full scale (Seifert et al. 2009; Lin et al. 2016; Seele et al. 2012) studies. The development of fluidic oscillators started in the 1960's, attributed to Spyropoulos (1964) and Warren (1962), for usage in fluid logic systems. Their common characteristic is the ability to create temporally and spatially alternating jets from a steady-state input, without any moving components at play. This behaviour is achieved using a diverging geometry with a bi-stable flow regime and an internal feedback mechanism, which varies from device to device. The actuator used in this work is based on the oscillator design proposed by Arwatz et al. (2008) and is described in the following.

The geometric configuration enabling the self-sustained oscillations is rather simple and essentially two-dimensional. Figure 1 shows the internal flow field inside the device. An inlet nozzle supplies fluid into a chamber formed by two diverging walls which lead to two outlets. The outlets are separated by a splitter. Where the nozzle and the interaction chamber join, channels are connected to both sides of the nozzle. The area where the entrance channel splits into the two outlets and the channel exits merge is termed control port. The two control ports are connected by a feedback tube made of a flexible tube or a channel machined using (for example) additive manufacturing. The continuous inlet jet attaches due to the Coanda effect to one of two diverging walls downstream of the inlet. In the course of the operation of the device, the jet switches between the attachment walls and subsequent outlets, emitting alternating pulses through the outlets. The relevant geometry in the diverter stage is 2.5-dimensional, i.e. it is symmetrical to the two-dimensional plane with the same distance to the floor and ceiling of the device. The last stage is the outlet nozzle, with the nozzle comprising two outlets. The outlet openings would be connected to the surface to be controlled, with the actuator mounted below that surface. The oscillation frequency, i.e. the frequency with which the jet switches between the outlets, increases with the flow rate and is inversely proportional to the length and width of the feedback tube. Thus, the achievable frequency in dependence of the flow rate can be easily adapted by adjusting the feedback tube parameters to investigate and provide optimal parameters.

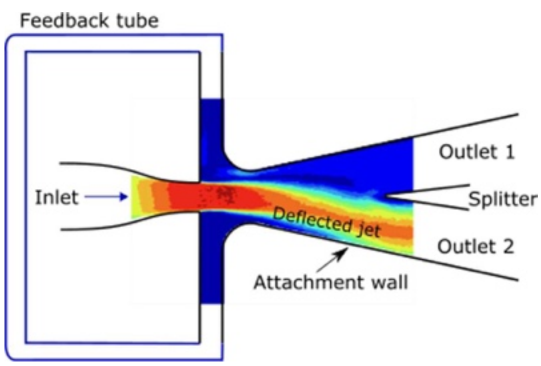

Figure 1. Schematic geometry and phase-averaged velocity magnitude of the internal flow field of the fluidic oscillator employed in this study at a phase angle of 0° at a flow rate of 15 l/min and an oscillation frequency of 2 Hz. The width of the inlet nozzle is 5 mm. Velocity field measured in bench-top experiments by the authors.

Several dimensionless quantities have been defined in the literature to characterize and quantify an actuation system. The most important are, without particular order, the momentum coefficient, the reduced frequency and the velocity ratio. The momentum coefficient C_μ is defined as the ratio of the momentum of the actuation jet and the freestream (Greenblatt and Wygnanski 2000). For incompressible conditions, it is

$$C_\mu = \frac{u_{jet}^2 l_s}{0.5 u_\infty^2 C}. \tag{2}$$

In this equation, u_{jet} is the excitation jet velocity, l_s is the streamwise length of the actuation slot, u_∞ is the freestream velocity and C is the airfoil chord length. The reduced frequency is defined in analogy to the Strouhal number,

$$F^+ = f\frac{u_\infty}{C}, \tag{3}$$

where f is the excitation frequency. It can be interpreted as the number of coherent flow structures above the foil. Optimal F^+ are of order of unity, but slightly different results have been reported for different applications. In general, a broad range of F^+ is expected to be effective (Greenblatt and Wygnanski 2000).

For assessing the efficiency of an actuation system, several figures of merit have been proposed by Seifert (2014). The Aerodynamic Figure of Merit (AFM) is defined as

$$AFM = \frac{F_L u_\infty/(F_D u_\infty + P_{hyd})}{F_{L,0}/F_{D,0}} \tag{4}$$

where u_∞ is the freestream velocity; F_L is the lift force; F_D is the drag force; and $F_{L,0}$ and $F_{D,0}$ refer to the baseline values of the lift and drag force, respectively. The hydraulic power can be calculated by

$$P_{hyd} = \dot{V}\Delta p \tag{5}$$

where $\dot{V}$ is the volume flow rate of the actuation system and Δp is the inlet pressure to the actuation system. The AFM can be used to assess the net energy efficiency of the actuation system. AFM greater than unity indicate a power saving by operating the actuation system. Additionally, the hydraulic power of the system can be compared to the freestream power by computing the power coefficient (Seifert et al. 1998)

$$C_E = \frac{P_{hyd}}{0.5\rho S u_\infty^3}, \tag{6}$$

where S is the planview area of the foil and ρ is the fluid density.

The effect of a given actuation intensity is dependent on the freestream velocity (as follows from Equation 2) and on the Reynolds number,

$$Re = \frac{u_\infty C}{\nu}, \tag{7}$$

where C is the chord length of the rudder or foil in general, ν is the kinematic viscosity and u_∞ is again the freestream velocity.

3. Small scale rudder model and actuation system

The rudder foil geometry used in this study is based on a proprietary design by Damen Marine Components, which closely resembles a NACA 0024. The small scale model has a chord length of 0.291 m and a span of 0.42 m, resulting in an aspect ratio of 1.44. The small-scale model upper edge is flat, and the lower edge is slightly rounded to reduce end effects. Pulsed jets, driven by a fluidic oscillator, are chosen as the method for the flow excitation. For experimental simplicity, the system is installed only on one side of the model, i.e. on the suction side considering the towing direction. The system consists of two independent chambers inside the leading edge of the rudder model. A single fluidic oscillator is used to supply all slots in both chambers with fluid, with each chamber connected to one outlet of the oscillator. The oscillator is positioned outside of the rudder model, for simplicity. Each chamber has 6 outlet slots to the rudder surface. Each slot has a rectangular cross-section and is 0.9mm wide and 19mm long. The slot outlet angle is 30° to the tangent of the rudder surface. Along the span, every other slot is connected to the same chamber. In the chordwise direction, the slots are located at $x/c = 0.24$. The slots are evenly distributed along the span, covering 55% of the total span. Figure 2 shows a crosssection of the leading edge of the model, showing the chambers and the connection to the outlet slots.

The rudder model and oscillator are manufactured using 3D printing from PETG and are post-processed with epoxy resin and coating. Connections between the oscillator and rudder model as well as to the supply pump are realized using flexible tubing and CAM-LOCK joints. Figure 3 shows the entire setup.

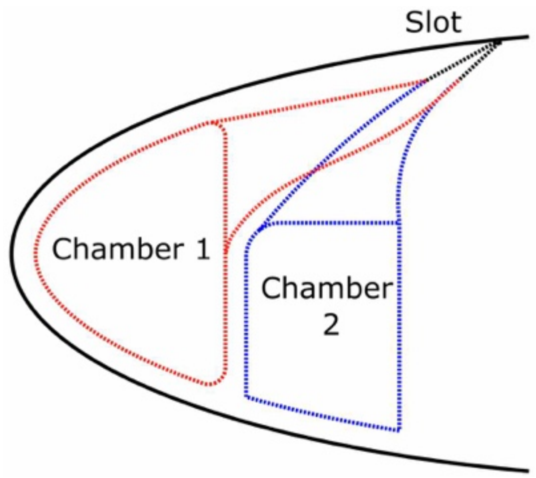

Figure 2. Cross-section of the leading edge of the rudder model with projected geometry details of the two chambers. Each chamber is connected to alternative exits of the oscillator.

Three different feedback tubes for the oscillator are investigated providing three different ranges between flow rate and frequency. It is anticipated that, in a real world system, the oscillator might be replaced by several oscillators and might be positioned inside the rudder model. If both sides of the model shall be actuated, a total of four chambers are necessary and at least two oscillators.

4. Small-scale towing tank experimental setup

The small-scale towing tank experiments are conducted at the towing tank at the University of Rostock. The tank is 37 m long, 5 m wide and has a water depth of 3 m. Three different setups are employed to acquire the characteristics of the actuation system.

In the first setup, the rudder model is mounted vertically and submerged well below the water surface in a quiescent environment. By aligning the light sheet of the Particle Image Velocimetry (PIV) system parallel to the rudder camber line, the flow induced by the actuation jets is measured. This allows for the quantification of the distribution, coherence, and impact of the actuation jets on the surrounding flow field.

In the second setup, the towed rudder model is mounted vertically just below the water surface, with the upper edge of the rudder aligning with the surface. The model is mounted to a high-fidelity force balance. This force balance consists of four three-component piezoelectric force transducers, precisely positioned between rigid plates made from aluminum, allowing for accurate force measurements in multiple

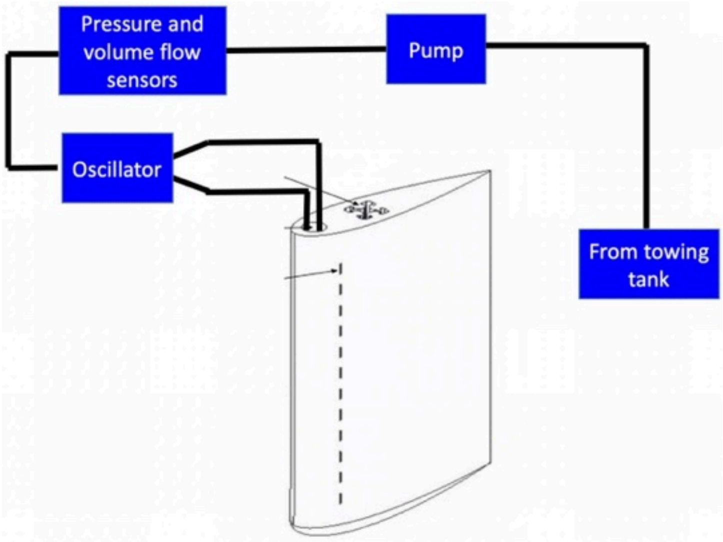

Figure 3. Actuation system periphery and sensor setup.

directions. The AoA can be changed by rotating the model relative to the force balance. During the experiment, the model is towed along the tank at constant velocity. The resulting lift and drag forces on the rudder model, influenced by the applied actuation, are measured using the force balance.

This configuration is used as well for the characterization of the actuation system. For this purpose, inlet flow rate, inlet pressure and forces are measured with the towing carriage at rest. The frequency of the oscillations is determined by computing the FFT of the forces which result from the jet switching, i.e. the thrust induced by the actuation system.

The third setup is used to acquire the 2D flow fields of streamwise slices on the suction side of the model using PIV. To achieve this, the model is mounted horizontally on a vertical strut, with the leading edge in streamwise direction, and then towed through the tank. It is submerged four times the model chord length, to eliminate possible surface effects. Thus, the flow fields of setups two and three are expected to be similar. In this configuration, the AoA is adjusted by pivoting the vertical strut. The light sheet is positioned at half of the span width and aligned with the centre of a blowing slot, such that the actuation jet emitted from the slot can be captured. The flow field is expected to be mostly two-dimensional at this position at half of the span of the model.

In each of the setups, a centrifugal pump with a maximum flow rate of 1000 liters per minute provides the supply flow to the actuation system. A simple bypass system is used to adjust the volume flow rate fed to the actuation system, allowing for fine-tuning of the actuation parameters. Industry-grade sensors measure the inlet pressure and supply flow rate with resolutions of 0.5 kPa and 0.1 l/min, respectively.

The towing experiments are conducted in independent runs. Each run consists of a single parameter configuration which is kept constant over the duration of the run. All small-scale experiments are conducted at a constant Reynolds number of 144,000 corresponding to a freestream velocity of 0.5 m/s, which leads to a measurement duration of about 40 s of steady state conditions. The choice of the Reynolds number for the small model is guided by technical aspects and the minimization of the influence of the free surface. The large scale model will validate these results at significantly higher Reynolds number (see Section 7).

4.1. Piezoelectric force balance

Four three-component piezoelectric force transducers manufactured by Kistler (Kistler Instrumente GmbH, Germany) are employed to measure the forces on the rudder model. These transducers are carefully positioned between rigid aluminum plates with a thickness of 35 mm. The bottom plate is connected to the towing car, while the top plate holds a L-shaped beam where the model is fixated. In this configuration, forces can be measured with an error of less than 1 % for loads above 1 N, with a maximum load of 5 kN in each direction. The force transducers are connected to a charge amplifier module, which is connected to an Analog-to-Digital conversion device (cRIO-chassis, National Instruments). For the presented measurements, the sampling rate is set to $f_s = 1638$ Hz, resulting in a Nyquist frequency of $f = 819$ Hz. The amplifier module incorporates a built-in analog high-pass filter which reduces the natural relaxation of the piezoelectric charges.

The acquisition routine is as follows: For each run, the data acquisition is started approximately 10 s before starting the carriage towing movement, and after reaching the end of the tank another additional 10 seconds are recorded. During post-processing, a peak detection routine identifies the start and end of the measurement from the derivative of the sum of the lift and drag forces, i.e. the acceleration acting on the model. To improve the reliability of the identification routine, the force signal is low-pass filtered using a standard third-order Butterworth filter applied forward and backward. The calculation of the lift and drag forces is done using the unfiltered data. With this procedure, linear drifts due to temperature effects and the offset of the amplification system can be assessed and corrected in a next step before calculating the time-averaged drag and lift coefficients.

When the actuation system is operated, the force measurement is zeroed with the actuation system operating but before starting the towing movement. Thus, all forces induced by the jets are zeroed out, and only forces related to the flow field are measured. This gives a conservative estimate of the system performance, since the thrust of the jets acts, depending on the AoA, mainly in streamwise direction and thus further reduces the overall drag force.

In all configurations, it is verified that the inlet pressure and flow rate do not change after the towing movement is started, to assure the actuation system operation is not dependent on the changing pressure distribution on the foil surface.

4.2. Underwater PIV

A state-of-the-art commercial PIV system manufactured by LaVision (LaVision GmbH, Germany) is used to measure the velocity field around the rudder model. The system is operated in 2D-2C mode, capturing the two-dimensional velocity field on a defined plane, by recording pairs of consecutive images of tracer particles carried by the fluid flow. The system incorporates a submerged torpedo-like structure housing the cameras, while a separate vertical tube holds the laser beam optics. The laser source used is a Nd:YAG EverGreen 200 laser, emitting at a wavelength of 532 nm with a maximum pulse energy of 200 mJ. The camera utilized is an IMAGER SX 5M with a high-resolution 5 Megapixel sensor. The field of view is 304.6 x 342.1 mm^2. The entire system is mounted on the towing carriage. The laser head and peripherals are attached to the carriage and a mirror arrangement is used to direct the laser beam to the light sheet optics. To provide tracer particles, the tank water is seeded with Vestosint polyamide particles with 100 m diameter. The seeding density of the tank is manually monitored and adjusted between runs to maintain optimal particle concentration and mitigate the settling of particles.

Double frames are recorded at a rate of 12.95 Hz. The velocity of the flow is then calculated from the displacement of the particles between two images. The Δt between the image pairs is adjusted to the individual experiments. While the optical resolution of the camera is sufficient to capture the actuation jets, the high velocity gradient between jet and freestream makes the choice for an optimal Δt in the PIV double images difficult. The Δt is thus adjusted to the freestream velocity. Computation of the vector fields is done in the Davis software suite (LaVision GmbH). A standard multi-pass PIV algorithm is used with a final interrogation area size of 16 x 16 or 32 x 32 pixels, depending on the setup, and a constant overlap of 50% in both x and y direction. This equates to a final resolution of 0.98 mm by 0.98 mm and 1.97 mm by 1.97 mm, respectively. The subsequent data analysis is implemented in Python.

The acquisition routine for the towing experiments is similar to the one employed for the force measurements and the transient stages of each run are recorded as well. The steady state flow field is then extracted by computing the Proper Orthogonal Decomposition of the entire run. Of the resulting modes, the first one represents the shifting 'mean' of the flow. The temporal derivative of the coefficient of this mode is used to detect start and end of the movement with a peak detection routine. A fixed number of 456 consecutive snapshots is then extracted from the steady-state, fully-developed flow. For the actuation system characterization in setup 1, 4541 snapshots are collected in one measurement for a single flow rate of 20 l/min (Figures 4–8).

4.3. Proper orthogonal decomposition (POD)

The POD (Berkooz et al. 1993) is used in this paper to analyse the coherent flow structures above the rudder model and serves as a tool for identification of changes in the flow field, i.e. for identification of the start and end of a measurement from PIV data. The POD decomposes a dataset $\boldsymbol{D}(\vec{x}, t)$ of snapshots into a combination of time-dependent coefficients $a_i(t)$ and an orthonormal basis of spatial modes Φ such that the dataset may be reconstructed by the linear combination $\boldsymbol{D} = \sum_i a_i(t)\Phi_i$. Singular value decomposition is used for computing the modes and coefficients, where matrix $\boldsymbol{U}$ is decomposed into left- and right-hand eigenvectors and singular values: $\boldsymbol{U} = A\Sigma V^{\mathrm{T}}$. Then, the individual modes are the columns of the left-hand eigenvectors, $\phi_i = A_i^{\mathrm{T}}$, and the associated energy e_i of the i-th mode is the square of its singular value $e_i = \Sigma_i^2$. The coefficients are obtained by

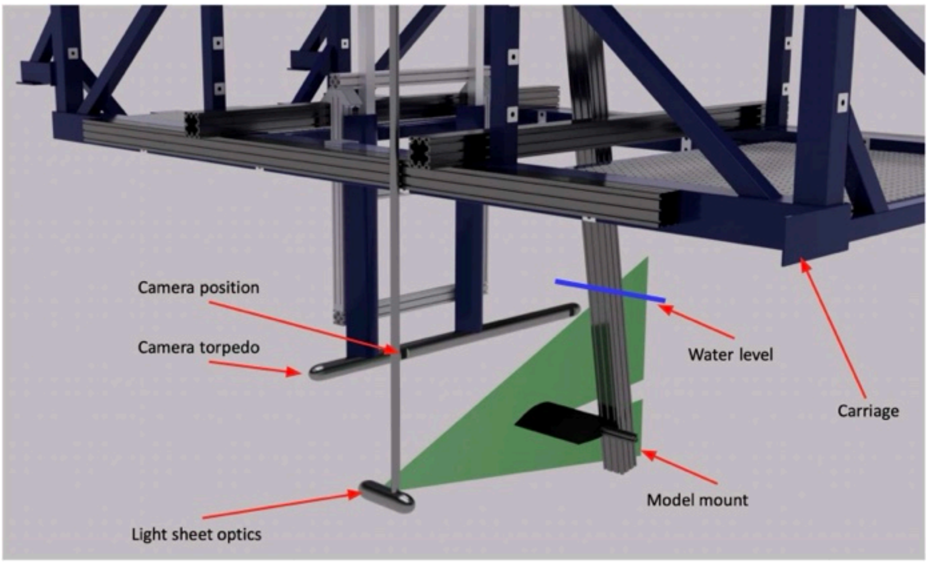

Figure 4. Small scale rudder model mounted horizontally on the towing tank carriage in the second PIV setup.

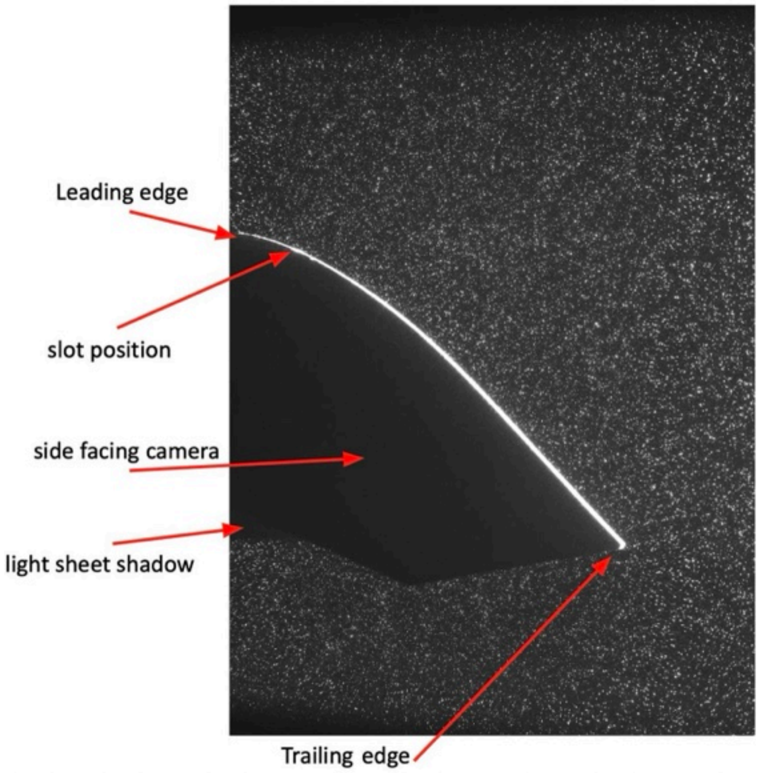

Figure 5. Raw PIV particle image of setup 2.

multiplication of the singular values with the right-hand eigenvectors, $a_i = \Sigma_i V_i$.

5. Actuation system characterization

The following section provides details of the characteristics of the actuation system. The flow rate through the system is measured against the inlet pressure. The frequency of the oscillation measured in setup 1 is linearly dependent on the inlet flow rate, in good approximation. The hydraulic power and C_μ increase cubic and quadratic, respectively, with the flow rate. For C_μ smaller than 2.5 %, the corresponding hydraulic power is almost negligible. To achieve a C_μ of 15 %,

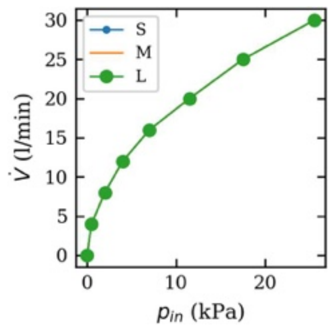

Figure 6. Inlet flow rate versus inlet pressure for the three different feedback tubes.

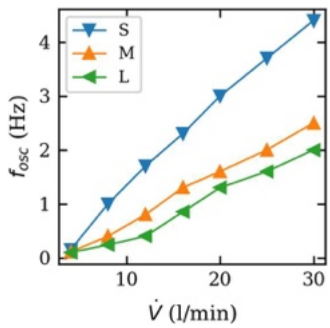

Figure 7. Oscillation frequency versus inlet flow rate for three different feedback tubes.

which is considered very high in the context of airfoil flow control, a modest 12.5 W of P_{hyd} is needed, giving a power coefficient C_E of 1.65.

The time-averaged flow field measured in setup 2 at a flow rate of 20 l/min is displayed in Figure 9. The streamwise and cross-stream velocity components clearly show the jets. Each jet entrains fluid from the sides towards the centre of the jet. A slight upwards directed trend is visible, most notably in the crossjet direction. This is attributed to the slight difference in temperature between the jet water and the tank water, since the jet water is heated the pump. Note that the cross-stream velocity is an order of magnitude smaller than the magnitude of the streamwise direction, and thus this effect is considered negligible

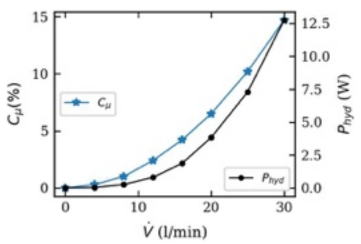

Figure 8. Momentum coefficient C_μ and hydraulic power of the actuation system calculated from input pressure and inlet flow rate.

with respect to the performance of the AFC system. The jets start interacting with each other approximately four slot widths downstream of the nozzles. Since the sampling frequency of the PIV is of the same order of magnitude as the oscillation frequency, no time-resolved information is available.

In order to gain insight into the dynamical process and the coherent structures of the jet switching, the POD is computed. The first two POD modes computed from this flow field presented in Figure 10 show the alternating operation of the adjacent AFC jet openings. Mode 1 represents the fully developed jet and mode 2 the jet switching. Every other slot is operated at the same time. The frequency spectra of the coefficients of these two modes are closely tied together, indicating they describe the same phenomena (see Figure 11). A smooth Lissajous figure is formed between the coefficients of mode 1 and 2, indicating that the jet switching is remarkably stable and undergoes only slight cycle-to-cycle variations (see Figure 12).

6. Small scale towing tank experimental results

The baseline lift and drag polars obtained for the rudder model are shown in Figure 13. The baseline was measured with the slots open and the slots taped, to assess the potential detrimental influence of the open slots on the flow. It is found that the open slots have a minor influence only. Particularly, they do not increase the drag at AoA=0°. For validation, the polars obtained using Xfoil are also shown in Figure 13. For the infinite foil, much higher C_L are expected. A correction for the aspect ratio can be achieved by scaling the data using $C_{L,corr} = C_L\lambda/(\lambda + 2)$, where λ is the aspect ratio, $\lambda = l/c$. When this is applied to the Xfoil data, the slopes of the curves agree with each other. The separation angle is determined to be 26° for the baseline flow with a maximum C_L of 0.85, followed by a relatively sharp decline of C_L.

A total of 63 runs investigating the influence of the C_μ are presented in Figures 14 and 15. The coefficient of lift before the separation angle ($\alpha_s = 25°$) remains unchanged for C_μ smaller than 1%, and the delay of separation by a maximum of 2° can be obtained, accompanied by an increase in $C_{L,max}$ and a reduction of C_D as long as the separation is delayed, at the expense of an increased drag at post-stall. Note that the post-stall C_L for these C_μ remains 20% higher than the baseline C_L. As C_μ is increased beyond 2 %, the C_L of the linear region of the polar is increased. The separation is delayed further, and a strong increase in $C_{L,max}$ up to $C_L = 1.22$ at 14.7% C_μ is achieved. The pre-stall lift increment comes with increased drag in the linear region as well as in post-stall. However, there remains a range of angles for

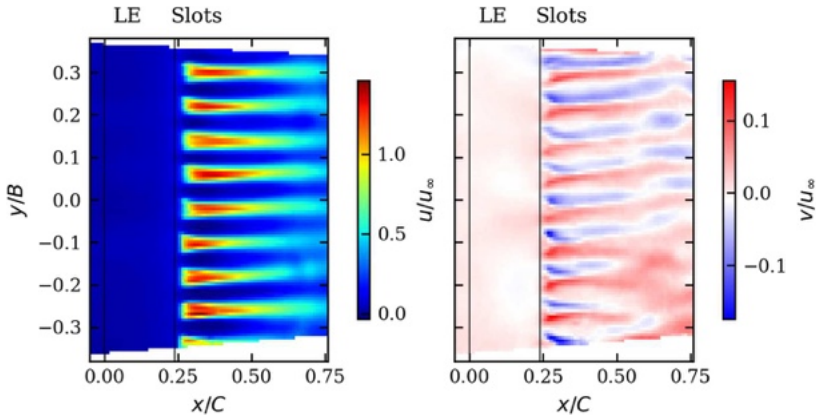

Figure 9. Mean velocity on the tangent plane above the rudder surface in streamwise (left) and cross-stream (right) direction measured by PIV in the vertical setup at a flow rate of 20 l/min with feedback tube L. The black lines mark the leading edge and the position of the slots.

every C_μ where the drag is always reduced compared to the baseline at increased lift conditions. This comparison is presented in Figure 16, where the delta C_L is displayed for the corresponding C_μ for the individual AoAs.

In the following, the corresponding flow fields for the parameters presented above are discussed. PIV measurements are available for AoA's of 25°, 27°, 28° and 30°. Figure 17 shows the baseline flow fields for all investigated AoA. At $\alpha_{CL,max}$, 25°, the flow fields exhibit a small separation bubble at the trailing edge. At 28°, where the lift is reduced by 19% compared to $C_{L,max}$, the separation bubble covers the last 30% of the chord. The separation increases to almost 50% of the chord at 30°, where the lift dropped to 63% of $C_{L,max}$. Note that the flow remains attached and the boundary layer remains intact on the first 20% of the chord for all the investigated AoA.

The AoA of 28° is chosen in the following to discuss the effect of the actuation (see Figure 18). The baseline flow (C_μ=0) shows a large separation bubble and a large area of decelerated flow above the rudder's suction side, starting almost from the leading edge. As the actuation is applied with increasing actuation intensity, the separation bubble decreases in size and length until it completely vanishes at C_μ= 4.2%. At the same time, the actuation jet starts to be visible as a high-velocity streak above the surface at C_μ=2.4% At high C_μ, above 6.5%, the high momentum leads to an extension of the jet flow beyond the trailing edge.

This observation can be further refined by investigating the boundary layer on the suction side of the foil. Figure 19 shows the velocity profiles of the boundary layer extracted from the time-averaged flow field measured by PIV, for an AoA of 28°. An individual line is drawn for each variation in C_μ.

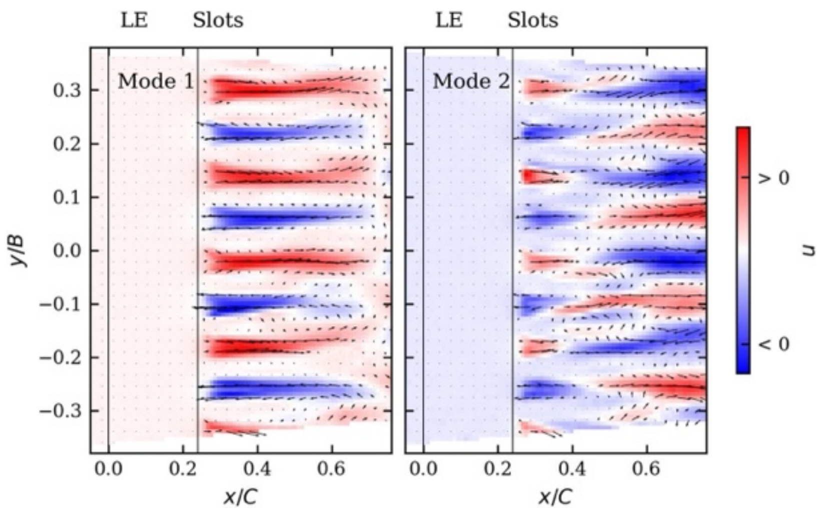

Figure 10. POD modes 1 and 2 of the flow field on the tangent plane above the rudder surface measured by PIV in the vertical setup at a flow rate of 20 l/min with feedback tube L. The black lines mark the leading edge and the position of the slots.

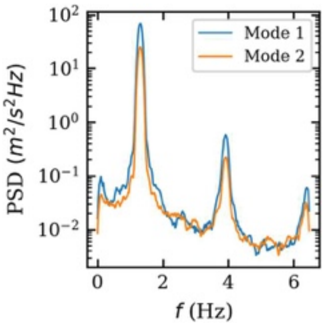

Figure 11. Power Spectral Density estimated using Welch's method of the coefficients of POD modes 1 and 2.

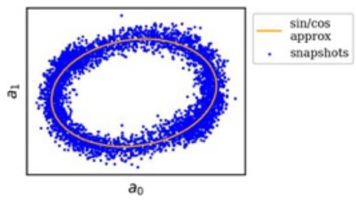

Figure 12. Lissajous figure of the coefficients of POD modes 1 and 2.

Upstream of the slot, the profiles remain unchanged independent of C_μ. The baseline boundary layer can be observed to decelerate and to increase in thickness along the surface. Downstream of the excitation location at x/c=24%, the jet can be clearly seen to increase the velocity at the wall. The mean velocity is increased exceeding the freestream velocity for C_μ equal to 4.2% and greater. At the trailing edge, the baseline profile is heavily decelerated and a recirculation region can be identified. The actuation is able to restore and significantly thin the boundary layer above the trailing third of the foil, and for the two highest C_μ investigated, the wall jet keeps a magnitude above the freestream velocity even at the trailing edge.

More insight to this aspect can be gained by analysing the Power Spectral Density (PSD) of the velocity magnitude close to the surface as shown in Figure 20. The baseline flow exhibits a peak at a Strouhal number of 0.5. However, for C_μ between 0.3% and 2.4%, power is contained at the baseline frequency as well as at much lower frequencies corresponding to a Strouhal number smaller than 0.3. For C_μ larger than 4.2%, the flow is dominated by the actuation frequency.

Figure 21 shows the influence of the actuation of the wake of the rudder model at an AoA of 27°. The baseline flow and for $C_\mu < 1\%$, the velocity field is dominated by the separation bubble and decelerated flow behind the trailing edge. With increasing C_μ, the separation bubble is gradually closed and the velocity in the wake approaches the freestream velocity.

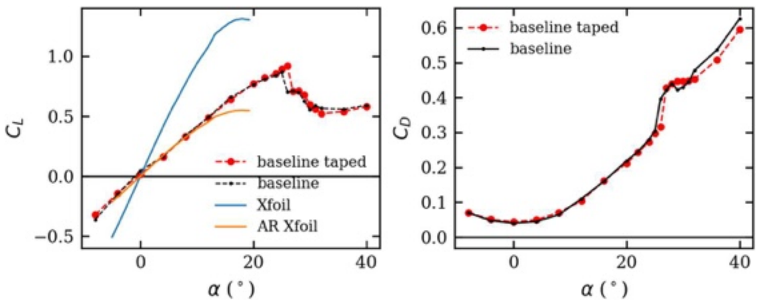

Figure 13. Lift and drag coefficients of the rudder model without actuation versus AoA with the slots open (baseline) and the slots covered with tape (baseline taped). For comparison, polars obtained using Xfoil for the infinite two-dimensional and aspect-ratio corrected foil are shown. AR=1.44, $Re = 144,000$.

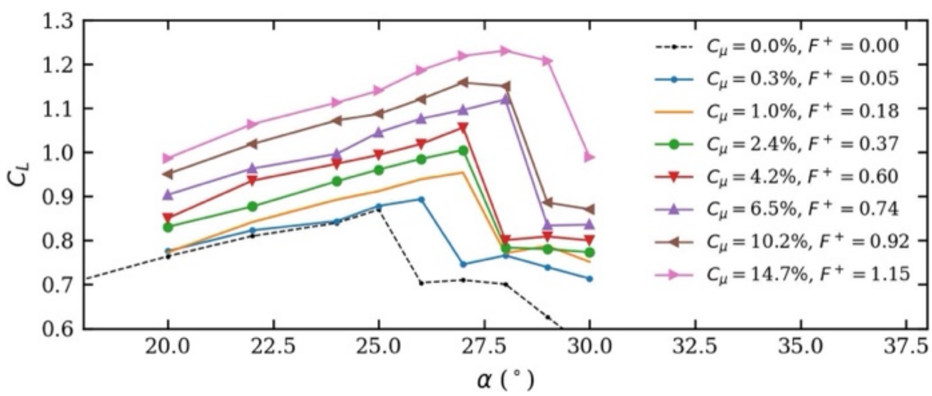

Figure 14. Lift coefficients versus AoA for various C_μ near the stall AoA.

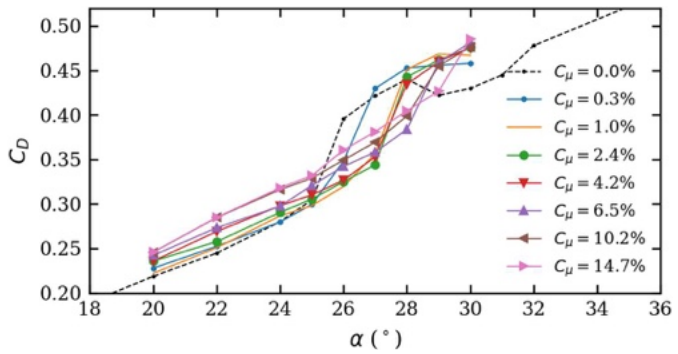

Figure 15. Drag coefficients versus AoA for various C_μ near the stall AoA.

For large $C_\mu > 6.5\%$, the actuation jet extends clearly beyond the trailing edge and the velocity in the wake is higher than the freestream, associated with the virtual extension of the foil and super-circulation lift enhancement (Spence 1956).

Another important question is the transient behaviour of the flow when the actuation system is operated at fully separated flow. To investigate this aspect, a dedicated experiment using PIV is performed at an AoA of 27° and with an actuation intensity of C_μ = 6.5%. The towing run is started with the actuation system switched off. After 15 s of towing, when a stable flow state is expected to be developed, the supply pump is switched on and the actuation system starts operation. The onset of the pump flow is immediate, since it always operates at full power and the volume flow is only regulated with the bypass ratio which is adjusted before the experiment. The resulting flow fields measured by PIV are decomposed into the POD modes, where the same number of snapshots before and after operation of the pump is used. Note that care needs to be applied when analysing transient events using POD, as discussed in Siegel et al. (2008). If the number of transient snapshots is small compared to the ones of steady state, the POD analysis can be applied and used to further the understanding of the flow field.

Figure 22 shows the resulting 2D modes, where the colormap corresponds to the streamwise velocity u. The first mode consists of three areas. Directly above the foil, the flow is accelerated for positive values of the mode coefficient. The flow at the leading edge is accelerated as well (indicated

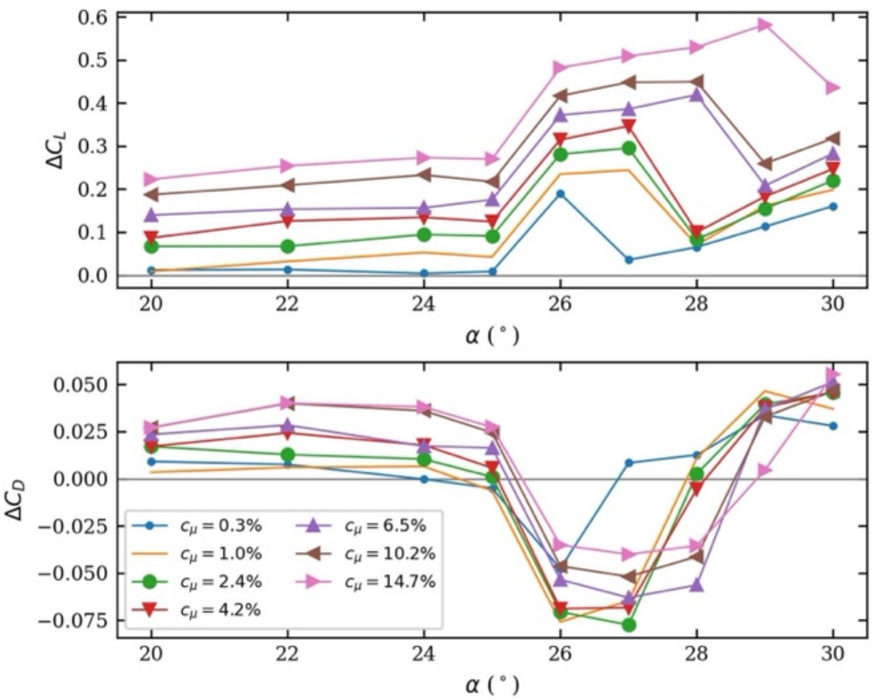

Figure 16. ΔC_L and ΔC_D for C_μ according to legend for various AoA.

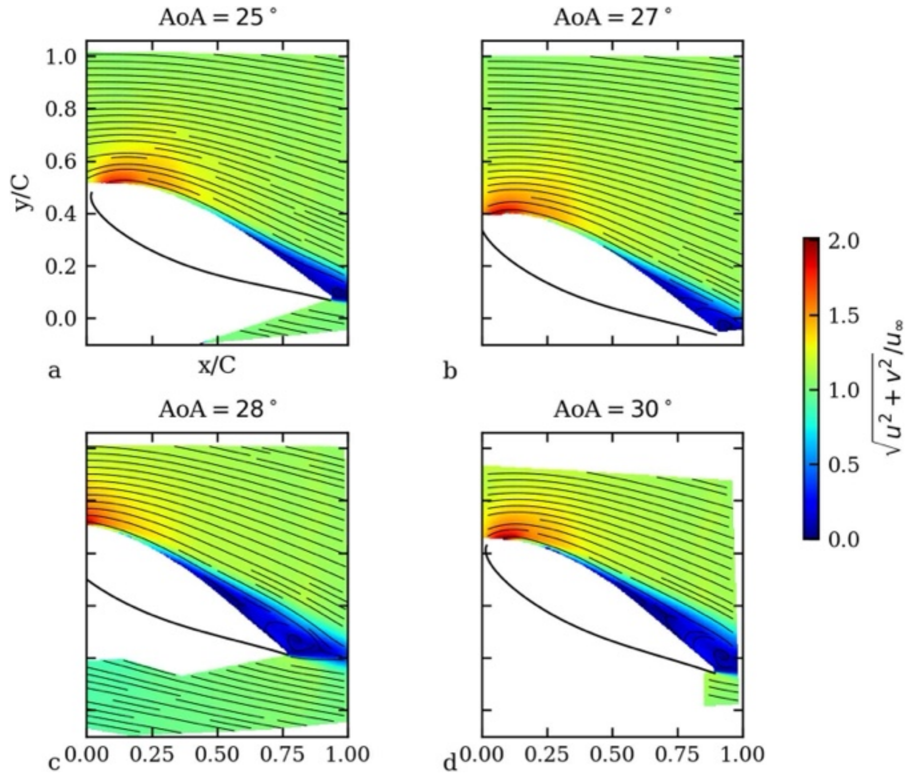

Figure 17. Temporal mean streamlines and velocity magnitude of the baseline flow fields (without actuation, open slots) for all the investigated AoAs measured by PIV.

by red area), whereas the flow at the rear of the foil loses velocity in the streamwise direction (indicated by blue area). The second and third modes together display the on and off switching of the actuation jet flow above the rudder. Two modes are necessary to approximate the pulsating jet flow, similarly as two Fourier modes are necessary to approximate a travelling wave.

Figure 23 displays the time history of the coefficients corresponding to the four modes discussed above. The time is non-dimensionalized with the chord length C and the freestream velocity u_∞, such that $t^* = tu_\infty/C$. The actuation system is activated at $t^* = 0$. The first mode is strongly negative before the system is operated, corresponding to decelerated and separated flow above the rudder suction side, as expected for the baseline flow. Modes two, three and four are close to zero before the system is operated. At $t^* = 0$, when the actuation is switched on, mode 1 abruptly transitions from negative to positive values, indicating the immediate acceleration of the flow above the rudder surface. This transition takes less than 1 second. Modes 2 and 3 immediately start with a sinusoidal oscillation, indicating that the jet starts its oscillation motion without delay. Note that mode 2 exhibits a strong peak in its signal at $t^* = 0$, associated with a stronger than average jet emitted from the slot when the system is switched on. This might be associated with a pressure pulse travelling through the tubing system when the pump is switched on for the first time, and this pulse presses fluid through the slot at high velocity. The origin of this pressure pulse can be related to the pump being switched on at full power, where the bypass system limits the volume flow through the actuation system but not the pressure. This effect might be beneficial in this special case for the reattachment of the flow, since a temporary higher C_μ is associated with this pulse.

In Figure 24, the dependence of ΔC_L on the actuation frequency is assessed for an AoA of 28°. In general, the frequency of the actuation had a minor influence on the achieved increase in lift, as all the investigated feedback tubes performed similarly. However, the comparison with the steady blowing shows clearly that some kind of unsteady actuation is necessary, as the steady blowing requires a much higher C_μ to reattach the flow and even decreases the C_L for small C_μ. This is expected, as previously shown by Seifert et al. (1996). Figure 25 shows the corresponding F^+ to the plot in Figure 24.

For all runs, the AFM (Equation 4) was calculated and selected results are shown in Figure 26. Highly efficient results were obtained, as a maximum AFM of 1.5 is reported at an AoA of 26° and many runs

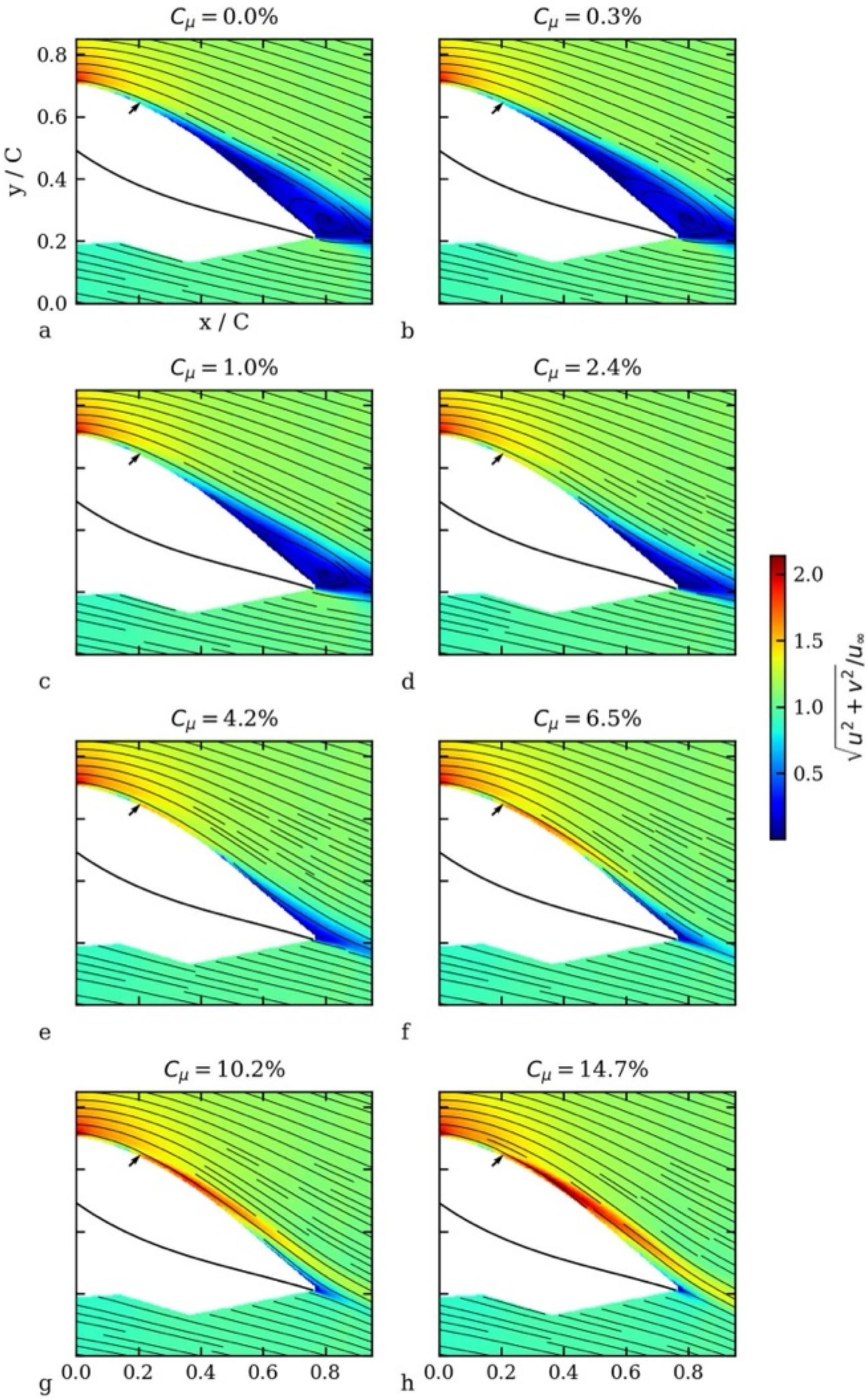

Figure 18. Magnitude and streamlines of the mean flow field around the rudder model measured by PIV for various C_μ at an AoA of 28°. The arrows mark the slot position.

exhibit AFM greater than unity. The best results are associated with a combination of small C_μ and one and two degrees post stall AoA's. The worst performing, from an energy perspective, are the cases with a small pre-stall AoA and high C_μ. However, an increase of maximum lift and resulting side force and maneuverability, achieved by circulation control, may be desirable even if the power required for this effect is high, considering the small duration AFC is needed.

7. Large scale towing tank experiments

The large-scale towing experiments are conducted at the towing tank facility of the Hamburg Ship Model Basin (HSVA). The rudder model cross-section

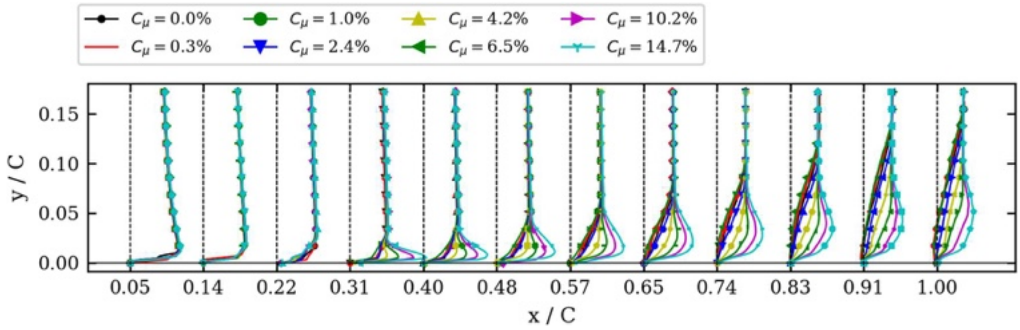

Figure 19. Profiles of the time-averaged tangential velocity along the foil surface measured by PIV for various C_μ at AoA of 28°.

geometry is the same as for the small-scale rudder. The span and chord of the large-scale model are 1.39 m and 0.97 m, respectively. Thus the aspect ratio of the model is 1.43, similar to the one of the small-scale model. In anticipation of the real-world application, the model is equipped with a head-box. This head-box is supposed to reduce the three-dimensionality of the flow at the upper end of the model, but increases the drag measured compared to a foil-only configuration. The head-box is fixed to an AoA of 0° and has the same cross-section geometry as the rudder foil. The rudder model is manufactured in two parts, where the trailing edge part is manufactured from wood and contains metal struts for stability. The leading edge part containing the actuation system is manufactured by additive manufacturing techniques. The actuation system design and setup are similar to the small-scale model, and the same fluidic oscillator and supply system are used. The number of spanwise slots is increased to 20, and the individual slot size is 30 mm in length and 1.1 mm in width. Their chordwise position is $x/c = 0.25$. As for the small scale model, only one side of the model is equipped with the actuation system. However, the large scale model has dummy slot openings also on the other side of the model for a realistic assessment.

For this system, the oscillation frequencies are obtained by measuring the pressure fluctuations inside the two chambers using a differential pressure sensor. The obtained frequencies are displayed in Table 1. The length of the feedback tube is 1.5 m for all cases.

In the current towing experiments, force measurements are conducted using a conventional strain gauge force balance. As for the smaller model, the input pressure and volume flow rate of

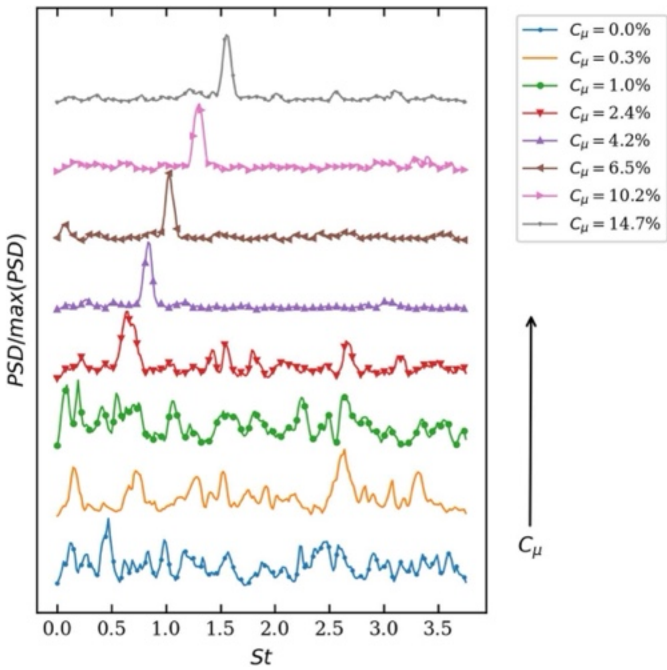

Figure 20. Normalized Power Spectral Density calculated using Welch's method of the flow magnitude at x/c=0.9 above the foil surface for various C_μ, extracted from PIV data at AoA of 28°. Every 10th data point marked.

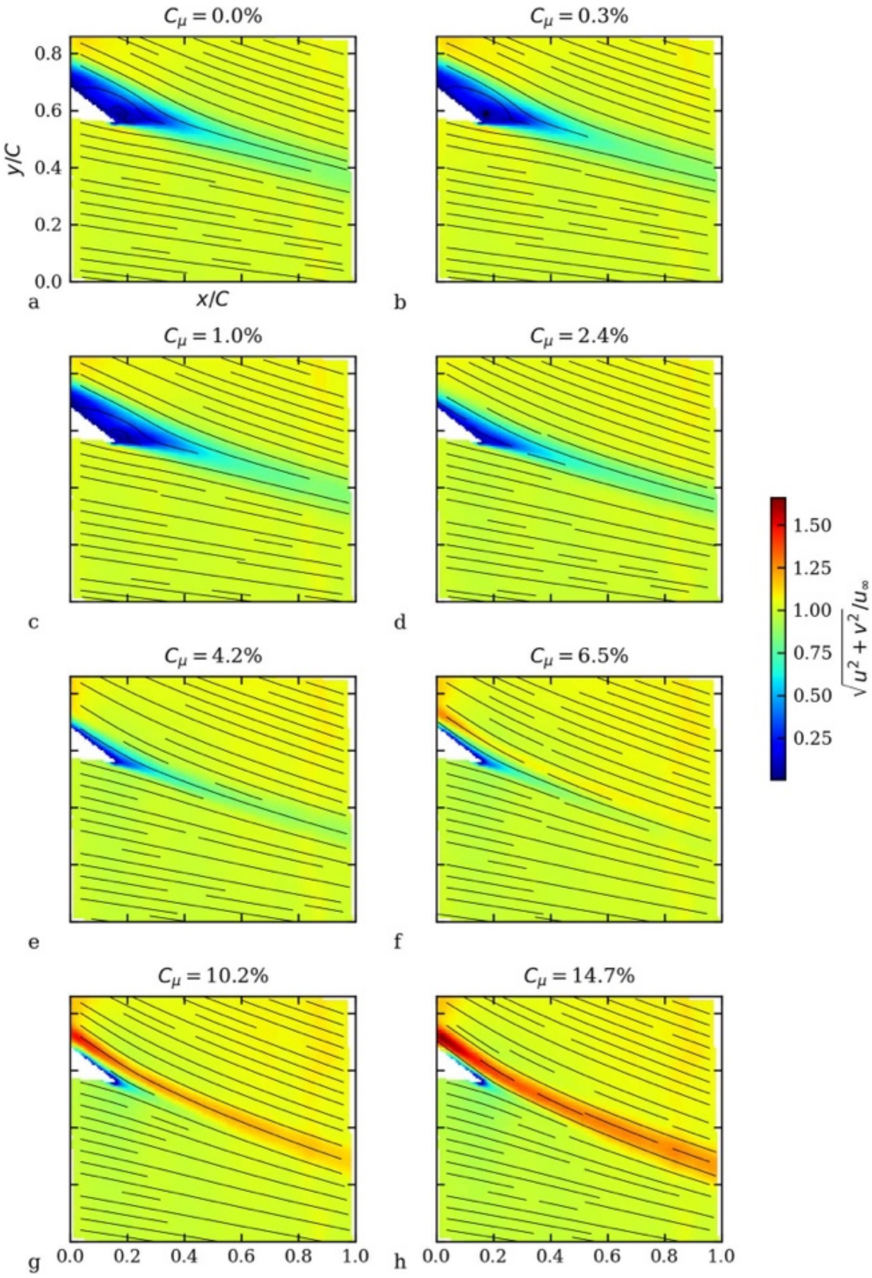

Figure 21. Temporal-mean velocity magnitude and streamlines of the wake flow at and behind the trailing edge of the rudder model for various actuation intensities, at an AoA of 27°.

the actuation system are measured. The model is towed at two different velocities corresponding to chord Reynolds numbers of $Re = 0.66 \times 10^6$ and 1.33×10^6. The orientation of the model is vertical as in setup 2 of the small scale model and the waterline is at half the height of the head-box. Similar to the small-scale model, constant velocity runs are conducted. Three different actuation intensities corresponding to a supply flow of 30, 60 and 90 l/min are investigated for a range of AoA's. A single actuation system volume flow rate translates now to different C_μ depending on the freestream velocity. Thus, for the smaller Re, a higher maximum C_μ can be obtained.

7.1. Results

The C_L and C_D curves and the stall behaviour of the unactuated flow are dependent on the Reynolds number (see Figure 27). At the lowest Reynolds number, $Re = 0.66 \times 10^6$, the C_L slope is linear for small AoA and the stall behaviour is very flat. At the higher

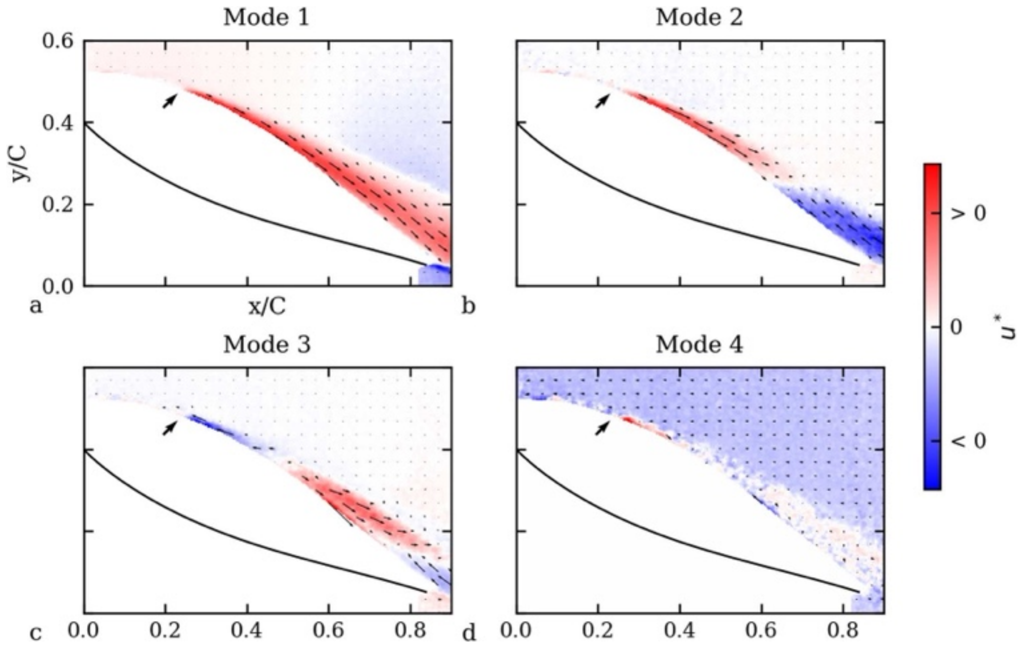

Figure 22. Most energetic POD modes of the transient flow experiment at an AoA of 27°. The arrows mark the slot position.

Re, $Re = 1.33 \times 10^6$, the C_L exhibits a more abrupt decrease when full separation occurs. Note that the maximum C_L at $Re = 1.33 \times 10^6$ is similar to the lower Reynolds number but the stall angle is decreased by four degrees. This may indicate a strong three-dimensional behaviour due to the free end on the lower side of the foil and the head-box on the upper side, which supports the flow attachment at the lower Reynolds number.

Figure 28 shows the results of static AoA runs. An increase in maximum C_L was obtained for $Re = 0.66 \times 10^6$ and $Re = 1.33 \times 10^6$ of up to 29% and 21%, respectively. The separation was delayed by up to 4 degrees.

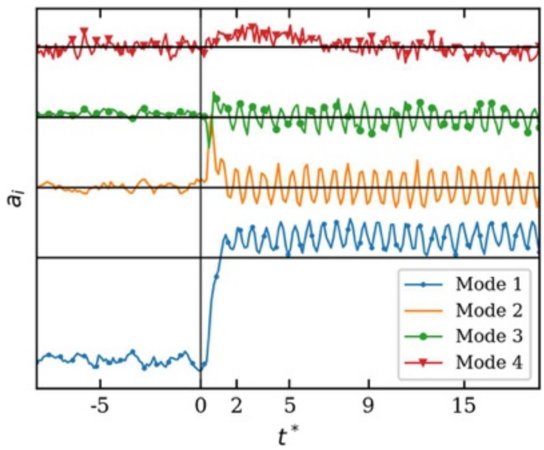

Figure 23. Coefficients of the first four POD modes of the transient flow experiment, shifted along the y axis for visual clarity. Horizontal lines indicate a value of zero of the respective coefficient. $t^* = 0$ indicates start of operation of the actuation system. $C_\mu = 6.5\%$, $Re = 144{,}000$, AoA$= 27°$.

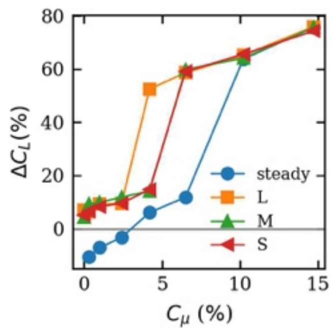

Figure 24. Dependence of ΔC_L on the actuation frequency for various C_μ at of AoA 28°, $Re = 144{,}000$. The letters correspond to the length of the feedback tube.

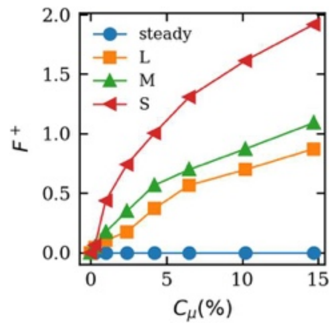

Figure 25. Reduced frequency for the different feedback tubes versus C_μ The letters correspond to the length of the feedback tube.

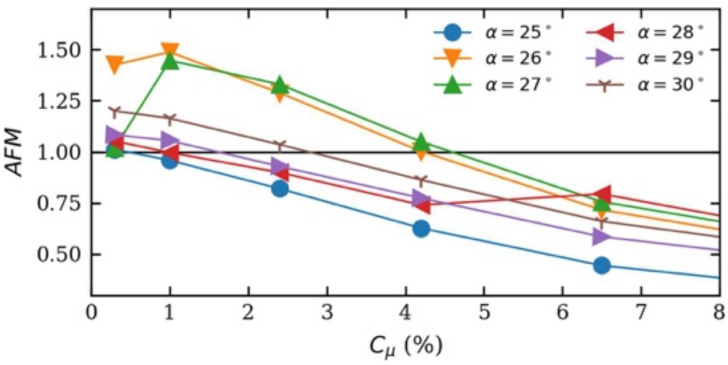

Figure 26. Efficiency Figure of Merit (see 4) indicating the performance of the actuation system for various AoA and C_μ at $Re =$ 144, 000.

Table 1. Frequencies of the large model actuation system versus the inlet volume flow rate.

Flow rate (l/min)	30	60	90
Switching frequency (Hz)	2.1	6.1	7.5

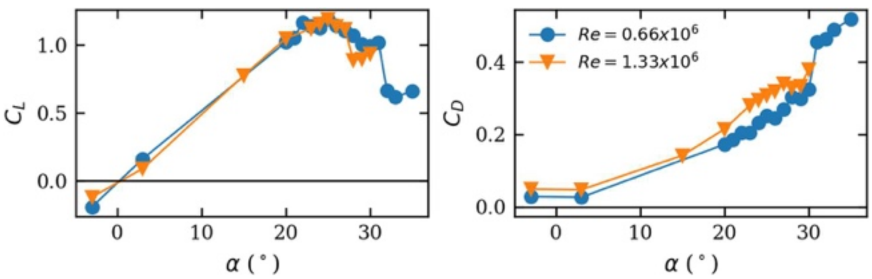

Figure 27. Baseline (C_μ=0.0) Lift and Drag coefficients of the large-scale rudder model for the two investigated Reynolds numbers. The legend applies to both plots.

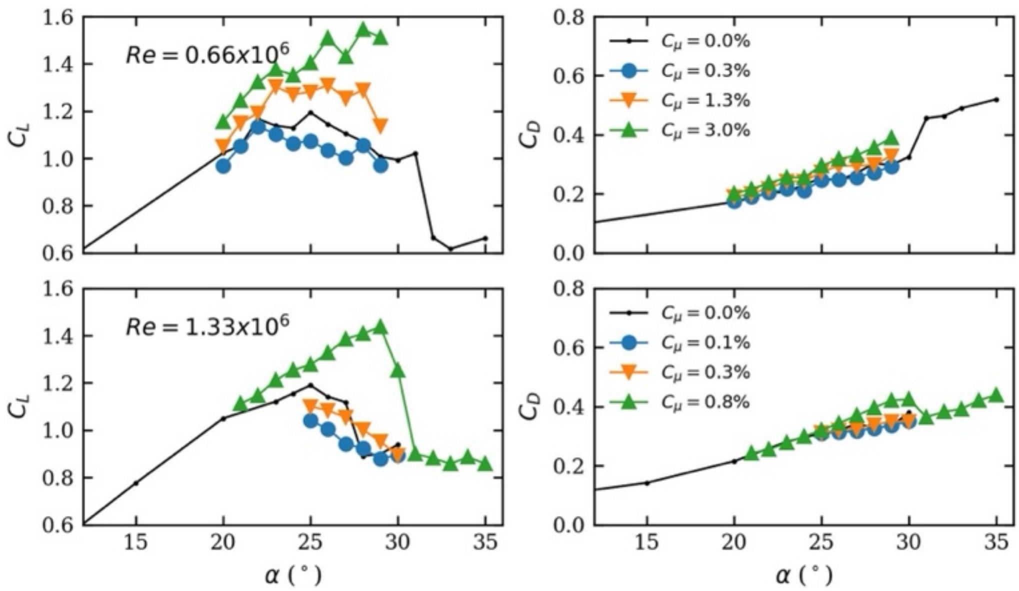

Figure 28. Lift and Drag coefficients of the large-scale rudder model for the two investigated Reynolds numbers at different momentum coefficients. The legend in the right plot applies to the left plot as well.

8. Conclusions

This paper showed the benefits of an application of AFC on two ship rudder models. Tests were conducted in towing tanks using load measurements and PIV. An increase of up to 80% of the baseline lift was achieved using moderate actuation energy levels. At the same time, flow separation was delayed by a few degrees. Technical and design aspects of the integration of such a system were solved on a model scale.

The presented experimental results demonstrated the feasibility of the approach up to near-full scale model size and chord-lenght Reynolds numbers at the order of 10^6. A future application of the system might aim for harbour maneuvering, i.e. at relatively low velocities and subsequently low Reynolds numbers, but high AoA and loads. The system presented here performed well under these conditions. In view of energy efficiency concerns, a benefit of the proposed system is that it only requires power when actually being operated, e.g. during harbour maneuvers. Depending of the operating profile of the vessel this may have an impact on the overall energy efficiency (e.g. ferries on short routes) or is negligible (long range routes). Thus, high amounts of C_μ can be realized without sacrificing the overall energy savings.

The results presented here exhibit a large potential for optimization, which may result in a further increase in the system efficiency. The chosen manufacturing strategy using fully 3D-printed parts has the drawback of high roughness of the walls inside the chambers, which cannot be post-processed. This increases the pressure loss of the overall system and the uniformity of the actuation. The precision of the printed slots in the sub-millimeter range has not been satisfying. The slot parameters, i.e. the width, length and chordwise position, have not been fully explored in this work and provide potential for further optimization.

Further work would be necessary to assess the effectiveness of the presented system when the rudder is positioned in the hull wake and the propeller slipstream. Various options exist to combine the current results with other high-lift or high-efficiency rudder types such as flapped rudders. For a flapped rudder, actuation can be employed at the leading edge of the main element and/or at the flap.

Acknowledgments

We express our thanks to Johannes Will for fruitful discussions on the particulars of rudder design.

Disclosure statement

No potential conflict of interest was reported by the author(s).

Funding

This project was supported by the German Federal Ministry of Economic Affairs and Climate Action [grant number 03SX496E].

ORCID

Matthias Fromm http://orcid.org/0000-0002-9757-2800

References

Ahn H-S, Kim H-C, Park J-J, Lee S-H. 1999. An application of coanda effect to a flapped rudder. J Ship Ocean Technol. 3(4):23–34.

Ahn H-S, Yoo J, Kim H. 2004. An advanced study on the development of marine lifting devices enhanced by the blowing techniques. J Ship Ocean Technol. 8(4):1–9.

Andino MY, Lin JC, Roman S, Graff EC, Gharib M, Whalen EA, Wygnanski IJ. 2019. Active flow control on vertical tail models. AIAA J. 57(8):3322–3338. doi: 10.2514/1.J057876

Andino MY, Lin JC, Washburn AE, Whalen EA, Graff EC, Wygnanski IJ. 2015. Flow separation control on a full-scale vertical tail model using sweeping jet actuators. In: 53rd AIAA Aerospace Sciences Meeting, Kissimmee, Florida, AIAA; p. 0785.

Arwatz G, Fono I, Seifert A. 2008. Suction and oscillatory blowing actuator. In: IUTAM Symposium on Flow Control and MEMS. Springer; p. 33–44.

Berkooz G, Holmes P, Lumley JL. 1993. The proper orthogonal decomposition in the analysis of turbulent flows. Annu Rev of Fluid Mech. 25(1):539–575. doi: 10.1146/fluid.1993.25.issue-1

Choi B-J, Kim H-C. 2004. An experimental evaluation of the coanda jet applied high efficient rudder system for vlcc. J Ship Ocean Technol. 8(2):1–12.

Gim O. 2017. On flow charactistics around special rudders by piv measurement; flapped and water-blowing rudder. J Korean Soc Mar Environ Saf. 23(2):200–207. doi: 10.7837/kosomes.

Greenblatt D, Wygnanski IJ. 2000. The control of flow separation by periodic excitation. Progress Aerosp Sci. 36 (7):487–545. doi: 10.1016/S0376-0421(00)00008-7

Lin JC, Andino MY, Alexander MG, Whalen EA, Spoor MA, Tran JT, Wygnanski IJ. 2016. An overview of active flow control enhanced vertical tail technology development. In: 54th AIAA Aerospace Sciences Meeting, San Diego, California, AIAA; p. 0056.

Liu J, Hekkenberg R. 2017. Sixty years of research on ship rudders: effects of design choices on rudder performance. Ships Offshore Struct. 12(4):495–512. doi: 10.1080/17445302.2016.1178205

Molland AF, Turnock SR (2011). Marine rudders and control surfaces: principles, data, design and applications. Elsevier.

Oh J-K, Ahn H-S, Kim H-C, Lee S-H, Lew J-M. 2003. Application of coanda effects to a ship hydrofoil. J Ship Ocean Technol. 7(2):29–39.

Schloesser P, Soudakov V, Bauer M, Wild J. 2019. Active separation control at the pylon-wing junction of a real-scale model. AIAA J. 57(1):132–141. doi: 10.2514/1.J057345

Scott Collis S, Joslin RD, Seifert A, Theofilis V. 2004. Issues in active flow control: theory, control, simulation, and experiment. Prog Aerosp Sci. 40(4-5):237–289. doi: 10.1016/j.paerosci.2004.06.001

Seele R, Graff E, Gharib M, Taubert L, Lin J, Wygnanski I. 2012. Improving rudder effectiveness with sweeping jet actuators. In: 6th AIAA Flow Control Conference, New Orleans, Louisiana, AIAA; p. 3244.

Seifert A. 2014. Evaluation criteria and performance comparison of actuators for bluff-body flow control. In: 32nd AIAA Applied Aerodynamics Conference, Atlanta, GA, AIAA; p. 2400.

Seifert A, Bachar T, Koss D, Shepshelovich M, Wygnanski I. 1993. Oscillatory blowing: a tool to delay boundary-layer separation. AIAA J. 31(11):2052–2060. doi: 10.2514/3.49121

Seifert A, Darabi A, Wyganski I. 1996. Delay of airfoil stall by periodic excitation. J Aircr. 33(4):691–698. doi: 10.2514/3.47003

Seifert A, Eliahu S, Greenblatt D, Wygnanski I. 1998. Use of piezoelectric actuators for airfoil separation control. AIAA J. 36(8):1535–1537. doi: 10.2514/2.549

Seifert A, Greenblatt D, Wygnanski IJ. 2004. Active separation control: an overview of reynolds and mach numbers effects. Aerosp Sci Technol. 8(7):569–582. doi: 10.1016/j.ast.2004.06.007

Seifert A, Stalnov O, Sperber D, Arwatz G, Palei V, David S, Dayan I, Fono I. 2009. Large trucks drag reduction using active flow control. In: The Aerodynamics of Heavy Vehicles II: Trucks, Buses, and Trains. Springer; p. 115–133.

Seo D-W, Oh J, Jang J. 2017. Performance analysis of a horn-type rudder implementing the coanda effect. Int J Nav Archit Ocean Eng. 9(2):177–184. doi: 10.1016/j.ijnaoe.2016.09.003

Siegel SG, Seidel J, Fagley C, Luchtenburg DM, Cohen K, McLaughlin T. 2008. Low-dimensional modelling of a transient cylinder wake using double proper orthogonal decomposition. J Fluid Mech. 610:1–42. doi: 10.1017/S0022112008002115

Spence DA. 1956. The lift coefficient of a thin, jet-flapped wing. Proc R Soc Lond Ser A Math Phys Sci. 238 (1212):46–68.

Spyropoulos CE. 1964. Sonic oscillator. In: Procc. of the Fluid Amplification Symposium, Washington, DC, Army Materiel Command; p. 27–52.

Warren RW. 1962. Fluid oscillator, Jan 9, 1962. US Patent 3,016,066.

Whalen EA, Spoor M, Vijgen PM, Tran J, Shmilovich A, Lin JC, Andino M. 2016. Full-scale flight demonstration of an active flow control enhanced vertical tail. In: 8th AIAA Flow Control Conference, Washington, DC, AIAA; p. 3927.

Zelazny K. 2014. Approximate method of calculating forces on rudder during ship sailing on a shipping route. TransNav,Int J Marine Navigation Safe Sea Transport. 8 (3):459–464. doi: 10.12716/1001ISSN 2083-6473.

3.4 Comparison of Methods

The three papers in this thesis employ a variety of methods in a carefully chosen combination of high-fidelity analytical and experimental methods to explore the application of AFC in marine environments using fluidic oscillators.

The first paper primarily analyzes existing, high-fidelity CFD data to investigate the internal flow dynamics of fluidic oscillators. It utilizes Proper Orthogonal Decomposition (POD) and Lagrangian Coherent Structures (LCS) analysis to identify the dominant modes influencing jet deflection. Thus, a data-driven approach brings the direct correlation between pressure differences across control ports and the resulting jet behavior into focus, providing a foundation for designing experiments with water-based oscillators.

Complimentary, the second paper focuses on experimental methods to obtain data and uses similar analytical methods to validate the insights gained from the CFD data analysis and to explore the oscillation mechanisms in a water-based oscillator. An experimental setup was designed with optical access for Particle Image Velocimetry (PIV) and Laser Doppler Anemometry (LDA), along with pressure taps on the control ports. These experiments allowed for direct observation and measurement of the fluid fields and properties within the oscillator, revealing that the pressure and feedback tube flow waveforms closely resembled the variables of the FitzHugh-Nagumo system. Mathematical methods are employed for parameter finding in the equation system and analysis and simulation of the resulting dynamical system. This experimental validation was crucial for enhancing the understanding of the oscillator's operation and for refining its design, and revealed the complex physical relationship between pressure and feedback tube flow.

The third paper again combines both experimental and data-driven methods to apply the optimized oscillator design to a ship rudder model and assess its impact on flow separation and rudder performance. Extensive towing tank experiments were conducted in two different facilities at the University of Rostock and the Hamburg Ship Model Basin (HSVA), involving force measurements and underwater PIV to capture the flow field around the rudder. POD was used to interpret the experimental data and quantify the effects of AFC on flow dynamics. These experiments demonstrated the practical effectiveness of the AFC system in delaying flow separation and enhancing rudder performance.

By applying advanced analytical and experimental methods, the three papers collectively provide a comprehensive framework for understanding and optimizing fluidic oscillators for airborne as well as marine AFC applications.

3.5 Conclusion of the Publications

Together, the three papers presented in this thesis collectively advance the understanding and application of fluidic oscillators and AFC in both aerodynamic and hydrodynamic contexts, presenting a cohesive narrative that bridges fundamental fluid dynamics research with practical engineering applications. They highlight the critical role of fluidic oscillators in advancing AFC technologies and their potential to improve performance in both aerodynamics and hydrodynamics. Future research could further explore the integration of these systems into full-scale operational environments, optimizing their designs for specific applications, and investigating their long-term impacts on fuel efficiency and emissions reduction.

Several important advancements and achievements in the field of fluid dynamics and AFC are presented in the papers. Notably, the studies represent the first time a fluidic oscillator has been applied to a ship rudder, both in model and near-full-scale experiments. This innovative application demonstrates the feasibility and effectiveness of AFC in the maritime sector, showcasing significant improvements in rudder performance and maneuverability.

Another pioneering achievement is the novel relation established between the FitzHugh-Nagumo system and fluidic oscillators, providing a new theoretical framework to understand the dynamics of these devices.

Additionally, the research presents the first-time visualization of flow fields and Lagrangian Coherent Structures fields for this type of oscillator, offering detailed insights into the underlying fluid mechanics. These visualizations, achieved through advanced techniques like LES and POD, reveal the intricate jet switching mechanisms and the impact of pressure differences on flow behavior.

Furthermore, the comprehensive experimental setups, including PIV and force measurements, validate the effectiveness of AFC systems in delaying flow separation and enhancing lift forces. Collectively, these studies mark significant advancements in the understanding and application of fluidic oscillators and AFC, paving the way for future innovations in both aerodynamics and hydrodynamics.

Applying AFC to ship rudders holds significant potential benefits for the maritime industry. AFC can markedly delay flow separation, which occurs at high rudder deflection angles, thereby enhancing the rudder's lift force and overall steering performance. This improvement translates to a narrower turning radius and increased maneuverability, which is crucial during critical operations like harbor maneuvers. By maintaining attached flow over the rudder at higher angles of attack, AFC can also reduce hydrodynamic drag, leading to more efficient vessel operation and lower fuel consumption. Furthermore, AFC allows for the possibility of designing smaller rudders that achieve the same or better performance as larger ones, thereby reducing construction costs and further, significantly decreasing drag under normal operating conditions. The resultant reduction in fuel usage not only offers economic savings but also contributes to lower greenhouse gas emissions, supporting environmental sustainability in the shipping industry. Overall, the integration of AFC systems in ship rudders could advance maritime control surfaces, providing both performance enhancements and ecological benefits.

3.6 Associated publications

The results of the discussed research have also been presented at:

Fromm, M., Bestier, T., & Grundmann, S. (2022). *Erhöhung der maximalen Auftriebskräfte am Schiffsruder durch aktive Strömungskontrolle.* Presented at the Fachtagung **Experimentelle Strömungsmechanik**, Ilmenau, 6.–8. September 2022. ISBN 978-3-9816764-8-8.

Specifically, the research presented in the second publication directly led to the granting of the associated patent:

Fromm, M., Bestier, T., & Grundmann, S. O. (2024). *Vorrichtung und Verfahren zur Erhöhung einer Auftriebskraft an einem Schiffsruder mittels aktiver Strömungskontrolle, sowie Schiffsruder.* German Patent **DE102023100314B4**, Deutsches Patent- und Markenamt.

4 Extended Discussion

In this chapter, additional, previously unpublished experiments and analysis are presented, that underline the coherence of the above presented research and add further insights beyond the publications.

4.1 Chaos, Spiking and Absence of Oscillations

The FitzHugh-Nagumo system, a simplified version of the Hodgkin-Huxley model, is known for its ability to exhibit chaotic behavior under certain conditions. Chaos in the FHN system is characterized by aperiodic, unpredictable oscillations that arise due to the system's nonlinearity and sensitivity to initial conditions. This chaotic behavior is influenced by parameters such as the excitation frequency and the strength of the nonlinear feedback. When applied to the study of fluidic oscillators, the prediction of chaos in the FHN system provides valuable insights into the complex dynamics of fluidic oscillation.

Chaotic behavior was observed in the experiments with fluidic oscillators conducted over the course of this theses, which can occur due to factors such as poor manufacturing, low flow rates, and insufficient back pressure. Just as the FHN system can exhibit chaotic oscillations, fluidic oscillators may also experience aperiodic and unpredictable jet switching patterns, especially under conditions where nonlinear interactions dominate. These chaotic oscillations can compromise the effectiveness of active flow control by making the behavior of the fluidic oscillator difficult to predict and control. Understanding the potential for chaotic behavior in fluidic oscillators is crucial for optimizing their design and operation in active flow control applications, as it highlights the importance of precise parameter tuning to maintain stable and predictable oscillations. This analogy between the FHN system and fluidic oscillators underscores the relevance of mathematical models in predicting and managing the complex dynamics observed in fluidic systems.

The FitzHugh-Nagumo (FHN) system not only predicts chaotic behavior but also spiking behavior. Spiking in the FHN system is characterized by sudden, transient bursts of activity, followed by a return to a quiescent state. In our experiments, this spiking behavior manifested as the oscillator failing to maintain continuous oscillations, instead outputting fluid from only one side for extended periods. Occasionally, the flow would abruptly flip to the

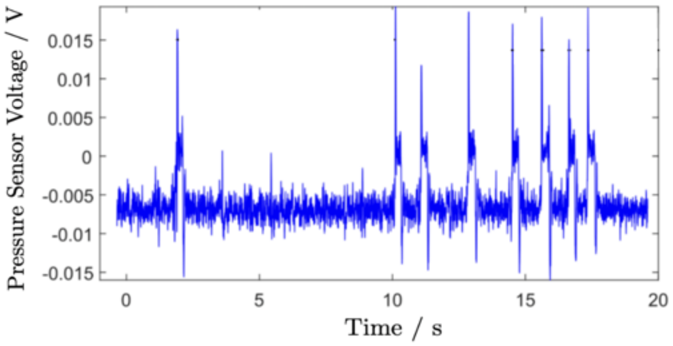

Figure 4.1: Measured voltage signal from a fluidic oscillator exhibiting spiking behavior. The signal shows periods of quiescence interrupted by sudden, transient bursts of activity, characteristic of spiking dynamics. The time intervals between spikes, Δt_{max} and Δt_{min}, indicate the variability in the occurrence of these spikes.

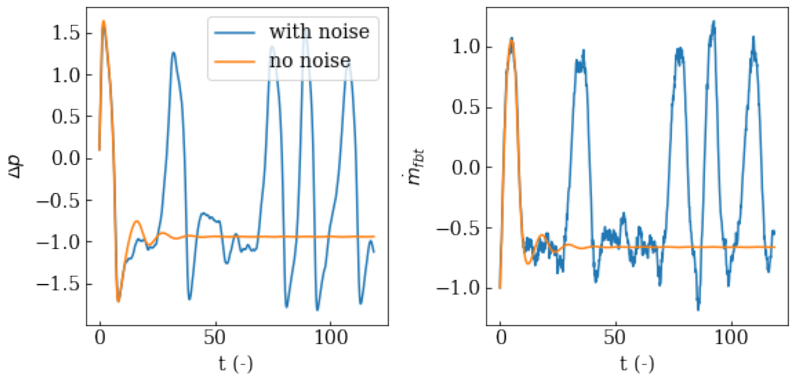

Figure 4.2: Simulated behavior of the FitzHugh-Nagumo (FHN) system. Pressure difference (Δp) across the control ports, and feedback tube flow ($\dot{m}_{fbt}$) over dimensionless time, with and without random noise.

other side for a short duration before reverting to the single-sided output. This behavior typically occurred in oscillators that were poorly manufactured, specifically those with excessively high flow resistance in the feedback tube, which dampens the oscillations and causes the device to operate in a single-sided manner. Additionally, high inlet flow turbulence, acting as input noise, can trigger these spikes, similar to how noise induces spiking in the simulated FHN system. Figure 4.1 shows measured spiking behavior, and parallels the spiking behavior predicted by the FitzHugh-Nagumo system when subjected to input noise. This behavior was observed under conditions of imperfect manufacturing, high flow resistance in the feedback tube, and high inlet flow turbulence.

Figure 4.2 showcases simulated spiking of the corresponding FHN system. The presence of noise leads to aperiodic, transient spikes in both Δp and feedback tube flow, similar to the spiking observed in experimental measurements. The simulation without noise and otherwise identical parameters converges into a steady state, single-sided output. This demonstrates the system's sensitivity to external disturbances and the impact of noise on the dynamics of the fluidic oscillator.

Understanding this spiking behavior is crucial for diagnosing and addressing manufacturing flaws and optimizing the operational parameters to ensure reliable oscillatory performance in active flow control applications.

4.2 Limit cycle behavior

The FitzHugh-Nagumo (FHN) system is well known for exhibiting limit cycle behavior, a type of stable, periodic oscillation that occurs when the system is perturbed from its equilibrium. In the context of fluidic oscillators, this limit cycle behavior is highly relevant for understanding how oscillations initiate and stabilize from a state of fluid rest. When a fluidic oscillator begins operation, it starts from a non-oscillatory state where the fluid is at rest or flowing steadily. As the system is activated, the feedback mechanisms within the oscillator, analogous to the nonlinear feedback in the FHN system, begin to influence the flow dynamics.

Initially, small perturbations in the flow can grow due to the system's inherent instability, leading to the development of oscillations. These oscillations gradually increase in amplitude and frequency until they reach a stable limit cycle. This transition from rest to stable oscillations is critical for the effective functioning of fluidic oscillators in active flow control applications. The time it takes to reach stable oscillations, as well as the characteristics of these oscillations, can significantly impact the performance of the AFC system.

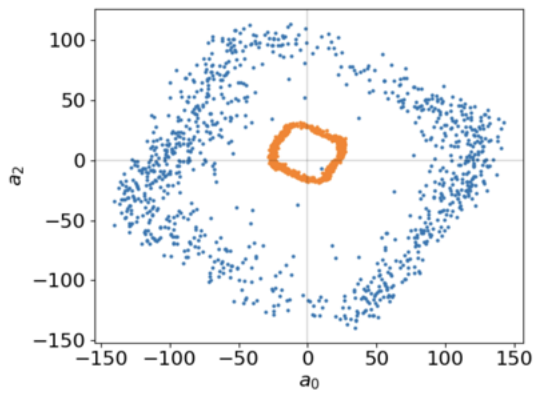

Figure 4.3: Dimensionless POD mode coefficients for two different flow rates.

In the experiments, the establishment of stable oscillations was observed to depend on several factors, including the initial flow rate and the design of the oscillator. Manufacturing imperfections, insufficient back pressure, or suboptimal flow rates could delay or disrupt the transition to stable limit cycle oscillations, leading to prolonged periods of unstable or chaotic behavior. Understanding the limit cycle behavior of the FHN system provides valuable insights into optimizing the startup phase of fluidic oscillators. By ensuring that the system parameters are within the appropriate ranges, it is possible to facilitate a smooth transition from fluid rest to stable oscillations, thereby enhancing the reliability and efficiency of AFC systems.

Thus, the limit cycle behavior of the FHN system serves as a useful model for predicting and managing the initial behavior of fluidic oscillators, ensuring that they achieve stable, predictable oscillations necessary for effective flow control.

4.3 POD modes and the FHN system

Proper Orthogonal Decomposition (POD) is a powerful tool for analyzing complex fluid flows by decomposing them into a set of orthogonal modes that represent the most energetic structures in the flow. In the context of fluidic oscillators, the relationship between POD modes and the FitzHugh-Nagumo (FHN) system provides a deeper understanding of the oscillatory behavior and the underlying dynamics.

The FHN system, with its nonlinear differential equations, models excitable systems and is capable of exhibiting both stable limit cycles and chaotic behavior. When applied to fluidic oscillators, the FHN system helps explain the nonlinear interactions and feedback mechanisms that drive oscillations. POD, on the other hand, offers a way to quantify and visualize these oscillations by breaking down the flow field into dominant modes.

In this study, the first few POD modes were found to capture the essential dynamics of the fluidic oscillator. The primary modes represent the fundamental oscillation pattern, corresponding to the jet switching mechanism driven by the pressure difference across the control ports. Subsequent modes captured secondary structures, such as the flow in the feedback tubes and higher harmonic components of the oscillation.

Relating these POD modes to the FHN system, the primary mode can be seen as analogous to the main variable of the FHN system that describes the excitable state of the system. This mode represents the core oscillatory behavior and the main feedback loop responsible for the jet deflection. Secondary POD modes, which capture additional flow structures and harmonics, correspond to the secondary variables in the FHN system that modulate the primary oscillation, introducing complexity and potential for chaotic behavior under certain conditions.

By linking POD modes with the FHN system, it is possible to interpret the fluidic oscillator's dynamics in terms of excitable system behavior. The primary mode's stability and periodicity reflect the stable limit cycle of the FHN system, while the presence and interaction of higher modes can indicate the onset of more complex, potentially chaotic dynamics. This relationship provides a framework for understanding how different flow structures contribute to the overall behavior of the fluidic oscillator, aiding in the design and optimization of AFC systems. Figure 4.3 showcases this idea where the phase space of the POD modes resembles the phase space of the FHN system variables.

In summary, the connection between POD modes and the FHN system enhances our understanding of the fluidic oscillator's behavior by combining a robust mathematical model of excitable dynamics with a powerful decomposition technique for fluid flow analysis. This integrated approach allows for more effective prediction, control, and optimization of oscillatory flow systems in active flow control applications.

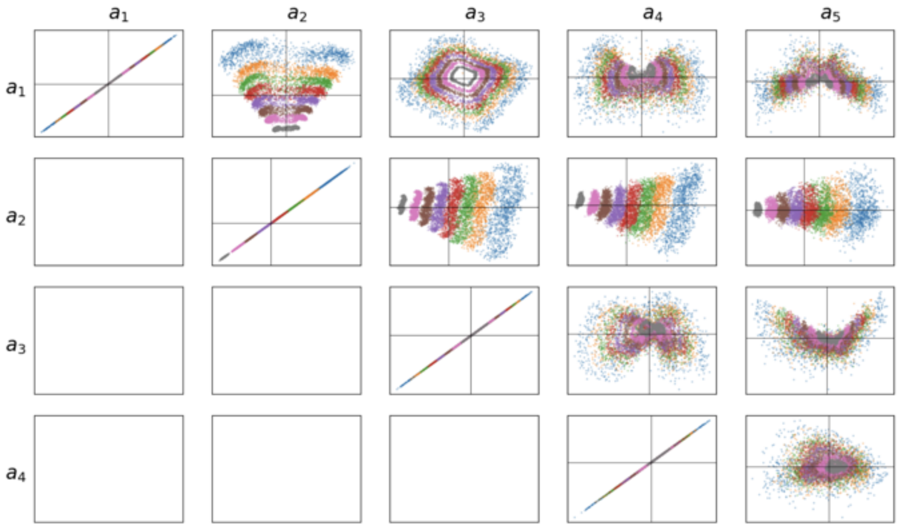

Figure 4.4: Lissajous figure of the dimensionless CPOD mode coefficients. Color indicates different flow rates, blue being the highest flow rate.

4.4 Common base POD analysis of flow rate variation

A Common Base POD [39] is a POD computed from several datasets that vary in a parameter. Experiments were conducted for several flow rates and combined to compute the CPOD. The result is a single set of modes, and a set of mode coefficients corresponding to each parameter realization. The results show that the variation in the flow field is minor when the Reynolds number is changed, because the same set of modes can represent the entire dataset. The dynamic behavior remains unchanged, as Figure 4.4 shows. The Lissajous figure created by the most important modes are self-similar in shape with respect to the Reynolds number variation. A visible difference certainly is the higher spread of the figure at higher flow rates, which may indicate higher variation in the cycle with higher fluctuations uncorrelated to the switching phenomena such as inlet turbulence.

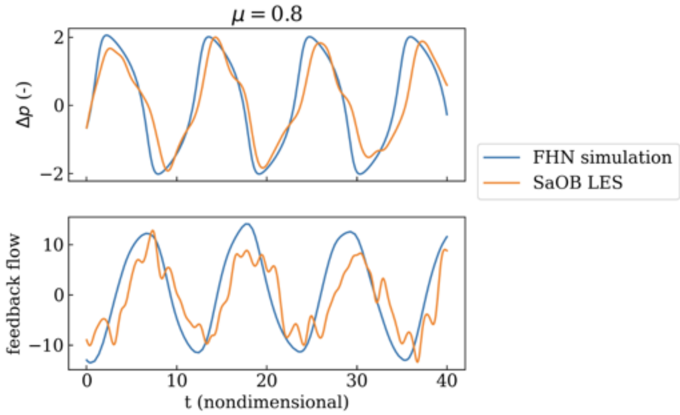

Figure 4.5: Comparison of the FHN system state variables (dimensionless), extracted from CFD simulation and obtained from fitting the equation parameters to the frequency of oscillation in air, demonstration qualitative agreement. μ indicates the damping factor used in the FHN model.

4.5 Application of the FHN equation to the LES data

Another question is if the newly found model is applicable for the air-operated oscillator as well. To obtain a preliminary understanding of this aspect, the CFD data used in publication 1 was used to extract spatially averaged equivalents to the experimental data from publication 2. A simulation was performed and tuned to oscillate at the frequency of the extracted CFD data. Figure 4.5 compares the obtained extracted and normalized data to the simulated, dimensionless data. The general applicability of the FHN system to air-based oscillators is demonstrated by the ability of the simulation to match the CFD extracted data characteristics.

5 Outlook

The field of Active Flow Control has seen extensive research and development, particularly within the aerospace sector. Despite numerous studies demonstrating the potential of AFC to enhance aerodynamic performance by delaying flow separation, reducing drag, and improving lift, there has been limited commercialization of this technology in practical aerospace applications. Several factors contribute to this, creating high entry barriers that have hindered widespread adoption.

Firstly, the stringent security and safety requirements in the aerospace industry present a significant challenge. Any new technology must undergo rigorous testing and certification processes to ensure it does not compromise the safety of the aircraft and its passengers. This adds considerable time and cost to the development of AFC systems for aerospace applications. Additionally, the introduction of AFC devices often entails an increase in the weight of the aircraft due to the need for additional components and actuators, which can negate some of the performance benefits by increasing fuel consumption.

Moreover, the high development costs associated with AFC technology have been a deterrent. The design, testing, and optimization of AFC systems require substantial financial investment, which can be a risk for aerospace companies unless the benefits are clearly demonstrated. Unfortunately, despite the potential advantages, the efficacy and efficiency of AFC in practical scenarios have not been compelling enough to justify the costs. The improvements in performance, while significant in controlled experimental settings, have often been too marginal when scaled up to full-sized aircraft operating under real-world conditions.

However, the application of AFC in the maritime sector presents a promising opportunity for translating this technology into industry. Ships operate in a different environment where the barriers to entry are lower, and the performance benefits can be more pronounced. For instance, the security issues that are paramount in aerospace are less critical in maritime applications, allowing for more flexibility in the design and implementation of AFC systems. Additionally, the weight penalties that are so detrimental to aircraft performance are less significant for ships, which can accommodate the extra weight of AFC devices without severely impacting overall efficiency.

Furthermore, the potential performance improvements offered by AFC for ship rudders and other control surfaces are substantial. By delaying flow separation and reducing drag, AFC can enhance maneuverability and fuel efficiency, leading to significant operational cost savings and reduced environmental impact.

In conclusion, while AFC has struggled to achieve commercial success in the aerospace sector due to high entry barriers and insufficient demonstrated benefits, its application in the maritime industry holds considerable promise. The lower barriers to entry, combined with the potential for significant performance improvements, make the maritime sector an ideal candidate for the successful commercialization of AFC technology. Future research and development efforts should focus on leveraging these advantages to bring AFC from the lab to the docks, providing a clear pathway for its industrial adoption and broader impact.

One of the primary future directions involves further optimization of fluidic oscillators for maritime applications. While the current research has shown that these devices can delay flow separation and improve rudder performance, there is still significant potential for enhancing their design and functionality. Future studies could focus on refining the geometric parameters of the oscillators, exploring different materials and manufacturing techniques to improve durability and performance under marine conditions. Additionally, integrating advanced sensing and control systems could enable real-time adaptation of the oscillation parameters to varying flow conditions, further enhancing the effectiveness of AFC systems.

Another important area for future research is the comprehensive evaluation of the long-term effects of AFC on ship performance and maintenance. While the immediate benefits of reduced drag and improved maneuverability are clear, it is essential to understand the potential impacts on rudder wear and tear, maintenance requirements, and overall vessel longevity. Long-term field studies and simulations could provide valuable insights into these aspects, helping to ensure that the implementation of AFC systems leads to sustainable benefits.

Furthermore, expanding the application of AFC beyond rudders to other ship components offers exciting possibilities. For instance, AFC could be applied to propellers, hulls, and stabilizing fins, potentially leading to even greater improvements in overall vessel efficiency. Investigating the interactions between AFC systems on different components and their combined effects on ship performance could yield a comprehensive approach to flow control in maritime engineering.

Additionally, leveraging advancements of CFD and machine learning could significantly enhance the design and optimization of AFC systems. High-fidelity CFD simulations, coupled with machine learning algorithms, could be used to predict and optimize the performance of AFC devices under a wide range of operating conditions. This data-driven approach could accelerate the development of more effective and efficient AFC solutions.

Finally, the environmental benefits of AFC technology should not be overlooked. By reducing fuel consumption and greenhouse gas emissions, AFC has the potential to contribute significantly to the sustainability goals of the maritime industry. Future research could focus on quantifying these environmental benefits and exploring ways to maximize them, aligning AFC technology development with global efforts to combat climate change.

A deeper and more focused experimental investigation into the spiking, starting, and chaotic behaviors of fluidic oscillators would provide substantial value. Such dedicated studies could further strengthen the theoretical framework established in this thesis and offer insights into the complex dynamics of these intriguing devices. By closely examining the conditions under which spiking and chaotic oscillations occur, researchers can identify the precise parameters that lead to these behaviors, allowing for the development of more robust and predictable fluidic oscillators.

In conclusion, the research presented in this thesis has laid a foundation for the application of AFC in maritime environments. By continuing to explore and refine this technology, there is substantial potential to achieve significant advancements in ship performance, efficiency, and sustainability. The future of AFC in the maritime industry is promising, with numerous opportunities for innovation and impact.

Bibliography

[1] L. Prandtl. Über Flüssigkeitsbewegung bei sehr kleiner Reibung. *Third International Mathematical Congress*, 1904.

[2] Marlyn Y Andino, John C Lin, Seele Roman, Emilio C Graff, Mory Gharib, Edward A Whalen, and Israel J Wygnanski. Active flow control on vertical tail models. *AIAA journal*, 57(8):3322–3338, 2019.

[3] Edward A Whalen, Marc Spoor, Paul M Vijgen, John Tran, Arvin Shmilovich, John C Lin, and Marlyn Andino. Full-scale flight demonstration of an active flow control enhanced vertical tail. In *8th AIAA Flow Control Conference*, page 3927, 2016.

[4] C. E. Spyropoulos. Sonic oscillator. In *Procc. of the fluid amplification symposium*, pages 27–52, 1964.

[5] H. Viets. Flip-flop jet nozzle. *AIAA journal*, 13(10):1375–1379, 1975. URL https://doi.org/10.2514/3.60550.

[6] Xin Wen, Ziyan Li, Luanliang Zhou, Chengji Yu, Zubair Muhammad, Yudan Liu, Shiqi Wang, and Yingzheng Liu. Flow dynamics of a fluidic oscillator with internal geometry variations. *Physics of Fluids*, 32(7), 2020.

[7] Rene Woszidlo, Timo Stumper, C Nayeri, and Christian O Paschereit. Experimental study on bluff body drag reduction with fluidic oscillators. In *52nd Aerospace Sciences Meeting*, page 0403, 2014. URL https://doi.org/10.2514/6.2014-0403.

[8] Moritz Sieber, Florian Ostermann, Rene Woszidlo, Kilian Oberleithner, and C Oliver Paschereit. Lagrangian coherent structures in the flow field of a fluidic oscillator. *Physical review fluids*, 1(5):050509, 2016. URL https://doi.org/10.1103/APS.DFD.2015.GFM.V0015.

[9] Florian Ostermann, Rene Woszidlo, C. Navid Nayeri, and C. Oliver Paschereit. Properties of a sweeping jet emitted from a fluidic oscillator. *Journal of Fluid Mechanics*, 857:216–238, 2018. doi: 10.1017/jfm.2018.739.

[10] Alexander Spens, Patrick J Brandt, and Jeffrey P Bons. Characterization of out-of-plane curved fluidic oscillators. *AIAA Journal*, 62(4):1563–1573, 2024.

[11] Katarzyna Zelazny. Approximate method of calculating forces on rudder during ship sailing on a shipping route. *TransNav, the International Journal on Marine Navigation and Safety of Sea Transportation*, 8(3):459–464, 2014. ISSN 2083-6473. doi: 10.12716/1001.08.03.18.

[12] Jung-Keun Oh, Hae-Seong Ahn, Hyo-Chul Kim, Seung-Hee Lee, and Jae-Moon Lew. Application of coanda effects to a ship hydrofoil. *Journal of Ship and Ocean Technology*, 7(2):29–39, 2003.

[13] Bong-Joon Choi and Hyo-Chul Kim. An experimental evaluation of the coanda jet applied high efficient rudder system for vlcc. *Journal of Ship and Ocean Technology*, 8(2):1–12, 2004.

[14] Hae-Seong Ahn, Hyo-Chul Kim, Je-Jun Park, and Seung-Hee Lee. An application of coanda effect to a flapped rudder. *Journal of Ship and Ocean Technology*, 3(4):23–34, 1999.

[15] Hae-Seong Ahn, Jaehoon Yoo, and Hyochul Kim. An advanced study on the development of marine lifting devices enhanced by the blowing techniques. *Journal of Ship and Ocean Technology*, 8(4):1–9, 2004.

[16] Oxoc Gim. On Flow Charactistics around Special Rudders by PIV Measurement; Flapped and Water-blowing Rudder. *Journal of the Korean Society of Marine Environment & Safety*, 23(2):200–207, 2017.

[17] Dae-Won Seo, Jungkeun Oh, and Jinho Jang. Performance analysis of a horn-type rudder implementing the coanda effect. *International Journal of Naval Architecture and Ocean Engineering*, 9(2):177–184, 2017.

[18] H-J Schmidt, R Woszidlo, CN Nayeri, and CO Paschereit. Separation control with fluidic oscillators in water. *Experiments in Fluids*, 58(8):1–17, 2017.

[19] Rene Woszidlo, Florian Ostermann, and Hanns-Joachim Schmidt. Fundamental properties of fluidic oscillators for flow control applications. *AIAA Journal*, 57(3):978–992, 2019.

[20] Bernhard C Bobusch, René Woszidlo, JM Bergada, CN Nayeri, and CO Paschereit. Experimental study of the internal flow structures inside a fluidic oscillator. *Experiments in fluids*, 54(6):1559, 2013.

[21] JR McDonough, R Law, J Kraemer, and AP Harvey. Effect of geometrical parameters on flow-switching frequencies in 3d printed fluidic oscillators containing different liquids. *Chemical Engineering Research and Design*, 117:228–239, 2017.

[22] I. Wygnanski. Boundary layer and flow control by periodic addition of momentum. *AIAA journal*, 2117, 1997.

[23] Dov Oster and Israel Wygnanski. The forced mixing layer between parallel streams. *Journal of Fluid Mechanics*, 123:91–130, 1982.

[24] Avi Seifert and LaTunia G. Pack. Active flow separation control on wall-mounted hump at high reynolds numbers. *AIAA Journal*, 40(7):1363–1372, 2002. doi: 10.2514/2.1796. URL https://doi.org/10.2514/2.1796.

[25] Avi Seifert, David Greenblatt, and Israel J Wygnanski. Active separation control: an overview of reynolds and mach numbers effects. *Aerospace Science and Technology*, 8(7):569–582, 2004.

[26] Mehti Koklu and Lewis R Owens. Comparison of sweeping jet actuators with different flow-control techniques for flow-separation control. *AIAA Journal*, 2017.

[27] David Greenblatt and Israel J Wygnanski. The control of flow separation by periodic excitation. *Progress in Aerospace Sciences*, 36(7):487–545, 2000.

[28] Bar Mizrahi and Avraham Seifert. The oscillatory suction actuator: Fundamentals, interactions and efficiency. In *AIAA AVIATION 2020 FORUM*. AIAA, 2020. doi: 10.2514/6.2020-2941. URL https://arc.aiaa.org/doi/abs/10.2514/6.2020-2941.

[29] Roman Seele, Emilio Graff, Morteza Gharib, Lutz Taubert, John Lin, and Israel Wygnanski. Improving rudder effectiveness with sweeping jet actuators. In *6th AIAA Flow Control Conference*, page 3244, 2012. URL https://doi.org/10.2514/6.2012-3244.

[30] A. Seifert and LG. Pack. Oscillatory control of separation at high reynolds numbers. *AIAA Journal*, 37(9):1062–1071, 1999.

[31] A. Seifert, T. Bachar, D. Koss, M. Shepshelovich, and I. Wygnanski. Oscillatory blowing: a tool to delay boundary-layer separation. *AIAA journal*, 31(11):2052–2060, 1993.

[32] Raymond W Warren. Fluid oscillator, January 9 1962. US Patent 3,016,066.

[33] G. Arwatz, I. Fono, and A. Seifert. Suction and oscillatory blowing actuator. In *IUTAM Symposium on Flow Control and MEMS*, pages 33–44. Springer, 2008. doi: 10.2514/1.30468.

[34] F. Ostermann, R. Woszidlo, C. Nayeri, and C.O. Paschereit. Experimental comparison between the flow field of two common fluidic oscillator designs. In *53rd ASM*, page 0781, 2015.

[35] T. Shtendel and A. Seifert. Three-dimensional aspects of cylinder drag reduction by suction and oscillatory blowing. *Int J Heat Fluid Flow*, 45:109–127, 2014. URL https://doi.org/10.1016/j.ijheatfluidflow.2013.10.009.

[36] A. Seifert, O. Stalnov, D. Sperber, G. Arwatz, V. Palei, S. David, I. Dayan, and I. Fono. Large trucks drag reduction using active flow control. In *The Aerodynamics of Heavy Vehicles II: Trucks, Buses, and Trains*, pages 115–133. Springer, 2009.

[37] Marlyn Y Andino, John C Lin, Anthony E Washburn, Edward A Whalen, Emilio C Graff, and Israel J Wygnanski. Flow separation control on a full-scale vertical tail model using sweeping jet actuators. In *53rd AIAA Aerospace Sciences Meeting*, page 0785, 2015. doi: 10.2514/6.2015-0785.

[38] John C Lin, Marlyn Y Andino, Michael G Alexander, Edward A Whalen, Marc A Spoor, John T Tran, and Israel J Wygnanski. An overview of active flow control enhanced vertical tail technology development. In *54th AIAA Aerospace Sciences Meeting*, page 0056, 2016. URL https://doi.org/10.2514/6.2016-0056.

[39] J. Kriegseis, T. Dehler, M. Gnirß, and C. Tropea. Common-base proper orthogonal decomposition as a means of quantitative data comparison. *Meas. Sci. Technol.*, 21(8):085403, 2010.